CENTRALE
LYON

Entanglement generation and measurement in electron quantum optics

Final year thesis

Student :
Mathieu Paulet

Professors :
Pascal Degiovanni
Ségolène Callard

July 9, 2025

TRAVAIL DE FIN D'ETUDES

Année Scolaire 2024-2025

Ce formulaire est à insérer après la page de garde de votre rapport. Il atteste que le rapport a été validé par l'entreprise et peut être communiqué en l'état au Service de la Scolarité de l'Ecole Centrale de Lyon.

VALIDATION DU RAPPORT DE TFE
PAR L'ENTREPRISE

Références du Travail de Fin d'Etudes

Nom de l'élève :

Titre du rapport :

Entreprise :

Nom du Tuteur entreprise :

Nom du Tuteur ECL :

L'entreprise reconnaît avoir pris connaissance du rapport mentionné ci-dessus et autorise sa transmission à l'Ecole Centrale de Lyon.

L'entreprise autorise la diffusion du rapport sur le catalogue de la bibliothèque de l'Ecole Centrale de Lyon :

- les informations sur le TFE (titre – auteur – mots-clés – résumé…) seront publiques.
- L'accès au rapport pdf, sur authentification, sera limité aux étudiants et personnels de l'Ecole Centrale de Lyon.

Le représentant de l'entreprise

Nom :

Fonction :

Date :

Signature et cachet

Abstract

This work is a theoretical study focusing on several aspects of the determination and manipulation of a single electron's quantum state. We first introduce the concept of electronic flying qubit, as well as its use within a paradigm of non-stationary-qubits quantum computer. A potential experimental realization of such qubits is also described, based on Levitons propagating ballistically along quantum Hall edge channels. Their physical implementation is then illustrated by a system composed of two parallel propagation channels allowing electrons to carry quantum information: the railroad qubit

Next, we introduce the notion of first-order electronic coherence function, both in the physical and the time-frequency spaces. This mathematical tool is fundamental for studying the single electron's physics in mesoscopic quantum conductors. The principle of an existing electronic quantum tomography protocol, based on Hong-Ou-Mandel interferometry, is then presented, followed by a discussion of its practical and experimental limitations. A novel theoretical improvement of this protocol, relying on voltage pulse trains, is then proposed and illustrated with a simple example. This protocol allows for a more precise exploration of the frequency domain and is theoretically more efficient than the previous one.

Finally, we present the second-order electronic coherence function in order to study three entanglement witnesses resulting from the Cauchy-Schwarz inequality. We derive their expressions in the context of electronic quantum optics in terms of the first- and second-order coherence functions. We also provide a representation of these criteria in terms of spin operators to better grasp their physical significance. We illustrate this general discussion by a detailed study of a coherent two-electron scattering model. The collision-induced entanglement creation is assessed *via* the Cauchy-Schwarz entanglement witnesses expressed in the energy domain.

Résumé

Ce travail est une étude théorique portant sur plusieurs aspects de la détermination et de la manipulation de l'état quantique d'un électron. Nous y présentons d'abord le concept de qubit volant électronique, ainsi que son utilisation dans un paradigme d'ordinateur quantique à qubits non-stationnaires. Une piste de réalisation expérimentale d'excitations électroniques adaptées à ce contexte, basée sur des Levitons se propageant ballistiquement dans des canaux de bord résultant de l'effet Hall quantique, est également décrite. L'implémentation physique de ces qubits est alors illustrée par un système de deux canaux de propagations parallèles permettant aux électrons de transmettre de l'information quantique: le *railroad qubit*.

Ensuite, nous introduisons la notion de fonction de cohérence électronique du premier ordre dans l'espace physique, ainsi que dans l'espace des temps-fréquences. Cet outil mathématique est fondamental pour étudier la physique des électrons individuels dans des conducteurs quantiques mésoscopiques. Le principe d'un protocole de tomographie quantique électronique existant, basé sur l'interférométrie Hong-Ou-Mandel, est alors présenté, puis ses limites pratiques et expérimentales sont exposées. Alors, une amélioration théorique nouvelle de ce protocole, reposant sur des trains d'impulsions de voltage, est proposée puis illustrée sur un exemple simple. Ce protocole permet une exploration plus précise de l'espace des fréquences, et est théoriquement plus efficace que le précédent.

Enfin, nous présentons la fonction de cohérence électronique du second-ordre, afin d'étudier trois critères d'intrication découlant de l'inégalité de Cauchy-Schwarz. Nous dérivons leurs expressions dans le contexte de l'optique quantique électronique en fonction des fonctions de cohérence du premier et du second ordre. Nous présentons également une représentation de ces critères en termes d'opérateurs de spin afin de mieux appréhender leur signification physique. Nous terminons par une étude détaillée d'un modèle de diffusion cohérente à deux électrons. La création d'intrication causée par la collision est ensuite discutée grâce au critère d'intrication de Cauchy-Schwarz exprimée dans le domaine des énergies.

Acknowledgments

I would like to express my sincere gratitude to all those who supported and guided me throughout the course of this six-month internship, as well as during the preparation of this scientific report. This experience has been simultaneously intellectually fulfilling, professionally enriching, and personally rewarding. It would not have been possible without the help and involvement of many individuals.

First and foremost, I would like to extend my deepest thanks to my internship supervisor, Pascal Degiovanni. His expert guidance, scientific rigor, and constant encouragement played a vital role throughout the duration of this project. I am especially grateful for his (amazing) availability, his enthusiasm, his detailed and constructive feedback, and for fostering an environment where I was encouraged to ask questions, take initiatives, explore ideas, and develop my autonomy as a young researcher.

Of course, I also truly thank Giacomo Rebora who, as the team's post-doctoral student, assisted Pascal in coordinating my internship and answering all my questions. His regular sanity checks in my office all along the internship prevented me from drowning in bibliography or calculations. Also, including me in his research by letting me repeat his calculations, both as a training and a result-checking, made me really feel as a part of the team.

I also thank Pascal's most regular collaborators, Alexandre Feller and Benjamin Roussel, for all the weekly working-group meetings they had with our team. These sessions were a great opportunity for me to appreciate the importance for a researcher to stay updated about his colleagues' research, and the necessity to remain curious about scientific topics that are seemingly unrelated to its own. Through these discussions, Alex and Benjamin introduced me to fields of mathematics and physics that I did not even suspect the existence before, and I thank them for the time they took to explain it to me.

My thanks also go to Rémy, who joined the team even more recently than me, as a master's first-year intern. His questions as a new member in the team helped me to take a step back on the research I do, and realize the parts of my work that I did not really understand. Most importantly, together we showed that engineering students could indeed do fundamental research.

Then, I obviously thank the few people I was the closest to - literally - during these six months: those I shared the office with. I thank Andrea, Ashesh, Kinan, and Nick for the friendly atmosphere in the office, and the discussions about each other's research field. I hope that this small M7-111 community will initiate great discoveries, whether it be in machine learning, hydrodynamics, or quantum physics.

I want to thank the PhD students I met during my internship, for including me in their traditional *11h45* daily routine from my first day in the lab. Thank you Alex, Antonin, Geoffroy, and Marlysa for our passionate conversations about theoretical physics (sorry Marlysa), video games (about which I learnt a lot), and other fundamental society subjects such as the best kind of chocolate (which is of course dark chocolate) or the correct human / bear ratio for a balanced fight (assuming an optimized human strategy).

I also wish to thank all the members of the Laboratoire de Physique de l'ENS de Lyon I did not thank yet for their warm welcome and for the collaborative atmosphere that made daily work both productive and enjoyable. I am particularly indebted to Pierre Borgnat and Adrien Meynard, from the Signal Processing research team, with whom I collaborated at the beginning of this project. Their patience and generosity in sharing their knowledge helped me overcome many challenges at a time when I was still discovering my own research domain. Their technical expertise, insightful discussions, and friendly support contributed to the progress and quality of this work.

I would also like to thank my academic advisor at Ecole Centrale de Lyon, Ségonlène Callard, for her continued support throughout this internship period. Her follow-up was essential in connecting this research experience with the academic requirements of my engineering school's program.

Finally, I would like to acknowledge the broader scientific community whose published works and shared tools have supported the development of this project. The open exchange of ideas is what makes scientific progress possible, and I am thankful to have taken part in this process.

Contents

1 Introduction

Electron quantum optics (EQO) is a recent field [17] originally initiated by the demonstration of an on-demand single-electron source in 2007 [13]. For the last fifteen years, numerous milestones have been achieved. Basic experiments of photonic quantum optics have been demonstrated with electrons, such as the Hanbury Brown-Twiss [7] and the Hong-Ou-Mandel (HOM) [6] experiments. In the meantime, electronic single-particle and two-particle interferometry - like Hong-Ou-Mandel [22] or Mach-Zender [23] interferometers - have been used in order to study the decoherence of electronic excitations during their propagation. Finally, experiments consisting in the determination of electronic quantum states have been performed *via* quantum tomography protocols [5]. This access to the quantum properties of electrons within quantum coherent conductors has opened a lot of previously unreachable perspectives. Among them, one of the most relevant and promising is the question of electron entanglement and its potential use in quantum technologies.

One idea is to encode quantum information into electronic states to mimic universal quantum computing using photons. Indeed, working with fermions presents several advantages over bosons. For example, the velocity of electrons in a quantum conductor being much inferior to the speed of light, this allows the conception of a delocalized quantum computer, in which operations are performed with fixed hardware on propagating qubits [10]. Such qubits are called *electronic flying qubits* and have been investigated for a few years now. They present another advantage compared to photons, as they easily interact with each other. This paves the path to the studying electronic entanglement, and using it to process quantum information.

For such a model to work correctly, it is of capital importance to be able to efficiently determinate the precise quantum state of an electron. For now, the electron quantum tomography protocols are based on two-particle interferometry, and the theory behind them involves the use of first-order electronic coherence function [26]. Actually, these protocols probe the unknown electron's representation in the time-frequency space, giving access to what is called the *Wigner representation* of its coherence function. Then, a second step consists in the translation of this representation into a wave-function in the physical space-time. Experimentally, the method presently used gives a proof that the quantum state of an electron can indeed be determined, but has a pretty restricted practical range of application. As a matter of fact, the HOM protocol performed in [5] allows a good reconstruction of simple-enough quantum states, but requires a large number of high precision current noise measurements, taking an unworkable amount of time (~ 5 minutes/point).

Then, contrary to the photonic case, the notion of entanglement between electrons has not been experimentally studied by the community yet. Being a two-particle phenomenon, electronic entanglement requires the use of the second-order electronic coherence function [26]. To this day, the current understanding of electronic entanglement mostly relies on theoretical works. Indeed, the theory for fermions is slightly different from the bosonic case, and requires to take some precautions when comparing electrons and photons. For example, a fermionic quantum theory of information is currently being developed [28], while other adaptations of the quantum theory of information are made for the case of indistinguishable particles [3]. It is commonly understood, since Bell's contribution in 1964 [2], that entanglement relies on tensions between mathematical inequalities - called *entanglement criteria* - and physical states: an entangled state is a state violating such inequalities. A lot of such criteria are known as of today [29], but their use in the context of EQO still needs to be studied.

This is precisely the objective of this document. During the two first months of this internship, I have focused on the reconstruction of an electronic quantum state. The work consisted in proposing an ameliorated tomography protocol that could allow an experimentalist to access the exact quantum state of an electron more efficiently, that is to say with a shorter measurement time. This protocol exploits the fact that the charge carried by a single-electron excitation remains very small. Indeed, while the present HOM protocol proposes to reconstruct the quantum state harmonic by harmonic, the newly developed *voltage pulse-train* protocol allows the use of linear combinations of sinusoidal signals, and thus to reproduce the shape of wavelets with interesting properties to determinate the unknown signal. This gives the possibility to selectively explore specific areas of the Wigner space by tuning parameters of the probing signals. Consequently, the reconstruction of the quantum state can be done in a quicker and more efficient way.

Moreover, this "coherent" HOM protocol is also more polyvalent than the generic HOM protocol, as it is more efficient than its predecessor with the reconstruction of high-energy electronic wave-functions.

The rest of the internship was dedicated to the study of quantum entanglement witnesses for electronic quantum states. For that matter, we considered three criteria derived from the mathematical Cauchy-Schwarz inequality [29]. The last two of them were a particular case of the first one, particularly useful for the study of one-electron states. Starting from their general mathematical form, we derived their expression in terms of first- and second-order electronic coherence functions, thus adapting them so they can be used in EQO. Also, we worked on building a representation of these criteria in terms of wisely-defined "spin-operators", in order to make their implications easier to apprehend. This formalism gives a way to easily visualize the states that respect or violate the two one-electron criteria, hence giving a way to classify their strength. Finally, we applied the first - and most general - criterion to probe the entanglement generated by a two-particle coherent scattering model, and looked at its consequences on the resulting two-electron state.

This document is divided into three parts. In the first section, we will mainly contextualize our work and introduce the basic concepts and experimental tools that constitute the framework of our studies. More precisely, we will define the notion of *electronic flying qubit*, and insist on the motivations that lead to its study and development during the last few years. We will also give a short description as well as some key features of EQubitFly, the national research program funding the work done during this internship. Then, the implementation of electronic flying qubits with Levitons will be detailed. We will first explain what is a Leviton, before presenting the arguments justifying its use in the making of qubits. Finally, we will have a first look at the notion of electronic entanglement and how to physically generate it in a lab by introducing the concept of *railroad qubit*.

The second section will focus on the first-order electronic coherence, and its use to develop electron quantum tomography protocols. We will start by introducing the first-order electronic coherence function and its Wigner representation in the time-frequency space. We then dispense the generic HOM quantum tomography protocol. After describing the experimental setup used for this protocol, we discuss its drawbacks and limitations. This will justify the development and study of the pulse-train protocol idea, which will then be presented and discussed.

Last but not least, the third section will be devoted to the second-order coherence and the study of three Cauchy-Schwarz entanglement witnesses. After explaining the theory of second-order electronic coherence function, we will recall some important results of a quantum theory of information for indistinguishable fermions. Then, we will present the various entanglement witnesses and their expression in EQO. The spin-operator representation will then be used to visualize their physical meaning. Finally, we will study the possibility to create entanglement between two electrons by making them collide. Studying a two-electron coherent scattering model with two energy-localized electronic wave-packets, we will compare the conclusions given by an entanglement criterion and the general Cauchy-Schwarz inequality.

2 Electronic flying qubits

Over the last few decades, a huge amount of research has been conducted - whether it be in computer science or in physics - in order to develop an operational quantum computer. Due to the promising results obtained so far, as well as the important demand from the industry or the numerous potential applications of such a device, this field of research is nowadays more relevant than ever before. In the physics community, the most studied aspect of the problem is without any doubt the realization of physical qubits.

The *qubit* is the key-concept of quantum computation [8], as it represents the quantum equivalent of the classical elementary unit of information, called *bit*. While a classical bit can take only two values (0 or 1), a qubit $|\psi\rangle$ can be seen as a normalized quantum superposition of the states $|0\rangle$ and $|1\rangle$, where we used the Dirac formalism and the notation $|\cdot\rangle$ to designate a quantum state. A qubit can then generally be written as $|\psi\rangle = \alpha\,|0\rangle + \beta\,|1\rangle$, where $(\alpha, \beta) \in \mathbb{C}^2$ and the normalization condition imposes $|\alpha|^2 + |\beta|^2 = 1$. As of today, many leads are explored in several branches of physics to find two-level (representing the $|0\rangle$ and $|1\rangle$ states) quantum-mechanical systems whose degree of freedom could be used to carry qubits states. These include photons (using polarization), atoms, trapped ions on artificial systems (such as superconducting circuits) using suitable quantum states as $|0\rangle$ and $|1\rangle$. But these also include electrons, which leads to the concept of electronic flying qubits.

In the whole document, we will focus on the case of electronic flying qubits. The aim of this section is to define and introduce this concept. First, we will start with specifying what an *electronic flying qubit* exactly is, and specify the motivations that lead to consider this specific type of qubit as a promising lead to build a universal quantum computer. Then, in order to give a more specific context to our study, we will present the EQubitFly project, in which this internship takes place. After this, we will give a brief description of the most promising way to produce such qubits *on demand*. It relies on the emission of specific single-electron excitations called *Levitons* in a mesoscopic conductor [9]. To conclude this section, we will introduce the notion of electronic entanglement, and insist on its necessity to realize operations on electronic flying qubits.

2.1 What is an electronic flying qubit?

The definition of a qubit given in this section's introduction paragraph is very conceptual and general. However, numerous types of qubits exist in practice. As we just saw, qubits differ by their physical implementation, which also defines the type of quantum computer considered. As a matter of fact, the most widespread paradigm regarding the concept of a quantum computer currently relies on *localized* (or *stationary*) two-levels systems on which quantum operations are performed by the means of fixed hardware. Nevertheless, this vision of the quantum computer has a non-negligible drawback: scalability. Indeed, due to their stationarity, each qubit requires an amount of hardware specifically dedicated to it. In order to make a multi-qubit quantum computer, it is then necessary to multiply not only the number of physical qubits, but also the number of gates to act on them. This scalability issue is a considerable obstacle to the development of such a kind of quantum computer.

An alternative to this paradigm is to use *propagating* (or *flying*) qubits that could propagate through a single set of quantum gates. Under the assumption that they could be generated on demand, such qubits would solve the problem of scalability, as they would all share the same hardware (see figure 1). For now, the only kind of existing flying qubits uses propagating photons. Still, a problem remains with photons as their propagation speed c is so important that their trajectories must be set in advance. This prevents any in-flight reconfiguration, and the operations to perform then need to be determined prior to their emission. Another limitation encountered with photons is that they don't interact with each other. Even though interaction with the environment is most of the time undesirable for a qubit - as it affects its quantum state and spoil quantum algorithms -, the qubit must however still be sensitive to some interactions in order for the experimentalist to prepare its initial state, or to use multi-qubits gates.

To overcome these issues, it seems reasonable to think about fermions like electrons [20] to make flying qubits. Indeed, an on-demand single electron source - based on quantum-dots - already exists [13], and the typical speed v_F at which the electronic excitations propagate in a mesoscopic conductor is considerably

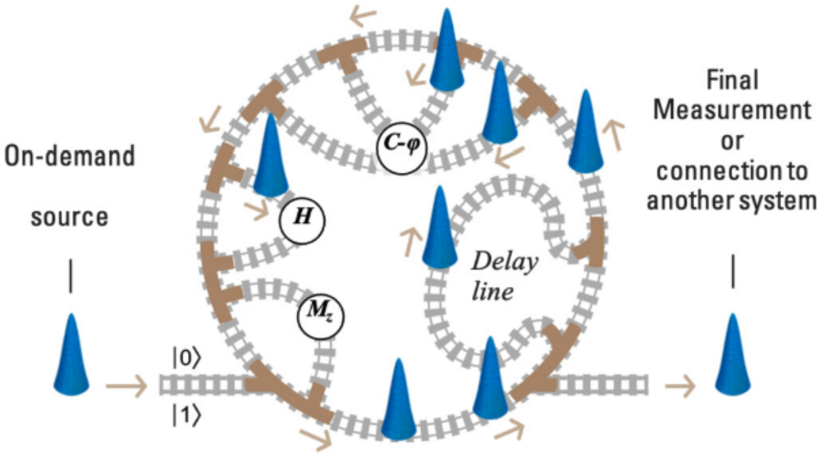

Figure 1: Schematic representation of the flying qubit paradigm for quantum computers (adapted from [10]). The flying qubit on-demand source (on the left) sends a qubit in the pre-set hardware track - composed of a universal quantum gates set - common to all qubits. Depending on the operations to perform on the qubit, the experimentalist chooses the itinerary of the qubit - meaning the gates it will go through - similarly to the railway stations visited on a train line. Once the track is completely covered, the qubit exits the quantum computer and is ready to be measured or connected to another system (on the right).

lower than the speed of light c ($v_F \sim 10^{-2}c$). Besides, their electric charge causes them to interact directly with each other *via* the Coulomb interaction, and hence enables the creation of entanglement and the use of a two-qubits gate. However, an important difficulty when trying to implement a physical qubit, especially with electrons, is the preservation of its coherence - and consequently of the quantum information it carries - along its propagation.

In order to be a good flying qubit, its quantum state must ideally remain exactly the same between its creation and its measurement. As mentioned earlier, quantum objects interact with their environment. Electrons propagating in a conductor suffer from the presence of the electrons forming the Fermi sea, with which they necessarily interact. Therefore, the Coulomb interaction needed to tune the qubit state also tends to alter its initial properties. The carried information is thus destroyed by the environment after a short propagation time. Typically, the coherence time of an electron in a conductor varies between the dozen of picoseconds to the nanosecond. Hence, it is of crucial importance to control the quantum state of an electronic flying qubit on sub-nanosecond time-scales. The demonstration of such a functional electronic flying qubit would then probably be the instigator of a paradigm shift regarding quantum computers. This is precisely the reason why the EQubitFly project has been initiated.

2.2 The EQubitFly project

The internship constituting the object of this report is funded by a large research project on electronic flying qubits called EQubitFly. This project is a part of a French national research initiative on quantum technologies. It is dedicated to the development of a quantum nano-electronics platform aimed at realizing, controlling, and detecting electronic flying qubits. Spanning from February 2023 to February 2029, the project is coordinated by Dr. Christopher Baüerle at CNRS Néel Institute in Grenoble. As a part of the France 2030 scientific program on quantum technologies, it is supported by a 4.5 M€ grant from the French National Research Agency (ANR).

The primary objective of EQubitFly is to demonstrate the feasibility of high-speed, coherent manipulation of such flying qubits on picosecond timescales, targeting operational frequencies in the terahertz regime. To support these efforts, the project combines advanced theoretical frameworks - including quantum field theory in mesoscopic systems, numerical simulations, and data-driven techniques like machine learning - with state-of-the-art experimental platforms. The project focuses on two central technological challenges.

The first one is the on-demand generation of single electrons with picosecond time resolution, using quantum capacitors and engineered voltage pulses to emit well-defined electronic wave packets. Indeed, the quantum-dot-based single electron source developed by G. Fève in 2006 is able to produce relatively high-energy electrons ($E \sim 1meV$), whose relaxation during propagation is not compatible with the realization of electronic flying qubits. However, one key experimental achievement has been the demonstration of coherent emission and manipulation of specific excitations called *Levitons* in graphene-based quantum Hall edge channels, a major step toward realizing solid-state analogs of quantum optics with electrons. Indeed, these quasi-particles produced by the application of a Lorentzian voltage pulse to a single-electron source have several advantages, like having a long coherence time.

The other task focuses on *single-shot* detection of these electrons with high temporal precision, enabling real-time readout of quantum information and coherence properties during flight. For now, the best electron detectors are not fast enough to permit such performances: they need integration times comparable to a microsecond, whereas the temporal width of a single electronic excitation is of the order of a picosecond. Then, the statistical determination of quantum information is achieved *via* average current on current noise measurements. However, a functional quantum computer needs to be able to detect electronic excitations after a single measurement. When repeated, these single-shot measurements could lead to the determination of their quantum properties "on the fly".

EQubitFly is a collaborative effort involving several leading French research institutions: CNRS, Université Grenoble Alpes, CEA, Université de Savoie Mont-Blanc, École Normale Supérieure de Lyon, Université d'Aix-Marseille, Sorbonne Université, and Université Paris Cité. In this project, the École Normale Supérieure de Lyon team is engaged in the theoretical studies related to the quantum tomography method that allows the determination of the quantum information carried by electronic excitations, and to the generation and detection of entanglement between flying qubits. By integrating experimental expertise and theoretical innovation, the project aims to establish foundational technologies for future devices based on electronic flying qubits, contributing to the broader vision of scalable and distributed quantum information processing. For example, some applications in the field of quantum sensing are already being investigated, among others through the QSig4QSense project.

The context of the following study is now settled. As mentioned, the project focuses on a specific type of quasi-particle to play the role of electronic flying qubits in the mesoscopic conductor: the Leviton. The details about the production of these so-called *Levitonic electronic flying qubits* are given in the following subsection.

2.3 The Levitonic electronic flying qubit

Levitons are quasi-particles first theorized by L.S. Levitov in 1997 [21]. They consist of an electronic excitation on top of the Fermi sea built from a single voltage pulse. To understand why it is so special, it is important to stress out the fact that applying a voltage pulse to the Fermi sea usually excites both electrons and holes - thereby populating energy levels respectively above and under the Fermi sea. A practically annoying consequence is that the generation of any purely electronic wave-packet is generally prevented. However, Levitov et al. showed that applying a specific Lorentzian voltage pulse V to the Fermi sea would theoretically create an excitation that does not leave any hole and only generate an electronic excitation just above the Fermi sea:

$$V(t) = \frac{V_0}{\pi} \frac{\tau}{t^2 + \tau^2}. \tag{1}$$

In equation (1), V_0 and τ respectively correspond to the voltage pulse amplitude and half-width at half maximum. Since we require the pulse to carry exactly one electrical charge, V_0 and τ need to satisfy the normalization condition $e \int_{\mathbb{R}} V(t)dt = h$, where e is the elementary charge and h is Planck's constant. Consequently, we will indifferently talk about *electrons* and *electronic excitations* in the following of this document. The reason why these excitations are so important is because, contrary to the "high-energy" excitations we can emit with the quantum-dot-based source, Levitons fill the energy levels located right above the Fermi sea (see figure 2) and are indeed more robust to relaxation. This low energy gives to Levitons very good coherence properties [25], and explains why they are such good candidates to realize fermionic flying-qubits.

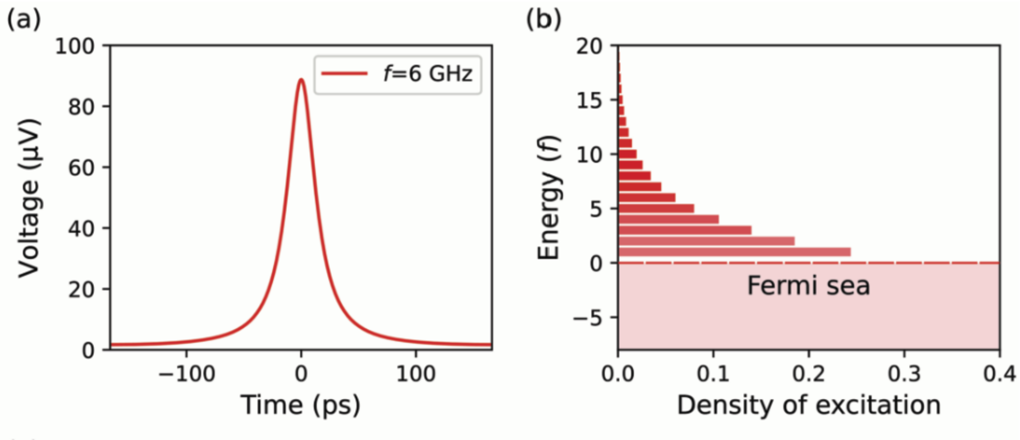

Figure 2: Levitonic excitation (from [10]). (**a**) Temporal representation of a Leviton. The voltage pulse applied to an Ohmic contact in order to produce this type of quasi-particle is a Lorentzian function with a width of a few hundreds of picoseconds. (**b**) Spectral representation of a Leviton. This graph shows that a Levitonic excitation only fills energy levels above the Fermi sea, without perturbing the sea itself. The excitation's wave-function is exponentially decaying with energy.

In order to use these excitations as quantum information bits, it is necessary to build structures allowing to manipulate their quantum state. Detailed information about how to build a quantum optics circuit with electrons are given in the next section. For now, let's simply specify that several ideas are already investigated to produce these qubits on demand [15], detect Levitons on the fly [16], tune their quantum state [23], or implement gates using interferometers based on Coulomb coupling [4]. Knowing this, the importance of the two previously mentioned objectives of the EQubitFly project - efficient generation of sub-nanosecond voltage pulses and single-shot electron detection - is clear, as they are the foundations of what could become an electronic qubit platform.

As mentioned earlier, a great advantage of electronic flying qubits over photonic ones is that fermions easily interact with each others, hence the possibility to conceive multi-qubits gates. Indeed, the Coulomb interaction-based devices currently considered to manipulate the Levitonic qubits, like the CNOT gate, are actually two-qubits gate creating entanglement between two electronic excitations. Then, the last - and maybe the most important - notion to have in mind in order to fully understand this internship's context is electron entanglement

2.4 Electronic entanglement and railroad qubit

The last subsection showed the necessity to understand entanglement between electrons in order to make operations on electronic flying qubits. To see how entanglement can concretely be used in electron quantum optics, let's introduce the notion of *railroad qubit*. This architecture is basically imposed when working with electronic qubits, because of what is called the *super-selection rule* (see section 4.2.1). For this reason, this is also the typical system we will study in the last part of this report.

A railroad qubit is a system composed of two parallel 1D-channels in which electronic excitations can propagate freely, as shown in figure 3. Physically, such channels are most of the times quantum Hall edge channels, resulting from the application of a strong magnetic field to a two-dimensional electron gas (2DEG) at cryogenic temperature. They follow the edges of the 2DEG and are chiral, allowing the

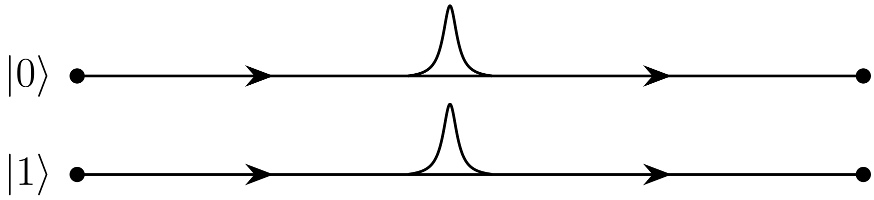

Figure 3: Schematic representation of a railroad qubit. The rails consist of quantum Hall edge channels in AsGa. The upper rail is the *0-rail* and the lower one represents the *1-rail.* The arrow on the channels represent their chirality. In the figure, the probability density of the quantum state $|\psi\rangle = \frac{1}{\sqrt{2}}(|0\rangle - |1\rangle)$ is represented: the common pre-factor accounts for the fact that the electronic excitation is equally delocalized between both rails, and the minus sign indicates a phase opposition between the excitations on both channels (not visible with the density probability).

electrons to propagate ballistically. These two quantum wires are called the *0-rail* and the *1-rail.* The presence of an electronic excitation in the first channel represents the logical state $|0\rangle$ of the qubit, while the same excitation in the other channel represents the state $|1\rangle$.

To manipulate the qubit and change its quantum state, we must now manage to precisely delocalize an electronic excitation on the two-channels. The coherence of such systems is determined by the length L_ϕ over which the phase of the excitations remain coherent in the channels. In AsGa - which is the most common material for EQO circuits - at 10 mK, we typically have $L_\phi \sim 40\ \mu m$ [20]. By bringing together both channels over a length L_C, an electron initially located e.g. in the channel $|0\rangle$ will oscillate back and forth between both channels with a transfer period L_t due to the coupling induced by the short distance between the channels. This way, a gate transferring the excitation from one channel to the other can be designed by choosing $L_C = L_t/2$. Similarly, a gate splitting equally the excitation in both channels can be made by choosing $L_C = L_t/4$: this is the Hadamard gate (H), equivalent to a beam splitter. This is completely coherent with the experimental reality, as it has been shown that, in real systems, $L_t \simeq 56\ \mu m$ [27]. Consequently, $L_t/2 < L_\phi$ and $L_t/4 < L_\phi$, allowing the physical implementation of these gates. Without entering into unnecessary details, we would also need, in order to build a universal set of quantum gates, a single qubit phase-shift (P_ϕ) and a controlled sing-flip (CP_π) gates (see [20]). The CP_π gate is the only one to act on two qubits: if the first one is in the state $|1\rangle$, it changes the sign of the second one by inducing a π phase-shift on it. A part of our work, presented in section 4, was actually done in the idea to determine whether this operation is indeed performed or not microscopically.

Using two railroad qubits, and performing operations on them by the means of the previously mentioned quantum gates, it is then possible to create entangled flying qubits. By *entangled* states, we mean two-qubits states for which each qubit cannot be described independently of the state of the other. Mathematically, this means that the ket $|\psi\rangle$ describing the entangled state cannot be written as the tensor product between the state of the first qubit and the state of the second. As an example, the railroad qubit-based quantum circuit presented in figure 4 shows how to create a (maximally) entangled Bell state starting from two independent qubits. For example, if the two input qubits are in the state $(|0\rangle, |0\rangle)$, it creates the entangled Bell state $|\psi\rangle = \frac{1}{\sqrt{2}}(|00\rangle + |11\rangle)$.

In figure 4, it is the controlled sign-flip gate CP_π who produces the entanglement. By acting on the state of one qubit conditionally to the state of the other, it introduces a "link" between both qubits, preventing the independent description of their individual state.

All the fundamental concepts related to what has been done during this internship have now been introduced. First, we have seen what was an electronic flying qubit, and why these qubits are very promising regarding a new paradigm of universal quantum computer with propagating qubits. Then, we added more context with the presentation of the EQubitFly project, to which this internship is directly

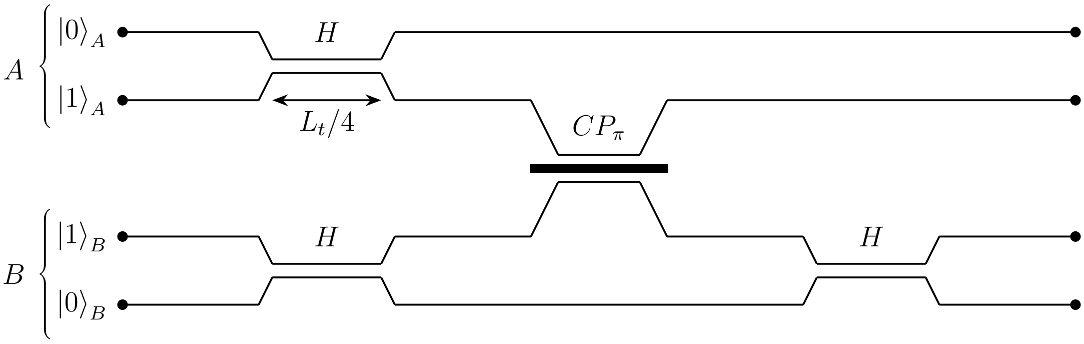

Figure 4: Quantum circuit creating a Bell state from two independent qubits, labelled A and B (adapted from [20]). It is composed of three Hadamard gates (H), and one controlled flip-sign gate (CP_π). The CP_π gate is the one who acts on both qubits, and who produces entanglement between the input qubits A and B.

related. This national research project aims at producing, controlling, and detecting electronic flying qubits. During this internship, we have focused on the determination of a qubit's state by tomography, and on the entanglement generated by interactions during two-electron collisions. For that matter, it was of course useful to spend some time describing the type of electronic excitations used in the experiments in order to make these flying qubits. Thus, we have introduced the notion of Leviton, this quasi-particle able to fly over the Fermi sea without disturbing it. Finally, we presented the concept of railroad qubit, and showed how suitable it was to imagine a universal quantum computer relying on Levitonic flying qubits. This motivates the necessity to quantitatively understand electron entanglement in electron quantum optics, as quantum circuits - like the one studied in the example - would require to entangle flying qubits.

Let's now present the first task realized during the internship. The next section is dedicated to the notion of first-order electronic coherence, and the amelioration of a quantum tomography protocol to determinate the quantum state of an electronic excitation.

3 First-order coherence and quantum tomography protocols

In this section, we will focus on the first problem studied during this internship: the development of an efficient quantum tomography protocol for a single electronic excitation's wave-function in a mesoscopic conductor.

As its name suggests, quantum tomography is a method to determinate the state of a quantum object by combining successive images of it, taken under different angles, similarly to a medical PET scan. However, the object we want to know here - an electronic wave-function - does not live in the physical lab, but rather in a mathematical Hilbert space. Then, the idea is not to obtain a real image of the wave-function (which would not really make sense), but a theoretical picture of it, called the *Wigner representation* of its first-order coherence function. Given that this representation lives in the abstract *time-frequency space*, the successive "images" of the wave-function are not 2D-photographs like in the medical case, but rather 1D-slices representing the shape of the electronic excitation in this abstract space at different time and energy values.

In order to study such a protocol, we will first need to introduce the mathematical tool describing the physics of single-electron states in a mesoscopic conductor. As in Glauber's quantum optics, this object is called the *electronic first-order coherence function*, noted $\mathcal{G}^{(e)}$. In the first part of this section, we will thus give the definition and some useful properties of the $\mathcal{G}^{(e)}$ function, as well as of its Wigner representation. Then, we will explain the principle of two fundamental components in electron quantum optics: the quantum point contact and the mesoscopic capacitor. The first one plays the role of an ideal beam splitter for electrons, whereas the other one can be operated as an *on demand* electron source. These elements will be used to describe the existing quantum tomography protocol, and understand its limitations. Finally, the last paragraph of this section will present a more efficient protocol, developed during this internship, and based on the idea of *pulse-train* shaped excitations.

3.1 First-order electronic coherence

Before entering into the details of the quantum tomography protocol, it is important to establish the theoretical framework required to understand it. For that matter, we will start by giving in this subsection a quick overview of the central mathematical tool in EQO when it comes to studying single-electron states in a mesoscopic conductor: the first-order electronic coherence function.

3.1.1 The first-order electronic coherence function

As written before, the EQO's *electronic first-order coherence function* is the exact equivalent of the Glauber's first-order coherence function in bosonic quantum optics. In the same way that *coherence* classically describes the ability for two waves to interfere, the *electronic first-order coherence* quantifies the overlap between the detections of two electrons - described in the quantum fields theory formalism - at two given space-time points.

The so-called $\mathcal{G}^{(e)}$ function is a function of four arguments (**x**, t, **x'**, and t'), and depends on the reduced density matrix operator $\hat{\rho}$ for the electronic fluid. Mathematically, the electronic first-order coherence function is defined as follows:

$$\mathcal{G}^{(e)}_{\hat{\rho}}(\mathbf{x},t \mid \mathbf{x}',t') = \langle \hat{\psi}^\dagger(\mathbf{x}',t')\ \hat{\psi}(\mathbf{x},t)\rangle_{\hat{\rho}} = Tr\big(\hat{\psi}(\mathbf{x},t)\ \hat{\rho}\ \hat{\psi}^\dagger(\mathbf{x}',t')\big), \tag{2}$$

where $\hat{\psi}$ (respectively $\hat{\psi}^\dagger$) represents the annihilation (respectively creation) electronic field operator, creating an electronic excitation at a given space-time point. In equation (2), the $\langle\cdot\rangle_{\hat{\rho}}$ notation stands for the quantum expectation value of an operator over the quantum state described by the density matrix $\hat{\rho}$.

Contrary to the PQO case, where the reference state is the vacuum, the fermionic excitations in a mesoscopic conductor exist on top of the Fermi sea, which is then taken as the fermionic reference state (and is not empty at all!). Consequently, its coherence is *a priori* non-null, and is noted $\mathcal{G}^{(e)}_F$. This allows we to define the *electronic first-order excess coherence*, usually noted $\Delta\mathcal{G}^{(e)}_{\hat{\rho}}$, and corresponding to the electronic first-order coherence relatively to the Fermi sea. Thus, we can write:

$$\mathcal{G}^{(e)}_{\hat{\rho}}(\mathbf{x},t \mid \mathbf{x}',t') = \mathcal{G}^{(e)}_{F}(\mathbf{x},t \mid \mathbf{x}',t') + \Delta\mathcal{G}^{(e)}_{\hat{\rho}}(\mathbf{x},t \mid \mathbf{x}',t'). \tag{3}$$

Equation (3) is actually the formal definition of the *first-order excess coherence*. It is this notion that will be of interest for all EQO experiments performed with a metallic conductor. For example, we define the field operator annihilating (resp. creating) an electronic excitation described by the wave-function φ as $\hat{\psi}^{(\dagger)}[\varphi] = \int_{\mathbb{R}^4} d^3\mathbf{x}\; dt\; \varphi(\mathbf{x},t)\hat{\psi}^{(\dagger)}(\mathbf{x},t)$. We can now consider a state $|\Psi\rangle = \prod_{k=1}^{N} \hat{\psi}^{\dagger}[\varphi_k]\,|F\rangle$ composed of N mutually-orthogonal electrons described by the wave-functions $\{\varphi_1, ...\varphi_N\}$, and where $|F\rangle$ stands for the Fermi sea. Then, noting $\hat{\rho} = |\Psi\rangle\langle\Psi|$, it is possible to show that the first-order excess coherence function computed on the state $|\Psi\rangle$ is equal to:

$$\Delta\mathcal{G}^{(e)}_{\hat{\rho}}(\mathbf{x},t \mid \mathbf{x}',t') = \sum_{k=1}^{N} \varphi_k(\mathbf{x}',t')^{*}\varphi_k(\mathbf{x},t), \tag{4}$$

In the following, and in order to simplify the notations, we will consider that all the electrons move at the same speed in the mesoscopic conductor. This speed is called the *Fermi speed* and noted $\mathbf{v_F}$ ($\|\mathbf{v_F}\| = v_F$). It then allows us to choose a reference position $\mathbf{x_0}$ in the conductor, and to write $\mathbf{x} = \mathbf{x_0} + \mathbf{v_F}t$. This transformation changes the electronic first-order excess coherence function into a two-arguments function, which will be more convenient to read when the equations become longer:

$$\Delta\mathcal{G}^{(e)}_{\hat{\rho}}(\mathbf{x},t \mid \mathbf{x}',t') = \Delta\mathcal{G}^{(e)}_{\hat{\rho}}(\mathbf{x_0}+\mathbf{v_F}t, t \mid \mathbf{x_0}+\mathbf{v_F}t', t') := \Delta\mathcal{G}^{(e)}_{\hat{\rho}}(t \mid t'). \tag{5}$$

Now that the definitions are well established, let's relate the first-order electronic coherence to a measurable physical quantity. Actually, the only $\mathcal{G}^{(e)}_{\hat{\rho}}$-related quantity accessible to the experimentalist is the excess of coherence $\Delta\mathcal{G}^{(e)}_{\hat{\rho}}$. It is linked to $\langle i\rangle$, the quantum average of the electric current caused by the electronic excitation, by the relation:

$$\langle i(t)\rangle_{\hat{\rho}} = -ev_F\Delta\mathcal{G}^{(e)}_{\hat{\rho}}(t \mid t). \tag{6}$$

The quantum average on the electrical current i in equation (6) is a direct consequence of the quantum nature of $\Delta\mathcal{G}^{(e)}_{\hat{\rho}}$. To understand this expression further, we must precise that the current i considered here is defined as the difference between the total charge current in the measurement channel and the expectation value of the current due to the Fermi sea:

$$i(t) = -ev_F : \hat{\psi}^{\dagger}(t)\hat{\psi}(t) :, \tag{7}$$

where $: x : = x - \langle x\rangle_F$ refers to the fermionic normal order with respect to the Fermi sea. This way, the current i corresponds exactly to the "excess of current" created by an electronic excitation in the measurement channel. Combining definition (7) of the averaged electrical current $\langle i\rangle$ with definition (3) of $\Delta\mathcal{G}^{(e)}_{\hat{\rho}}$, it becomes clear that we have relation (6). It is interesting to insist on the fact that, according to equation (6), only the *diagonal* part of the first-order coherence excess - meaning the couples of space-time points such that $(\mathbf{x}',t') = (\mathbf{x},t)$ - is accessible experimentally by measuring the average current $\langle i\rangle$. This restricts considerably the regions where $\Delta\mathcal{G}^{(e)}_{\hat{\rho}}$ can be deduced from the experiment.

While this so-called *temporal representation* of the first-order electronic coherence function gives precious information about the real-time dynamics of the system we study, it does not say anything about the energetic side of the problem. However, the energy of a system is directly related to its frequency. As time and frequency are conjugated quantities, it is pretty easy to switch between the time- and the energy-representations using a double Fourier transform. Indeed, it is possible to define the *energy representation* of the first-order electronic excess coherence as follows:

$$\widetilde{\Delta\mathcal{G}}^{(e)}_{\hat{\rho}}(\omega \mid \omega') = \iint_{\mathbb{R}^2} dt\, dt'\, \Delta\mathcal{G}^{(e)}_{\hat{\rho}}(t \mid t')e^{i(\omega t - \omega' t')}, \tag{8}$$

where the $\widetilde{\cdot}$ notation designates the Fourier transform of the quantity under the tilde symbol, and (ω, ω') are the conjugate variables of (t, t'). As both time- and energy- representations are complementary, the first-order electronic excess of coherence expressed like in equation (8) allows us to obtain information about the nature of the electronic excitations observed in the channel. Indeed, this expression can - as an example - give the repartition of an electronic excitation in the frequency spectrum, granting access to the energy it carries. Experimentally, it is possible to access the diagonal part of $\widetilde{\Delta\mathcal{G}}^{(e)}$ by measuring $\langle i \rangle$ after an energy filter.

Given these two complementary representations of the same quantity, we could be tempted to seek a third *hybrid* way to look at the first-order electronic coherence, taking the best from each of the time- and the energy- representations.

3.1.2 The first-order electronic coherence's Wigner representation

The *Wigner representation* is a mixed time-frequency representation of the first-order electronic coherence. It simultaneously gives information about the real-time dynamics and the energy spectrum of the electronic excitation in the measurement channel. In the rest of the paragraph, and for practical reasons, we will use the variables $(\bar{t}, \tau)$ and their respective conjugates (Ω, ϖ) in the Fourier space, defined as follows:

$$\begin{cases} \bar{t} = \frac{t+t'}{2} \\ \tau = t - t' \end{cases} \quad \text{and} \quad \begin{cases} \Omega = \omega - \omega' \\ \varpi = \frac{\omega+\omega'}{2} \end{cases} \tag{9}$$

The new $\bar{t}$ and τ variables respectively correspond to the average time and the time difference between the previous variables t and t'. This is the same for the energy variables Ω and ϖ. Besides, we have the relation $\omega t - \omega' t' = \Omega \bar{t} + \varpi \tau$.

Mathematically, the Wigner representation $\mathcal{W}$ of a two-variables function F is a real-valued function, consisting in a Fourier transform of F with respect to one of its arguments. In the present case, we take the Fourier transform of $\mathcal{G}_{\hat{\rho}}^{(e)}$ with respect to its second variable (τ) to obtain the definition of the *Wigner representation of the first-order electronic coherence*:

$$\mathcal{W}_{\hat{\rho}}^{(e)}(\bar{t}, \varpi) = v_F \int_{\mathbb{R}} d\tau \; \mathcal{G}_{\hat{\rho}}^{(e)}(\bar{t} \mid \tau) e^{i\varpi\tau} = v_F \int_{\mathbb{R}} \frac{d\Omega}{2\pi} \; \widetilde{\mathcal{G}}_{\hat{\rho}}^{(e)}(\Omega \mid \varpi) e^{-i\Omega\bar{t}}. \tag{10}$$

Similarly, applying the same transformation to the first-order electronic excess coherence gives $\Delta\mathcal{W}_{\hat{\rho}}^{(e)}$, the *Wigner representation of the first-order electronic excess coherence*:

$$\Delta\mathcal{W}_{\hat{\rho}}^{(e)}(\bar{t}, \varpi) = v_F \int_{\mathbb{R}} d\tau \Delta\mathcal{G}_{\hat{\rho}}^{(e)}(\bar{t} \mid \tau) e^{i\varpi\tau} = v_F \int_{\mathbb{R}} \frac{d\Omega}{2\pi} \widetilde{\Delta\mathcal{G}}_{\hat{\rho}}^{(e)}(\Omega \mid \varpi) e^{-i\Omega\bar{t}}. \tag{11}$$

The reason why the Wigner representation is so widely used in practice, besides its ability to give a more intuitive interpretation of the manipulated objects, is that its marginal distributions can easily be linked to measurable physical quantities. Indeed, integrating $\Delta\mathcal{W}_{\hat{\rho}}^{(e)}$ over the frequencies ϖ directly gives access to the averaged excess current $\langle i \rangle$ (defined as in equation (7)) expressed in electric charge units, giving the following relation:

$$\int_{\mathbb{R}} \frac{d\varpi}{2\pi} \Delta\mathcal{W}_{\hat{\rho}}^{(e)}(\bar{t} \mid \varpi) = \frac{1}{-e} \langle i(\bar{t}) \rangle_{\hat{\rho}}. \tag{12}$$

Reciprocally, integrating $\Delta\mathcal{W}_{\hat{\rho}}^{(e)}$ over the time $\bar{t}$ on a time interval of duration T gives, in the limit $T \to +\infty$, the excess quantum occupation number at the frequency ϖ with respect to the Fermi sea:

$$\lim_{T\to\infty} \int_{-\frac{T}{2}}^{\frac{T}{2}} d\bar{t} \; \Delta\mathcal{W}_{\hat{\rho}}^{(e)}(\bar{t} \mid \varpi) = \Delta f(\varpi). \tag{13}$$

Here, the number $\Delta f(\varpi)$ corresponds to the fraction of the system's levels of energy $E = \hbar\varpi$ that are filled without the Fermi sea's contribution, hence the name of *excess quantum occupation number* for the function f. This means that in the stationary case (without any excitation), all the levels with a negative energy will be such that $\mathcal{W}_{\hat{\rho}}^{(e)}(\bar{t} \mid \bar{\omega}) = 1$ - meaning completely filled levels ; whereas the positive-energy levels will correspond to $\mathcal{W}_{\hat{\rho}}^{(e)}(\bar{t} \mid \bar{\omega}) = 0$ - so completely empty levels.

Finally, another advantage of the Wigner representation is its ability to tell whether the system it represents can be described classically, or if we must use the quantum formalism to understand it. Indeed, the Wigner representation can be seen - when it is used to describe fermions - as a distribution of quasi-probability. It is a consequence of Pauli's exclusion principle, as the occupation number of a fermionic energy level is necessarily inferior to 1. Basically, this means that the Wigner representation of a classical fermionic system will takes its values between 0 and 1 (just like a standard distribution of probability), whereas for a quantum system, we will observe negative values or values bigger than one in the representation.

To conclude this paragraph, figure 5 depicts the Wigner representation of a T-periodic train of electronic excitations, emitted by a device called a *mesoscopic capacitor* and functioning as an *on demand* electron source (more details about this device will be given in the following paragraph). The x-axis represents the time in period units (ft, where $f = \frac{1}{T}$ is the frequency of the mesoscopic capacitor's regime and t is the absolute time), while the y-axis gives the energy in Δ units, where Δ is the gap between two consecutive energy levels in the mesoscopic capacitor (see next section). By convention, the Fermi energy is set to 0.

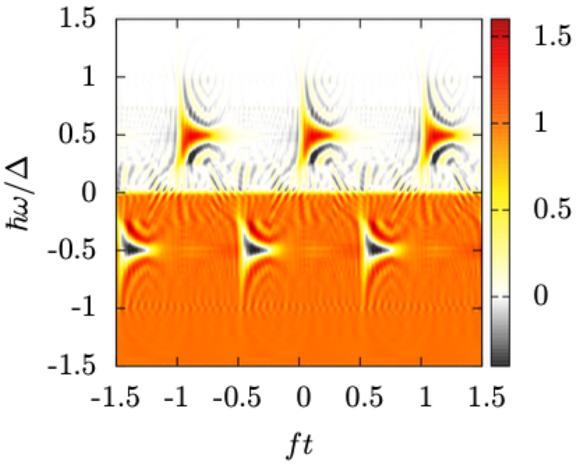

Figure 5: Wigner representation of three operating cycles of a mesoscopic capacitor (from [26]). A single period is composed of the successive emission of a hole ($\hbar\omega < 0$) and an electron ($\hbar\omega > 0$) excitations. In the Wigner representation, the Fermi sea is represented by an orange background as all the energy levels under the Fermi surface are filled. On the contrary, the levels above the Fermi surface are empty, and correspond to the white background.

In this figure, we can first notice that the electronic excitations definitely have a quantum nature, as their Wigner representation takes values in $[-0.5, 1.5]$. Besides, the orange background (representing the filled levels of the Fermi sea) contrasts with the white background (corresponding to empty levels), confirming what we said previously after equation (13). Let's now focus on the excitations themselves. It is clear, looking at the x-axis, that each period of the mesoscopic capacitor's regime produces two excitations: a first one above the Fermi sea, and a second one under it. Going further in the analysis, we notice that the first excitation is mainly composed of a positive-valued blob, that we will interpret as an *electron* flying over the Fermi sea. On the other hand, the excess of coherence of the second excitation is negative (with respect to the Fermi sea, this means that the coherence is inferior to 1), which can be interpreted as a *hole* in the Fermi sea. Finally, the interference fringes we can observe near the surface of the Fermi sea are due to the operating cycle of the source: its period is too short for the electron and the hole to completely escape the source during each cycle. This causes the emission of a superposition of coherent electron-hole excitations, causing these fringes.

All the theoretical tools needed to describe the single-particle physics in a mesoscopic conductor have now been presented. The next subsection will then be dedicated to the description of an experimental protocol allowing to determinate in a laboratory the first-order electronic excess coherence function of an excitation propagating in a measurement channel.

3.2 Hong-Ou-Mandel tomography protocol

A natural question regarding single electronic excitations in a mesoscopic conductor is: how to experimentally determine their quantum state? This subsection describes a quantum tomography protocol allowing the reconstruction of an excitation's first-order excess of coherence (or its Wigner representation). The analysis of this function then leads to the determination of the wave-function of the excitation.

3.2.1 The quantum point contact and the mesoscopic capacitor

While the PQO experiments are typically conducted in the vacuum or in the air, the standard background for EQO experiments is a 2D electron gas (2DEG) in a delimited area. When a 2DEG is submitted to a perpendicular magnetic field, chiral edge channels are created along its perimeter. These channels are a direct consequence of the quantum Hall effect, and their physics won't be detailed in this document. We simply needs to know that, in first approximation, electronic excitations can propagate ballistically in these channels, making them the electronic analog of optical fibers in photonics.

The quantum point contact

The most crucial competence in photon quantum optics is probably the ability to control the propagation of a photon, and to delocalize it onto different optical paths. This leads, for example, to single-photon interferences. In this sense, a basic of photonic quantum optics is the beam splitter. The analog of this device in EQO is called the *quantum point contact* (QPC), and its schematic representation is given in figure 6.

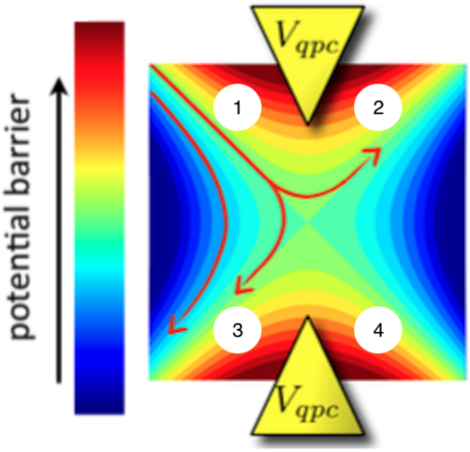

Figure 6: Schematic representation of a quantum point contact (from [7]). The colormap shows the potential in the 2DEG around the QPC.The two yellow spikes represent the electrodes submitted to a voltage V_{qpc}. Two types of excitation trajectories are represented by red arrows. First, an arrow going from input channel 1 to output channel 2 illustrates the case of an excitation crossing the potential barrier by tunneling. On the other hand, two arrows go from input channel 1 to output channel 3, showing two trajectories of electrons reflected by the potential barrier, unable to cross the QPC.

A QPC is a set of two electrodes facing each other, and submitted to a negative potential V_{QPC} (see figure 6). The idea is that this potential will create, *via* Coulomb repulsion, an energetic barrier for the electron propagating in the incoming edge channel 1. The height of this barrier is proportional to the potential V_{QPC}, and the higher the barrier, the lower the probability for the excitation to cross it by tunneling. Hence, it is possible to adjust the intensity of the applied potential in order to tune the proportion of electrons crossing the QPC.

Of course, the potential barrier created inside the QPC implies the quantum delocalization of the incoming electronic excitations. This way, a single excitation can be delocalized and simultaneously exit the QPC by different channels. Let's take the example of a value of V_{QPC} such that the transmission coefficient of the QPC is equal to 0.5. In this case, a single electronic excitation incoming in channel 1 will be equally delocalized onto channels 2 and 3: a part of it will be unable to cross the QPC and be reflected in channel 3, while the other part will tunnel through the potential barrier and exit in channel 4. This is exactly what a balanced photonic beam splitter would do with an incoming photon, and this is why the QPC is the electronic equivalent of the beam splitter.

Using this principle, several single-particle and two-particle interferences experiments have been realized with electrons. Two of them marked the experimental foundations of EQO: the demonstration of the electronic Hanbury Brown-Twiss [7] and Hong-Ou-Mandel [6] effects.

The mesoscopic capacitor

Then, it seems pretty logical that in order to study a single electron propagating in a mesoscopic conductor, we will need a source able to produce single electronic excitations. In EQO, such a source is called a *mesoscopic capacitor* and has first been developed in 2006 by G. Fève [13]. This particular single electron source allows the experimentalist to control, for example, the energy at which the electron is emitted or the characteristic duration of the wave packet that describes it.

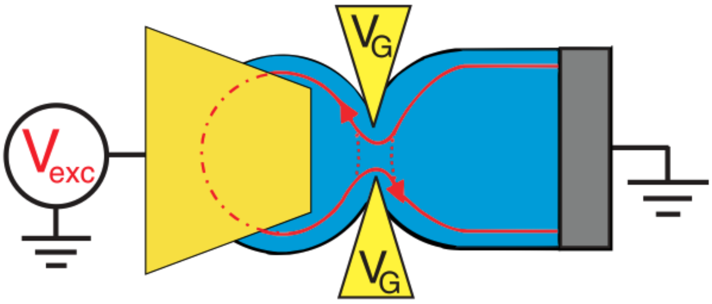

Figure 7: Schema of a mesoscopic capacitor (from [13]). The blue area represents the 2DEG. The yellow trapezoid on the left of the figure is the capacitor's top-gate, capacitively coupled to the 2DEG. The two yellow spikes in the center represent the QPC, separating the 2DEG into two zones: the quantum dot's cavity (which is also the bottom-gate of the capacitor) on the left, and the electron reservoir on the right. Finally, the gray rectangle on the right of the figure is the Ohmic contact imposing a potential to the 2DEG.

The principle of a mesoscopic capacitor is to isolate a small island of 2DEG, called *quantum dot* (the round blue zone in figure 7), from the rest of the 2DEG thanks to a QPC at a negative potential V_G (the two yellow spikes in figure 7). This quantum dot constitutes the first plate of the capacitor giving its name to the source. As the electrons in the quantum dot are confined, their energy is quantized. By applying a potential V_{exc} to the dot with an electrode (the second plate of the capacitor, in yellow in figure 7), we can shift the energy levels of the electrons located in the quantum dot. Calling Δ the gap between two consecutive energy levels (Δ is a function of the dot's size), it is possible to raise the level of the Fermi sea in the dot in such a way that only the highest energy level in the dot ends higher than the Fermi level of the 2DEG. The single electron occupying this level is then able to exit the quantum dot by tunneling and flies above the Fermi sea of the 2DEG. The operating cycle of the mesoscopic capacitor is represented in figure 8.

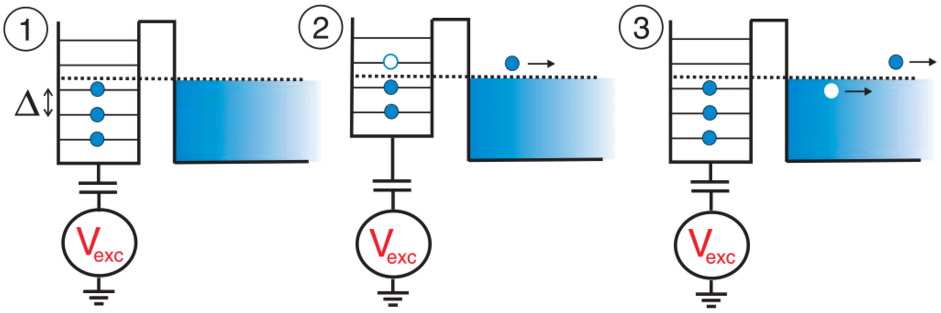

Figure 8: Operating cycle of a mesoscopic capacitor (from [14]). **(1)** The potential in the cavity is equal to the one of the Fermi sea in the electron reservoir. **(2)** A voltage is applied in the cavity, raising each electron to the energy level just above the one it occupied before. Thus, the single electron occupying the highest energy level becomes higher than the Fermi level and tunnels through the potential barrier imposed by the QPC: it flies over the Fermi sea, leaving a hole in the cavity behind it. **(3)** The voltage in the cavity come back to its initial value. An electron from the Fermi sea tunnels to the cavity to fill the empty level left by the flying electron. This is equivalent to the emission of a hole by the cavity. The cycle can now go on again.

In step 1, $V_{exc} = 0$ so that the level of the Fermi sea is the same in the dot than out of it. In step 2, we set the potential at $V_{exc} = \Delta$ so that all the electrons in the dot are shifted on the energy level right above the one they occupied before. This way, only the most energetic electron of the dot is shifted above the level of the Fermi sea in the 2DEG. The electron then tunnels through the potential barrier of height V_G created by the QPC. It is emitted above the Fermi sea in the 2DEG. Finally, the potential in the dot is decreased and comes back to 0 in step 3. This implies that an electron tunnels form the 2DEG into the quantum dot in order to fill the empty level left by the electron emitted in step 2: this is equivalent to emitting a hole excitation into the 2DEG's Fermi sea, as represented in the last step of figure 8. At the end of the day, a single operating cycle of the mesoscopic capacitor produces an electronic excitation (above the Fermi sea) during the first half of the period, and a hole (under the Fermi sea) during the second half. This is exactly what we observe in figure 5, which depicts three periods of the mesoscopic capacitor.

Now that we understand how a single electronic excitation source works, it is high-time to explore the details of the quantum tomography protocol designed to experimentally reconstruct the excitations emitted by such a device.

3.2.2 Experimental setup and theory

The basic idea behind this tomography protocol is to exploit two-particle interferometry to access the single-electron coherence of an unknown excitation by comparing it with the one emitted by a tunable and well-known source.

The electronic Hong-Ou-Mandel interferometer

The experimental setup of the protocol is a fermionic analog of the Hong-Ou-Mandel interferometer [19] in photonic quantum optics. It is composed of two mesoscopic capacitors - acting as electronic sources -, and a quantum point contact - acting as a fermionic beamsplitter - separating two 2DEG areas in an AsGa substrate (see figure 9).

In figure 9, the chiral quantum Hall edge-channels created in the 2DEG are represented in blue and numbered from 1 to 4. The unknown *source electrons* are emitted by the source 1 controlled by the potential V_{exc1}, while the *probe electrons* are produced by he source 2 controlled by the potential V_{exc2}.

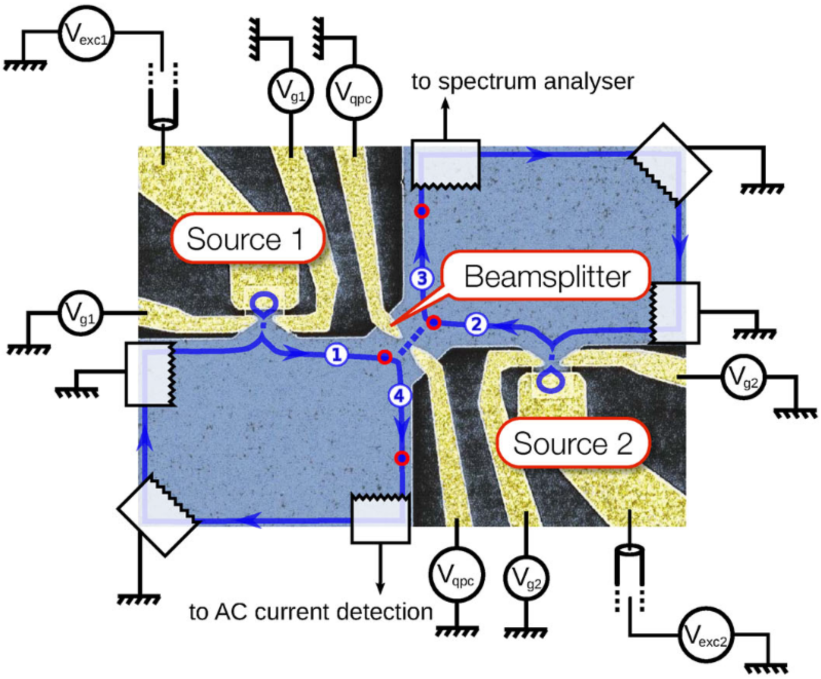

Figure 9: Schema of the quantum tomography setup (from [22]). The *source excitation* is created by source 1, and propagates to the central beam splitter through edge channel 1. On the other side of the device, the *probe excitation* is produced by source 2, and travels to the beam splitter *via* channel 2. If both excitations are emitted simultaneously, they meet at the beam splitter and interfere. Then, they exit the beam splitter in channels 3 and 4, where they are detected by a measurement process.

The excitations produced by each of the two sources travel in the 2DEG respectively along the incoming channels 1 and 2 before colliding at the beamsplitter. Then, they exit the beamsplitter in the outgoing channels 3 and 4.

When the *source* and the *probe* electrons arrive at the beamsplitter, the situation is analogous to the Hong-Ou-Mandel experiment [19]. In the historical 1987-experiment (considered as the fundamental experiment of quantum optics), the three authors observed that two interfering photons tend to exit the beamsplitter in the same output channel of the interferometer. A consequence of this *bunching* phenomenon, now called the Hong-Ou-Mandel effect, is the apparition of a dip in the coincidence rate after the interacting area. In the fermionic analog, the inverse phenomenon happens: a peak is observed in the coincidence rate. Indeed, electrons obey Pauli's exclusion principle and cannot occupy the same quantum state, so they tend to exit the beamsplitter in different channels, causing what we can call an *anti-bunching* phenomenon.

The measurement process takes place in channels 3 and 4, where we detect the *noise in current* signals created by the electronic excitations travelling in the channels after exiting the beamsplitter. In the next paragraph, we will explain how these measurement allow the experimentalist to reconstruct the Wigner representation $\Delta\mathcal{W}^{(e)}$ of the first-order electronic excess coherence, leading to the determination of the unknown excitation's wave-function.

Theoretical principle of the Hong-Ou-Mandel tomography

As seen in section 3.1, the Wigner representation $\Delta\mathcal{W}^{(e)}$ of an electronic excitation's first-order excess coherence is directly linked to the average current $\bar{i}$ and to the occupation number f (see equations (12) and (13)). However, these relations only give access to the time and energy distributions of the excitation, but not to the phase of its wave-function. The clue to all the necessary information about the excitation resides in the charge current's mathematical first moment: the *noise in current*. To be more accurate, we must define several quantities.

In the following, the set of n probe states produced by source 2 will be referred to as $\{P_n\}$, where P_n corresponds to the n^{th} probe state. We will actually be more interested in the *excess* of noise in current ΔS_i, defined for an electronic source as the difference between the noise in current detected when it is ON and when it is OFF: $\Delta S_i = S_{i,ON} - S_{i,OFF}$. However, as there are two sources in the setup presented previously, ΔS_i will actually be the sum of two terms here. The first one corresponds to the case when source 1 is ON and source 2 is OFF, and the second one when both sources are ON. In the first case, the noise in current is proportional to $\Delta\mathcal{W}_S^{(e)}$, the Wigner representation of the first-order excess coherence of the unknown source electron produced by source 1. In the second case, it is still proportional to $\Delta\mathcal{W}_S^{(e)}$ (as source 1 is ON), but also to $\Delta\mathcal{W}_{P_n}^{(e)}$, the Wigner representation of the first-order excess coherence of the n^{th} probe state. Then, we can show [5] that the total excess noise in current $\Delta S_{i,n}$ when the source electron S interferes with the n^{th} probe electron P_n is given by the following relation:

$$\Delta S_{i,n} = 2e^2\mathcal{T}(1-\mathcal{T})\int_{\mathbb{R}} \frac{d\omega}{2\pi}\left[\underbrace{\overline{\Delta\mathcal{W}_S^{(e)}(t,\omega)}^{t}\big(1-2f(\omega)\big)}_{[1]} - \underbrace{2\overline{\Delta\mathcal{W}_S^{(e)}(t,\omega)\Delta\mathcal{W}_{P_n}^{(e)}(t,\omega)}^{t}}_{[2]}\right]. \tag{14}$$

In equation (14), $\mathcal{T}$ is the transmission rate of the beamsplitter, $f(\omega)$ is the Fermi-Dirac distribution at $T \neq 0$, and the notation $\overline{\cdots}^{t}$ stands for the temporal average over time t. As mentioned earlier, term [1] accounts for the excess noise in current due to source 1 only, while term [2] corresponds to the noise in current resulting from the *anti-bunching* phenomenon between the source and the probe electrons when both sources are ON. This is why the latter term is proportional to the overlap between the two excess Wigner distributions.

The experimental approach of the present tomography protocol is to shape the probe excitations $\{P_n\}$ with sinusoidal voltage signals taking the form $V_{P_n}(t) = V_{DC} + V_{P_n}\cos(2\pi nft + \varphi)$. Here, V_{DC} is a bias voltage, f is the driving frequency, and φ is an arbitrary phase. Then, we work under the assumption that the Wigner representation of the source excitation has a Fourier decomposition: $\Delta\mathcal{W}_S^{(e)}(t,\omega) = \sum_{n\in\mathbb{Z}}\Delta\mathcal{W}_{S,n}^{(e)}(\omega)\exp(2i\pi nft)$. This assumption is clearly reasonable as we talk about a periodic physical signal. This way, when the probe electron P_n interferes with the source electron, it "selects" the source excitation's n^{th} harmonic $\Delta\mathcal{W}_{S,n}^{(e)}$. This harmonic can then be extracted from the $\Delta S_{i,n}$ signal thanks to equation (14). Proceeding like this for each probe excitation, it is theoretically possible to reconstruct $\Delta\mathcal{W}_S^{(e)}$ from the $\{\Delta S_{i,n}\}$ signals through the Fourier coefficients $\Delta\mathcal{W}_{S,n}^{(e)}$.

Of course, it is experimentally impossible to achieve an exact reconstruction with this method, as it would theoretically require an infinite number of probe excitations. However, it has been shown [5] that, due to the finite period of the unknown signal, a small number of harmonics ($N \sim 5$) already gives a very good approximation of it. Figure 10 shows the experimental determination of an electronic excitation's Wigner representation with only $N = 5$ harmonics (form $n = 0$ to $n = 4$).

The results presented in figure 10 correspond to the first experimental interpretztion of the previously explained protocol. Indeed, the unknown excitation was a Leviton initially produced by a Lorentzian voltage pulse of charge $q = -e$, which is a pretty well known case for which it is possible to predict what we are supposed to find. The Wigner representation was then reconstructed following the protocol, and with a set of five probe signals. The Fourier coefficients $\Delta\mathcal{W}_{S,n}^{(e)}$ of the source signal are plotted in figure 10 (**a**), and show a great agreement with the theoretical expectations. The reconstruction of the truncated Wigner representation ($N = 5$) is shown in figure 10 (**b**). As we can see, it takes values superior to 1 and inferior to 0, which is a sign of the source's quantum nature. Integrating the results of the reconstruction over ω, it is possible to deduce the voltage pulse that originally gave such a Wigner representation (see equation (12)): the shape of the pulse is the black dashed line represented in figure 10 (**b**). Clearly, the pulse deduced from the reconstruction exhibits a Lorentzian shape, which confirms the good results of the protocol in the test. Then, it is possible to deduce and extract the superposition of wave-functions corresponding to this Wigner representation (the so-called *atoms of signal*) thanks to an algorithm detailed

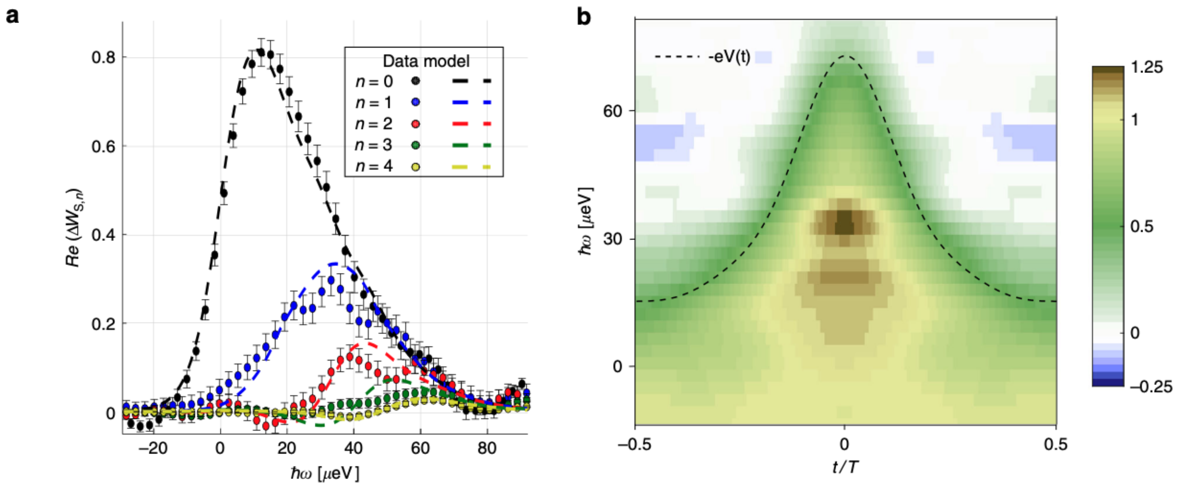

Figure 10: Reconstruction of a Leviton's Wigner distribution. (**a**) Real part of the Fourier coefficient of the excess Wigner distribution for the first five harmonics of the Fourier series. The dashed lines show the theoretical expectations, and are in very good agreement with the experimental results. (**b**) Excess Wigner distribution of the unknown electronic excitation (from [5]). The black dashed curve gives the temporal evolution of the energy resulting from the pulse that created the Leviton. We see an excellent agreement between the reconstructed Wigner distribution and the energy profile, proving the efficiency of the reconstruction method. Values of the Wigner distribution over 1 and below 0 are a sign that the excitation needs to be treated as a quantum signal.

in [24].

Even if the test seemed very successful in the Lorentzian case, we will show in the next paragraph that the present quantum tomography protocol suffers from several limitations, and needs to be improved.

3.2.3 Main drawbacks of the protocol

First, it is important to notice that although it is theoretically possible to reconstruct the signal coming from any shape of voltage pulses V_{exc1}, it remains impossible in practice to guarantee a good result in the general case. Indeed, applying this protocol to an arbitrary source signal would require an incredibly high number of measurement, taking a huge amount of time for the determination of a single source. To give a more quantitative idea of this protocol's time cost, let's consider a case similar to the previous example, with $N = 4$ and approximately 50 measurement points in energy for each harmonic. The total number of measures is then approximately equal to $10 \times 50 = 500$ (indeed, $N = 4$ corresponds to $n \in \{-4, ..., 4\}$, so roughly 10 harmonics). Each measure taking approximately 5 minutes, the type of results presented in figure 5 can then be obtained after almost 2 days of non-stop measurements. This is why it is necessary to work on an evolution of this quantum tomography protocol, and to find an optimal set $\{P_n\}$ that would be able to give satisfying results in the general case relatively quickly, and with a limited (and reasonable) number of probe signals.

Another expected drawback is that the Fourier coefficients of the Wigner representation $\widetilde{\Delta\mathcal{W}}^{(e)}_{S,n}$ we are able to deduce from the $\Delta S_{i,n}$ experimental measurements are not exactly those of the genuine time-frequency representation $\Delta\mathcal{W}^{(e)}_{S,n}$ of the source excitation. Indeed, what the experimentalist is able to compute with this method is actually a noisy convolution of $\Delta\mathcal{W}^{(e)}_{S,n}$ with a noise H_n depending on the temperature T and the form of the probe excitation P_n. This can be written in a vectorial form as follows:

$$\mathbf{\Delta\Sigma^{(e)}_{S,n}} = \mathbf{\hat{H}_n} \cdot \mathbf{\Delta\mathcal{W}^{(e)}_{S,n}} + \mathbf{N_n}, \tag{15}$$

where $\mathbf{\Delta\Sigma^{(e)}_{S,n}}$ is the vector of the experimental measurements, $\mathbf{\hat{H}_n}$ is the convolution matrix, $\mathbf{\Delta}\boldsymbol{\mathcal{W}}^{\mathbf{(e)}}_{\mathbf{S,n}}$ is the vector of the actual Fourier coefficient values we are looking for, and $\mathbf{N_n}$ is the noise vector. To be a little more precise, the coefficient of $\hat{H}_n$ corresponding to the frequency ω is equal to $h_n(\omega) = \frac{1}{2\pi nf}\big(f_{eq}(\omega-\pi nf) - f_{eq}(\omega+\pi nf)\big)$. At first glance, it seems pretty simple to extract $\mathbf{\Delta}\boldsymbol{\mathcal{W}}^{\mathbf{(e)}}_{\mathbf{S,n}}$ from $\mathbf{\Delta\Sigma^{(e)}_{S,n}}$ with a division in the Fourier space. However, as soon as the noise $\mathbf{N_n}$ takes value that are of the same order of magnitude (or even higher) as $\mathbf{\Delta}\boldsymbol{\mathcal{W}}^{\mathbf{(e)}}_{\mathbf{S,n}}$, this method would only amplify the noise contribution, and completely scramble the information on the signal we want to extract. The current version of the protocol is then based on a bayesian deconvolution algorithm, giving a maximum likelihood estimation of the solution, and relying on a prior information on the shape of the signal of interest $\mathbf{\Delta}\boldsymbol{\mathcal{W}}^{\mathbf{(e)}}_{\mathbf{S,n}}$. Besides, the results given by this algorithm also have to respect a constraint given by Cauchy-Schwarz inequality bounds on the variables n and ω [12].

The necessity of a prior information adds another difficulty in the search of reliability and robustness for the protocol. Added to its huge temporal cost, this increases the relevancy to look for a better version of it. The next subsection will show the work done during this internship to "improve" the Hong-Ou-Mandel quantum tomography protocol based on voltage pulse-trains.

3.3 Pulse-train tomography protocol

In the previous paragraph, we just saw the need for a set of probe signals that would allow, for a fixed number of them, to optimally probe the time-frequency space. Indeed, this would lead to an efficient determination of the excess Wigner representation $\Delta\mathcal{W}^{(e)}$ of the source excitation's first-order excess coherence function [24]. With this information, it is then simple to deduce $\Delta\mathcal{G}^{(e)}$, and the wave-function ψ to which it corresponds.

3.3.1 Theoretical principle of the pulse-train protocol

As we saw in the paragraph describing the mesoscopic capacitor, an electronic excitation is produced from a voltage signal V_{exc}, and its shape depends on the shape of the voltage pulse. The idea is now to consider coherent linear superpositions of the modes we used for the HOM protocol. However, we need to consider that the charge carried by each mode is small for this method to work, in order to have a valid approximation at order 1. The voltage signal $V_{exc2}(t)$ sent to produce the probe excitations then takes the form of a train of pulses $V_P(t)$:

$$V_{exc2}(t) = \sum_{l\in\mathbb{Z}} V_P(t-lT), \text{ with } V_P(t) = V_P\mathcal{F}_P\left(\frac{t}{\tau_0}\right) \tag{16}$$

In equation (16), T is the period of the pulse train, V_P is the amplitude of the pulse, $\mathcal{F}_P$ is a normalized pulse shape function such that $\int_{\mathbb{R}} \mathcal{F}_P(t)dt = 1$, and τ_0 is a parameter to tune the width of the pulse. This function is actually a wavelet resulting from the coherent linear superposition of the modes from the HOM protocol.

It is easy to show that the charge carried by a single pulse $V_P(t)$ is $Q_P = \frac{e^2 V_P \tau_0}{h}$. We then introduce the dimensionless parameter $q_P = \frac{Q_P}{-e}$ counting the charge carried by the pulse in electronic charges unity. It is this parameter that has to be small: we must impose $q_P \ll 1$.

As we usually work with energies more than with times, it is useful to compute the Fourier transform of such a pulse train:

$$\widetilde{V}_{exc2}(\omega) = -2\pi q_P \frac{hf}{e} \sum_{m\in\mathbb{Z}} \widetilde{\mathcal{F}_P}(2\pi m f\tau_0)\delta(\omega - 2\pi m f), \tag{17}$$

where $\widetilde{\cdots}$ stands for the Fourier transform, and $f = \frac{1}{T}$. The Fourier transform of the voltage pulse train is then a frequency comb of step $2\pi f$. Calling $\widetilde{\mathbf{V}}$ the vector of the frequency points at which $\widetilde{V}_{exc2}$ is taken, the equation replacing equation (15) (valid for the HOM protocol) now reads:

$$\mathbf{\Delta\Sigma^{(e)}_{S,n,\widetilde{V}}} = \left({}^{t}\widetilde{\mathbf{V}} \cdot \hat{\mathbf{H}}_{\mathbf{n}}\right) \cdot \mathbf{\Delta}\mathcal{W}^{(\mathbf{e})}_{\mathbf{S,n}} + \widetilde{\mathbf{V}} \cdot \mathbf{N_n}, \tag{18}$$

where $\mathbf{\Delta\Sigma^{(e)}_{S,n,\widetilde{V}}}$ is the vector of the experimental measures (now depending on $\widetilde{\mathbf{V}}$), and the notation ${}^{t}\cdot$ stands for the transpose vector. As $\widetilde{\mathcal{F}_P}(\omega) = \int_{\mathbb{R}} \mathcal{F}_P(t)e^{i\omega t}dt$, the normalization condition implies $\widetilde{\mathcal{F}}(0) = 1$, and as the voltage is a real quantity, we also have $\widetilde{\mathcal{F}}(-\omega) = \widetilde{\mathcal{F}}(\omega)^*$. Assuming that $|\widetilde{\mathcal{F}_P}(x)|$ rapidly decays to 0 when $|x| \geq 1$, we can then deduce the direct-current component V_{DC} of the voltage:

$$V_{DC} = \widetilde{V}_{exc2}(0) = -q_P\frac{hf}{e}. \tag{19}$$

In the following, we consider the case $f\tau_0 \leq 1$, so that many harmonics contribute to the pulse's spectrum and we really have a frequency comb. Indeed, in the opposite case $f\tau_0 \geq 1$, each pulse has a duration larger than the period T, and therefore only the first few harmonics (and ultimately only the first one in the case $f\tau_0 \gg 1$) significantly contribute to the spectrum.

Now that the pulse-train voltage is well defined, it is time to study its associated first-order electronic coherence function $\mathcal{G}^{(e)}_{V_{exc2}}$. In order to simplify the expressions, we define $\omega_{DC} = \frac{-eV_{DC}}{\hbar}$ the pulsation shift due to the DC component of the voltage, and $\mathcal{G}^{(e)}_{eq}$ the first-order electronic coherence function in the reference equilibrium state. As the equilibrium is by definition a stationary state, we have $\mathcal{G}^{(e)}_{eq}(t \mid t') = \mathcal{G}^{(e)}_{eq}(t-t' \mid 0) := \mathcal{G}^{(e)}_{eq}(t-t')$. This function obeys the following relation:

$$v_F\mathcal{G}^{(e)}_{eq}(t) = \frac{1}{2\pi}\int_{\mathbb{R}} d\omega\ f_{eq}(\omega)e^{-it}, \tag{20}$$

where f_{eq} is the Fermi-Dirac distribution at the equilibrium. It is then possible to show that the voltage's first-order electronic coherence function $\mathcal{G}^{(e)}_{V_{exc2}}$ evaluated at two arbitrary times t and t' is proportional to the coherence in the equilibrium state $\mathcal{G}^{(e)}_{eq}$ at time $t-t'$. The proportionality coefficient is simply a phase, which is the sum of two terms. The first one is called the *dynamical phase*, and corresponds to the phase acquired due to the propagation of the pulse train (compared to when we are at equilibrium). The second one is proportional to ω_{DC}, and depends on the time difference between t and t'. Concretely, if we define $\bar{t} := \frac{t+t'}{2}$ the average of the two times, and $\tau := t - t'$ the difference between them, we have $t = \bar{t} + \frac{\tau}{2}$ and $t' = \bar{t} - \frac{\tau}{2}$. Then, we can write:

$$\mathcal{G}^{(e)}_{V_{exc2}}\left(\bar{t} + \frac{\tau}{2} \mid \bar{t} - \frac{\tau}{2}\right) = e^{i\Delta\varphi_{AC}(\bar{t},\tau)}e^{-i\omega_{DC}\tau}\mathcal{G}^{(e)}_{eq}(\tau), \tag{21}$$

where $\Delta\varphi_{AC}$ is the dynamical phase, depending on $\bar{t}$ and τ. We can show that this phase reads as follows:

$$\Delta\varphi_{AC}(\bar{t},\tau) = -2q_P\sum_{m\in\mathbb{Z}^*}\widetilde{\mathcal{F}_P}(2\pi mf\tau_0)\frac{\sin(\pi mf\tau_0)}{m}e^{-2i\pi mf\bar{t}}. \tag{22}$$

From now on, we will only focus on the regime of small amplitude ($q_P \ll 1$), and try to compute the lowest non-trivial orders of $\mathcal{G}^{(e)}_{V_{exc2}}$ in q_P. In order to keep the parallel with the tomography protocol, we will focus on the excess of coherence $\Delta_{AC}\mathcal{G}^{(e)}_{V_{exc2}}$ defined as the coherence induced by the AC voltage compared to the case where only the DC component is applied. In the latter case, $\Delta\varphi_{AC}(\bar{t},\tau) = 0$ by definition, so we have:

$$\begin{aligned}\Delta_{AC}\mathcal{G}^{(e)}_{V_{exc2}}\left(\bar{t} + \frac{\tau}{2} \mid \bar{t} - \frac{\tau}{2}\right) &= e^{i\Delta\varphi_{AC}(\bar{t},\tau)}e^{-i\omega_{DC}\tau}\mathcal{G}^{(e)}_{eq}(\tau) - e^{-i\omega_{DC}\tau}\mathcal{G}^{(e)}_{eq}(\tau)\\ &= \left(e^{i\Delta\varphi_{AC}(\bar{t},\tau)} - 1\right)e^{-i\omega_{DC}\tau}\mathcal{G}^{(e)}_{eq}(\tau)\end{aligned} \tag{23}$$

The big advantage of the pulse train voltage is that the AC and DC parts are completely independent (see equation (21)). This allows the experimentalist to shift the associated Wigner distribution along the energy axis without changing its form simply by tuning the bias voltage of the pulse train. Without loss of generality, and in order to have shorter expressions, we thus consider in the following the case $V_{DC}=0$, meaning $\omega_{DC}=0$. The excess coherence then writes:

$$\Delta\mathcal{G}^{(e)}_{V_{exc2}}\left(\bar{t}+\frac{\tau}{2}\mid\bar{t}-\frac{\tau}{2}\right)=\left(e^{i\Delta\varphi_{AC}(\bar{t},\tau)}-1\right)\mathcal{G}^{(e)}_{eq}(\tau). \tag{24}$$

In the rest of this section, we study the first- and the second-order approximations (in q_P) of the first-order electronic excess of coherence function.

First-order approximation of the $\Delta\mathcal{G}^{(e)}$ function

At the first order in q_P, the excess coherence is simply given by:

$$\begin{aligned}\Delta\mathcal{G}^{(1e)(1)}_{V_{exc2}}\left(\bar{t}+\frac{\tau}{2}\mid\bar{t}-\frac{\tau}{2}\right)&=i\Delta\varphi_{AC}(\bar{t},\tau)\mathcal{G}^{(e)}_{eq}(\tau)\\&=-2iq_P\sum_{m\in\mathbb{Z}^*}\widetilde{\mathcal{F}_P}(2\pi mf\tau_0)\frac{\sin(\pi mf\tau_0)}{m}e^{-2i\pi mf\bar{t}}\mathcal{G}^{(e)}_{eq}(\tau).\end{aligned}\tag{25}$$

Finally, the associated Wigner distribution can now be computed, and we obtain:

$$\Delta\mathcal{W}^{(1e)(1)}_{V_{exc2}}(\bar{t},\overline{\omega})=-q_P\sum_{m\in\mathbb{Z}^*}\frac{\widetilde{\mathcal{F}_P}(2\pi mf\tau_0)}{|m|}e^{-2i\pi mf\bar{t}}g_{(-\pi|m|f,\pi|m|f)}(\overline{\omega}), \tag{26}$$

in which $g_{(\omega_1,\omega_2)}(\omega)=f_{eq}(\omega-\omega_2)-f_{eq}(\omega-\omega_1)$. At $T=0K$, $f_{eq}(\omega)=1-\Theta(\omega)$ gives $g_{(\omega_1,\omega_2)}(\omega)=\Theta(\omega-\omega_1)-\Theta(\omega-\omega_2)=\mathbb{1}_{[\omega_1,\omega_2]}$ the indicator function of the interval $[\omega_1,\omega_2]$:

$$\Delta\mathcal{W}^{(e)(1)}_{V_{exc2},T=0}(\bar{t},\overline{\omega})=-q_P\sum_{m\in\mathbb{Z}^*}\frac{\widetilde{\mathcal{F}_P}(2\pi mf\tau_0)}{|m|}e^{-2i\pi mf\bar{t}}\mathbb{1}_{[-\pi|m|f,\pi|m|f]}(\overline{\omega}), \tag{27}$$

It is important to notice in equation (26) that each harmonic m probes a limited portion of the frequency plane $(\overline{\omega},\Omega=2\pi mf)$, taking the form of horizontal bands of width $2\pi|m|f$ around $\overline{\omega}=0$. In order to better visualize the contribution of each term of the sum in equation (27), figure 11 gives the energy domain probed by each harmonic for $m\in\{-4,...,4\}$ at $T=0$.

It appears clearly in figure 11 that the higher the harmonic (in absolute value), the larger the probed slice of the frequency domain. Comparing figure 11 to the quadrant representation presented in figure 3 of [24], we see that the study at order 1 in q_P only gives information about the coherence between and electron and a hole, but not between two electrons or two holes.

At $T=0$, the indicator functions in (27) make the probed domains very sharp, but they tend to become smoother under the effect of temperature (due to the g function in equation (26)). Also, we must keep in mind that the bands in figure 11 are centered in $\overline{\omega}=0$ only because we considered the case $\omega_{DC}=0$. Indeed, we can show that the bands take non-zero values around $\overline{\omega}=\omega_{DC}$ in the general case. Depending on the area of the frequency plane we want to probe experimentally, we can then tune the value of V_{DC} and the number $|m|$ of harmonics we consider.

Second-order approximation of the $\Delta\mathcal{G}^{(e)}$ function

Let's now look at the second order approximation in q_P. Even though the tomography protocol relies on the first order approximation only, it is still interesting to investigate what information could the following order of approximation allow the access to. At this order, the first-order electronic coherence function $\Delta\mathcal{G}^{(e)}_{V_{exc2}}$ reads:

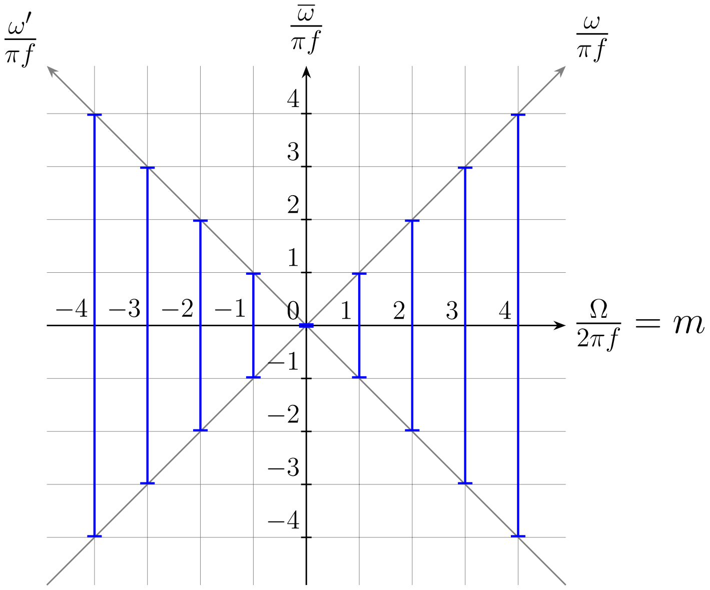

Figure 11: Localization of the pulse train's single-electron excess of coherence at the first order in q_P ($T = 0$, $\omega_{DC} = 0$) in the frequency plane $(\overline{\omega}, \Omega = 2\pi m f)$ for the first five harmonics ($m \in \{-4, ..., 4\}$). Each blue line represents the frequency domain probed by the m^{th} harmonic of the pulse train's excess of coherence. Taking $\omega_{DC} \neq 0$ results in the vertical translation of the blue lines such that they are all centered in $\overline{\omega} = \omega_{DC}$. We see that the higher the harmonic (in absolute value), the larger the probed domain in the frequency plane. We also notice that the frequency domains reached at this order correspond to the electron-hole coherences.

$$\Delta\mathcal{G}^{(1e)(2)}_{V_{exc2}}\left(\bar{t}+\frac{\tau}{2} \mid \bar{t}-\frac{\tau}{2}\right) = -\frac{1}{2}\big(\Delta\varphi_{AC}(\bar{t},\tau)\big)^2\mathcal{G}^{(e)}_{eq}(\tau \mid \tau). \tag{28}$$

Following the same scheme as for the first-order approximation, we can now compute the associated Wigner representation. The calculation gives:

$$\begin{aligned}\Delta\mathcal{W}^{(1e)(2)}_{V_{exc2}}(\bar{t},\overline{\omega}) =& \frac{q_P^2}{2}\sum_{k\in\mathbb{Z}^*}\sum_{m\neq k}\frac{\widetilde{\mathcal{F}_P}(2\pi k f\tau_0)\widetilde{\mathcal{F}_P}\big(2\pi(m-k)f\tau_0\big)}{k(m-k)}e^{-2i\pi m f t}\\ &\big[g_{(-\pi(2k-m)f,-\pi m f)}(\overline{\omega}) - g_{(\pi m f,\pi(2k-m)f)}(\overline{\omega})\big].\end{aligned} \tag{29}$$

Once again, the expression can be simplified in the case $T = 0$, and we can replace the g functions by indicator functions:

$$\begin{aligned}\Delta\mathcal{W}^{(1e)(2)}_{V_{exc2},T=0}(\bar{t},\overline{\omega}) =& \frac{q_P^2}{2}\sum_{k\in\mathbb{Z}^*}\sum_{m\neq k}\frac{\widetilde{\mathcal{F}_P}(2\pi k f\tau_0)\widetilde{\mathcal{F}_P}\big(2\pi(m-k)f\tau_0\big)}{k(m-k)}e^{-2i\pi m f t}\\ &\big[\mathbb{1}_{[-\pi(2k-m)f,-\pi m f]}(\overline{\omega}) - \mathbb{1}_{[\pi m f,\pi(2k-m)f)}(\overline{\omega})\big].\end{aligned} \tag{30}$$

As for the first-order approximation, figure 12 gives a visual interpretation of the energy domain probed by each harmonic. To be consistant with the experimental reality, we consider in the figure $k \in \{-5, ..., 5\}$. Indeed, limiting the voltage pulse to a linear combination of the five first harmonics is typically a good compromise to conserve enough components so that the shape of the pulse is conform to the shape of the wavelet$\mathcal{F}$, without going too far and conserving harmonics that almost don't contribute to the pulse. The red dotted lines in figure 12 are the graphical interpretation of the Cauchy-Schwarz bounds restricting the values of the coherence function [12]: out of the red-dotted square (only partially drawn in figure 12), the coherence is necessarily zero. Then the second-order approximation is compatible with these constraints, as it allows to probe areas located within the Cauchy-Schwarz bounds. Comparing figure 12 with the quadrant representation given in figure 3 of [24], we see that contrary to order 1, order 2 in q_P gives access to the electron-electron and to the hole-hole coherences.

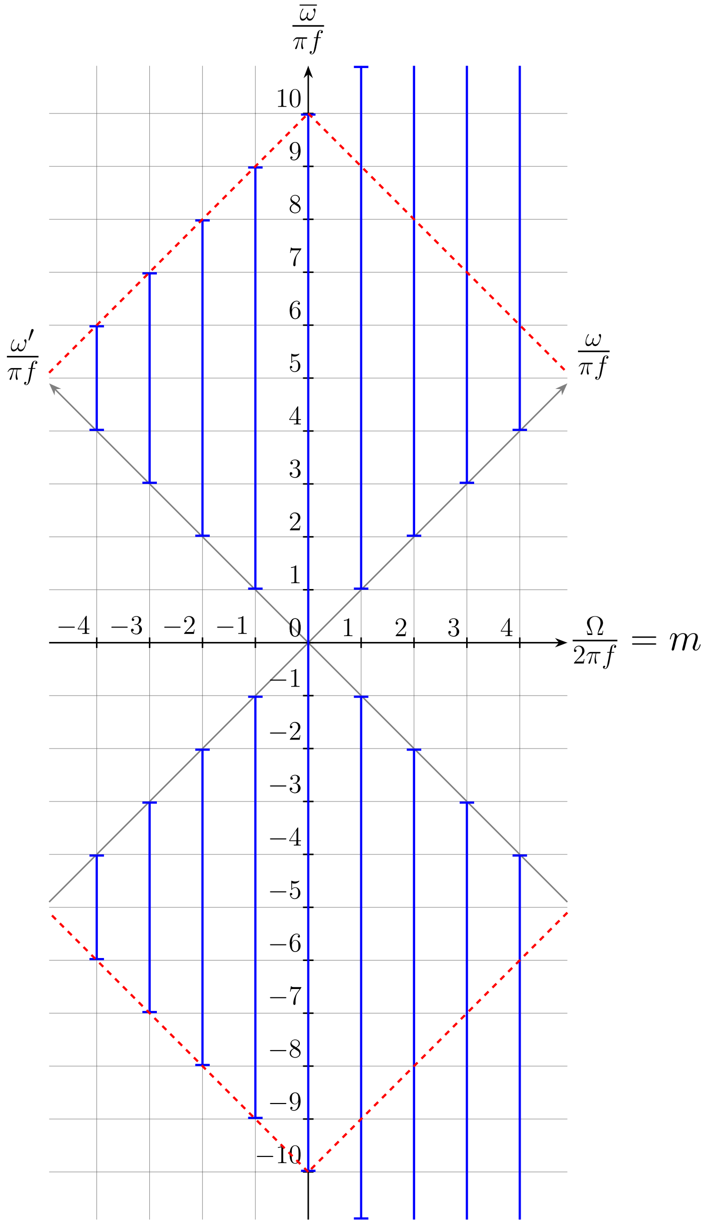

Figure 12: Localization of the pulse train's single-electron excess of coherence at the second order in q_P ($T = 0$, $\omega_{DC} = 0$) in the frequency plane ($\overline{\omega}, \Omega = 2\pi m f$) for the first five harmonics ($m \in \{-4, ..., 4\}$). Each blue line represents the frequency domain probed by the m^{th} harmonic of the pulse train's excess of coherence. The red dashed lines represent the Cauchy-Schwarz bounds (derived in [12]) restricting the area in which the coherence can be non-zero. This time, the frequency domains reached at the second order correspond to the electron-electron and hole-hole coherences.

This last remark is coherent with the results presented in [12] and that we explain here. When the Fermi sea is perturbed by a small-amplitude time-dependent voltage, the linear response of the Wigner distribution shows that the perturbation creates a charge current, but the average energy current remains null. But this latter current is proportional to the electronic occupation number at a given energy. Hence, this result proves that the electronic occupation number is not affected by the perturbation in the first-order approximation (linear response). Then, the first non-trivial contribution to the occupation number is at order 2, when the energy-current is affected by the perturbation. This explains why the electron-electron and hole-hole coherences, that change the occupation number, are not accessible when we only focus on the first-order, and only appear in the second-order study.

Actually, it has been shown that the flux of the energy carried by the electrons is similar to the power dissipated in a conductor of resistivity $\frac{R_K}{2}$, with $R_K = \frac{h}{e^2}$ the von Klitzing constant. In a sense, the result obtained at the second order in q_P is then a consequence of the Joule effect in a quantum conductor, where a fraction of the energy is dissipated in the contacts.

3.3.2 Example of a voltage pulse train

To conclude this section, let's check whether keeping only five-harmonics in the truncated Fourier series is generally a good approximation of the original wavelet. Let's take the example of a gaussian wavelet centered on $t = 0$, and of width $\tau_0 = 1ns$:

$$\mathcal{F}(t) = \frac{1}{\sqrt{2\pi}} \exp\left(-\frac{1}{2}\frac{t}{\tau_0}^2 \right) \tag{31}$$

As a reminder, we are in the approximation $f\tau_0 \ll 1$, so let's choose $f = 0.1GHz$ such that $f\tau_0 = 10^{-1}$. These values are taken as an example to show the forms of the pulses, and are not necessarily consistant with the real experimental values. In order to build a periodic pulse train based on the shape of $\mathcal{F}$, we consider the wavelet's Fourier transform $\widetilde{\mathcal{F}}$. Taking the truncated Fourier series of $\widetilde{\mathcal{F}}$ with a given number of terms, we obtain a periodic signal of which the period is an approximation of $\mathcal{F}$. Earlier, we mentioned that only the first five harmonics of the pulse were considered to build the pulse train experimentally. Figure 14 depicts the ponderation of the five harmonics used to generate the voltage pulse train.

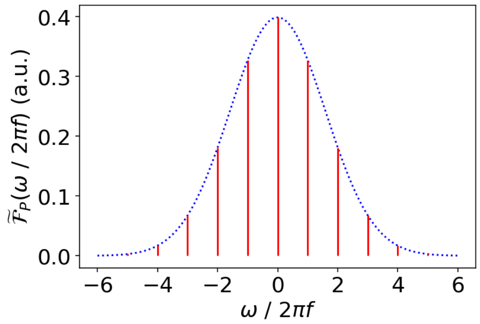

Figure 13: Ponderation of the five first harmonics used to construct the voltage pulse train. The blue curve represents the Fourier transform $\widetilde{\mathcal{F}}$ of the wavelet. The red spikes stand for the considered harmonics: their height is proportional to their contribution in the truncated Fourier series

Then, figure 14 shows the temporal profile of the pulse train created by taking different number of harmonics of $\widetilde{\mathcal{F}}$.This figure clearly demonstrates that taking $h = 5$ is a very good compromise between reliability and efficiency. Indeed, we see in figure 14 that $h = 5$ is the first value for which a period of the reconstructed pulse-train is a very good approximation of the original wavelet. Moreover, the plot for $h = 10$ is a proof that the gain between a reconstruction with five and ten harmonics is almost not perceivable.

Of course, a lot of work still needs to be done in order to develop a completely functional and efficient pulse-train tomography protocol, as no experimental tests have been done to this date. Nevertheless, the pulse-train idea looks very promising as it proposes a seemingly better alternative to the present "harmonic by harmonic" reconstruction of the source signal with the HOM protocol. Indeed, the lack of efficiency and tunability were the main problems of the HOM protocol. With the pulse trains, thanks to

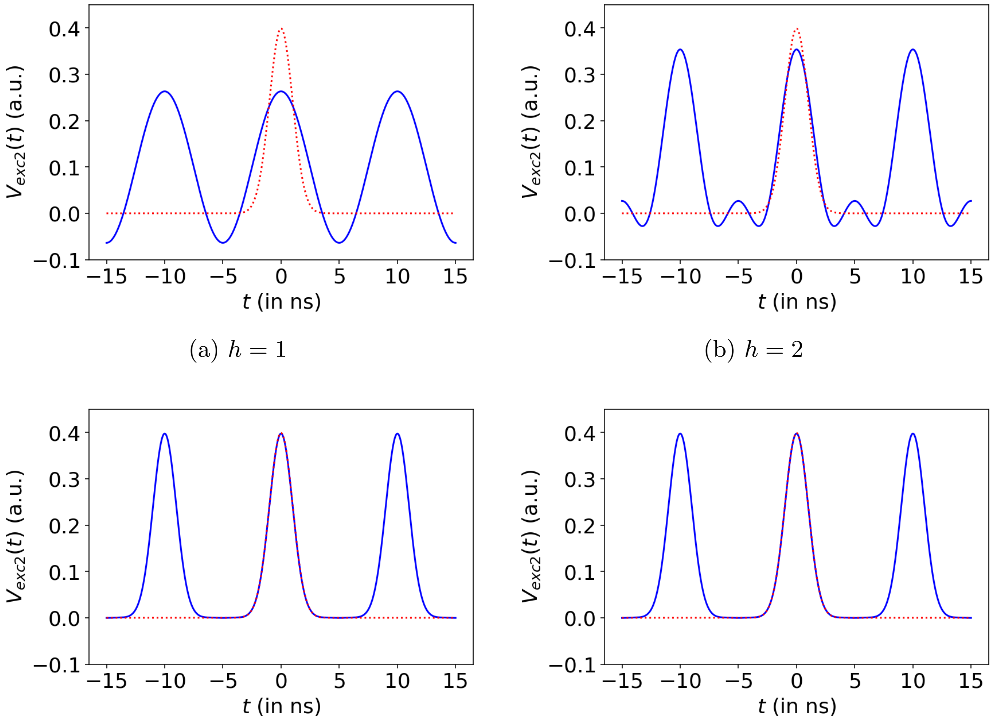

(a) $h = 1$

(b) $h = 2$

(c) $h = 5$

(d) $h = 10$

Figure 14: Reconstruction of the original wavelet with different numbers of harmonics (**(a)** $h = 1$, **(b)** $h = 2$, **(c)** $h = 5$, **(d)** $h = 10$). The blue curve represents the Fourier reconstruction with a number h of harmonics. The red dotted curve is the shape of the original wavelet we want to reproduce.

the roles of the bias voltage and the number of harmonics on the probed section of the frequency plane, the coherence function's determination seems to be much efficient. Contrary to what happens with the HOM tomography protocol, the experimentalist would not be forced to probe the whole plane in order to access the coherence localized in a given area. In that sense, the pulse-train protocol represents a great progress: for a given coherence function, the reconstruction would be much quicker than with the HOM protocol.

4 Second-order coherence and entanglement criteria

While the previous section focused on single electrons in a mesoscopic conductor, the last part of this document will deal with two-electron physics. Indeed, we will see in this section that going one step further, it is possible to study a typically quantum phenomenon called *entanglement*, arising as soon as we consider multi-particle states.

Quantum entangled states have first been theorized in 1935 by Einstein, Podolsky and Rosen in their famous EPR article [11]. Quantum particles are called entangled if they share information in such a way that measuring a quantity on one of them instantly gives information on the other. However, their existence beyond mathematics remained for decades at the heart of a metaphysical debate between Einstein and Bohr concerning the interpretation of quantum physics. It is only in the 1980's that Aspect gave the first irrefutable proof of quantum entanglement reality [1], by experimentally violating a mathematical criterion called a *Bell inequality* [2]. Entanglement is such an important and fertile concept that its experimental confirmation gave birth to what is now called the *second quantum revolution*, leading to the development of numerous fields of physics such as quantum computing, quantum information, or quantum cryptography.

Although entangled states are now relatively well understood for bosons (such as photons), it is very different for fermionic entangled states who have been seriously studied only recently. The beginning of this section will follow the same path as the previous one, as we will start by introducing the notion of *second-order electronic coherence function*, which is necessary to describe two-electron states. Similarly to the first-order function, we will present the definition and the main properties of the second-order electronic coherence function, as well as its representation in the Wigner time-energy space. Then, we will be ready to study quantum entanglement criteria, meaning mathematical inequalities that can tell whether a quantum state is entangled or not, depending on if it respects the criterion. Three criteria, based on the Cauchy-Schwarz inequality, have principally been studied during this internship. After briefly presenting the fundamentals of fermionic entanglement, we will present the criteria's expression in terms of spin-operators, and the interest of such a representation. Finally, we will study one of these criteria in the case of a scattered two-electron quantum state.

4.1 Second-order electronic coherence

In order to work on the two-electron states in a mesoscopic conductor, it is necessary to introduce the proper mathematical objects. In the present case, the main tool is simply a widely used extension of the first-order electronic coherence function, soberly called second-order electronic coherence function.

4.1.1 The second-order electronic coherence function

Once again, it is relevant to underline the parallel between PQO and EQO regarding the *second-order electronic coherence function*, as it is the exact analog of Glauber's second-order coherence function in standard quantum optics. This function of four space-time points, that we will note $\mathcal{G}^{(2e)}$, is defined as follows:

$$\begin{aligned}
&\mathcal{G}^{(2e)}_{\hat{\rho}}(\mathbf{x_1},t_1;\mathbf{x_2},t_2\,|\,\mathbf{x'_1},t'_1;\mathbf{x'_2},t'_2)\\
&\qquad = \langle \hat{\psi}^\dagger(\mathbf{x'_1},t_1)\,\hat{\psi}^\dagger(\mathbf{x'_2},t_2)\,\hat{\psi}(\mathbf{x_2},t_2)\,\hat{\psi}(\mathbf{x_1},t_1)\,\rangle_{\hat{\rho}} \qquad (32)\\
&\qquad = Tr\big(\hat{\psi}(\mathbf{x_2},t_2)\,\hat{\psi}(\mathbf{x_1},t_1)\,\hat{\rho}\,\hat{\psi}^\dagger(\mathbf{x'_1},t_1)\,\hat{\psi}^\dagger(\mathbf{x'_2},t_2)\big),
\end{aligned}$$

where $(\mathbf{x_1},t_1)$, $(\mathbf{x_2},t_2)$, $(\mathbf{x'_1},t'_1)$, and $(\mathbf{x'_2},t'_2)$ are the coordinates of the four space-time points at which the coherence is studied, and $\hat{\rho}$ is the electronic fluid's density operator. A way to interpret this definition is that the $\mathcal{G}^{(2e)}$ function quantifies the overlap between on one hand the two-electron state corresponding to the detection of two electrons at $(\mathbf{x_1},t_1)$ and $(\mathbf{x_2},t_2)$, and on the other hand the state corresponding to the detection of two electrons at $(\mathbf{x'_1},t'_1)$, and $(\mathbf{x'_2},t'_2)$.

In order to alleviate the notations, we consider here again that all the electrons in the conductor have the same velocity $\mathbf{v_F}$ ($||\mathbf{v_F}|| = v_F$), called the Fermi velocity. Choosing an arbitrary reference position $\mathbf{x_0}$, we can then express the $\mathcal{G}^{(2e)}$ function as a function of "only" four times as we have the relation $\mathbf{x} = \mathbf{x_0} + \mathbf{v_F}t$:

$$\begin{aligned}&\Delta\mathcal{G}^{(2e)}_{\hat\rho}(\mathbf{x_1},t_1;\,\mathbf{x_2},t_2\,|\,\mathbf{x'_1},t'_1;\,\mathbf{x'_2},t'_2)\\ &\quad=\Delta\mathcal{G}^{(2e)}_{\hat\rho}(\mathbf{x_0}+\mathbf{v_F}t_1,t_1;\,\mathbf{x_0}+\mathbf{v_F}t_2,t_2\,|\,\mathbf{x_0}+\mathbf{v_F}t'_1,t'_1;\,\mathbf{x_0}+\mathbf{v_F}t'_2,t'_2)\\ &\quad:=\Delta\mathcal{G}^{(2e)}_{\hat\rho}(t_1,t_2\,|\,t'_1,t'_2)\end{aligned}\tag{33}$$

As the fermionic reference state is not the vacuum like for the bosonic case, but the Fermi sea - which coherence $\mathcal{G}^{(2e)}_F$ is non-zero *a priori* -, we define the *second-order electronic excess of coherence function* $\Delta\mathcal{G}^{(2e)}$. This function is the commonly used quantity in practice, and corresponds to the intrinsic coherence of the two-electron state produced by the electronic source, without the contribution of the Fermi sea. However, the situation with a two-electron detection event is a little more complex than with one electron. Indeed, the detection of one electron can correspond to only two cases: either the electron comes from the Fermi sea, or it comes from the electronic source. This is why the first-order coherence can be written $\mathcal{G}^{(e)}_{\hat\rho} = \mathcal{G}^{(e)}_F + \Delta\mathcal{G}^{(e)}_{\hat\rho}$, distinguishing both cases. Regarding the detection of two electrons, three physical situations are possible:

- the Fermi sea lost two electrons;
- the electronic source lost two electrons;
- the electronic source and the Fermi sea lost one electron each.

Let's consider the two two-electron detection at times (t_1, t'_1) and (t_2, t'_2). As the two electrons are indistinguishable, we need to account for all the possible detection combinations, giving six terms. The second-order electronic excess of coherence then reads:

$$\begin{aligned}\mathcal{G}^{(2e)}_{\hat\rho}(t_1,t_2\,|\,t'_1,t'_2) = \;& \left.\mathcal{G}^{(2e)}_F(t_1,t_2\,|\,t'_1,t'_2)\right\}[1]\\ +\;& \left.\Delta\mathcal{G}^{(2e)}_{\hat\rho}(t_1,t_2\,|\,t'_1,t'_2)\right\}[2]\\ &\left.\begin{aligned}+\;& \mathcal{G}^{(e)}_F(t_1\,|\,t'_1)\,\Delta\mathcal{G}^{(e)}_{\hat\rho}(t_2\,|\,t'_2)+\mathcal{G}^{(e)}_F(t_2\,|\,t'_2)\,\Delta\mathcal{G}^{(e)}_{\hat\rho}(t_1\,|\,t'_1)\\ -\;& \mathcal{G}^{(e)}_F(t_1\,|\,t'_2)\,\Delta\mathcal{G}^{(e)}_{\hat\rho}(t_2\,|\,t'_1)-\mathcal{G}^{(e)}_F(t_2\,|\,t'_1)\,\Delta\mathcal{G}^{(e)}_{\hat\rho}(t_1\,|\,t'_2)\end{aligned}\right\}[3]\end{aligned}\tag{34}$$

In equation (34), term [1] corresponds to the case where the Fermi sea lost the two electrons involved in the detection. Term [2] is the second-order electronic excess coherence - of which equation (34) is actually the definition -, representing the case where the source gave the two detected electrons. Finally, term [3] stands for the four different possibilities where the Fermi sea lost one electron and the source lost the other.

Like for the first-order, it is possible to choose between several representations of the coherence function, depending on the context. While the previously introduced *time representation* of the $\Delta\mathcal{G}^{(2e)}$ function is useful when we are interested in the dynamics of the system, it can be relevant to switch to the energy domain if we want to study the nature of the electronic excitations. This *energy representation* is obtained by proceeding to a Fourier transform with respect to each of the time representation's four time variables:

$$\begin{aligned}&\widetilde{\Delta\mathcal{G}}^{(2e)}_{\hat\rho}(\omega_1,\omega_2\,|\,\omega'_1,\omega'_2)\\ &\quad= v_F^4\iiiint_{\mathbb{R}^4} dt_1\,dt_2\,dt'_1\,dt'_2\,\Delta\mathcal{G}^{(2e)}_{\hat\rho}(t_1,t_2\,|\,t'_1,t'_2)\,e^{i(\omega_1t_1+\omega_2t_2-\omega'_1t'_1-\omega'_2t'_2)}.\end{aligned}\tag{35}$$

In equation (35), the notation $\widetilde{\cdot}$ corresponds to the Fourier transform, and $(\omega_1, \omega_2, \omega_1', \omega_2')$ are the conjugated variables of (t_1, t_2, t_1', t_2') in the Fourier space. Let's now look at an hybrid representation of the second-order electronic excess of coherence function, living in the time-energy domain.

4.1.2 The second-order electronic coherence's Wigner representation

As mentioned just before, this subsection will focus on a particular representation of the $\Delta\mathcal{G}^{(2e)}$ function, giving simultaneously information about the dynamics and the nature of the considered electronic excitations: this is of course the Wigner representation we already introduced in the previous section of this document. For conveniency, we define new variables:

$$\begin{cases} \bar{t}_1 = \frac{t_1+t_1'}{2} \\ \tau_1 = t_1 - t_1' \end{cases} \quad \text{and} \quad \begin{cases} \bar{t}_2 = \frac{t_2+t_2'}{2} \\ \tau_2 = t_2 - t_2' \end{cases} \tag{36}$$

Consequently, the variables $(\Omega_1, \overline{\omega}_1, \Omega_2, \overline{\omega_2})$ are the respective conjugated variables of $(\bar{t}_1, \tau_1, \bar{t}_2, \tau_2)$, and read:

$$\begin{cases} \Omega_1 = \omega_1 - \omega_1' \\ \overline{\omega}_1 = \frac{\omega_1+\omega_1'}{2} \end{cases} \quad \text{and} \quad \begin{cases} \Omega_2 = \omega_2 - \omega_2' \\ \overline{\omega}_2 = \frac{\omega_2+\omega_2'}{2} \end{cases} \tag{37}$$

With the newly-defined variables, the time- and energy- representation of the second-order electronic coherence function then write:

$$\begin{cases} \mathcal{G}^{(2e)}_{\hat{\rho}}(t_1, t_2 \,|\, t_1', t_2') = \mathcal{G}^{(2e)}_{\hat{\rho}}\left(\bar{t}_1 + \frac{\tau_1}{2}, \bar{t}_2 + \frac{\tau_2}{2} \,|\, \bar{t}_1 - \frac{\tau_1}{2}, \bar{t}_2 - \frac{\tau_2}{2}\right) \\ \widetilde{\mathcal{G}}^{(2e)}_{\hat{\rho}}(\omega_1, \omega_2 \,|\, \omega_1', \omega_2') = \widetilde{\mathcal{G}}^{(2e)}_{\hat{\rho}}\left(\overline{\omega}_1 + \frac{\Omega_1}{2}, \overline{\omega}_2 + \frac{\Omega_2}{2} \,|\, \overline{\omega}_1 - \frac{\Omega_1}{2}, \overline{\omega}_2 - \frac{\Omega_2}{2}\right). \end{cases} \tag{38}$$

All the notations are now introduced to define the Wigner representation of the second-order electronic coherence function. The Wigner distribution is basically a "partial" Fourier transform (resp. inverse Fourier transform) with resect to two of the four variables of the time- (resp. energy-) representation of the coherence function:

$$\begin{aligned} &\mathcal{W}^{(2e)}_{\hat{\rho}}(\bar{t}_1, \overline{\omega}_1 \,|\, \bar{t}_2, \overline{\omega}_2) \\ &\quad = v_F^2 \iint_{\mathbb{R}^2} d\tau_1\, d\tau_2\, \mathcal{G}^{(2e)}_{\hat{\rho}}\left(\bar{t}_1 + \frac{\tau_1}{2}, \bar{t}_2 + \frac{\tau_2}{2} \,|\, \bar{t}_1 - \frac{\tau_1}{2}, \bar{t}_2 - \frac{\tau_2}{2}\right) e^{i(\overline{\omega}_1\tau_1 + \overline{\omega}_2\tau_2)} \\ &\quad = \frac{1}{v_F^2} \iint_{\mathbb{R}^2} \frac{d\Omega_1}{2\pi} \frac{d\Omega_2}{2\pi}\, \widetilde{\mathcal{G}}^{(2e)}_{\hat{\rho}}\left(\overline{\omega}_1 + \frac{\Omega_1}{2}, \overline{\omega}_2 + \frac{\Omega_2}{2} \,|\, \overline{\omega}_1 - \frac{\Omega_1}{2}, \overline{\omega}_2 - \frac{\Omega_2}{2}\right) e^{-i(\Omega_1\bar{t}_1 + \Omega_2\bar{t}_2)}. \end{aligned} \tag{39}$$

Of course, it would also have been possible to perform the two Fourier transforms over the couples of variables $(\bar{t}_1, \bar{t}_2)$ and $(\overline{\omega}_1, \overline{\omega}_2)$ to obtain the Wigner distribution $\mathcal{W}^{(2e)}_{\hat{\rho}}(\Omega_1; \tau_1 \,|\, \Omega_2; \tau_2)$. Finally, the Wigner representation of the second-order electronic *excess* of coherence $\Delta\mathcal{W}^{(2e)}$ can easily be defined by replacing $\mathcal{G}^{(2e)}_{\hat{\rho}}$ (resp. $\widetilde{\mathcal{G}}^{(2e)}_{\hat{\rho}}$) with $\Delta\mathcal{G}^{(2e)}_{\hat{\rho}}$ (resp. $\Delta\widetilde{\mathcal{G}}^{(2e)}_{\hat{\rho}}$) in equation (39).

Now that we are armed to face the mesoscopic conductor's two-electron physics, let's see in next subsection how the $\mathcal{G}^{(e)}$ and $\mathcal{G}^{(2e)}$ functions can be useful to study entanglement in an EQO system.

4.2 Two-electron entanglement criteria

As mentioned in this section's introduction, studying two-electron states in a quantum system opens a lot of doors regarding the notion of entanglement. In this whole subsection, the goal will be to derive and study several entanglement criteria based on the Cauchy-Schwarz inequality.

4.2.1 The basics of fermionic entanglement

We will start by giving the most important concepts and results of a mathematical theory of fermionic entanglement. Indeed, working with fermions sets a certain number of constraints to respect, and requires to make some changes in the "standard" mathematical framework.

Fermionic antisymmetry

The first fundamental difference is a direct consequence of Pauli's exclusion principle, that induces the fermionic many-body wave-functions' antisymmetry. Indeed, let's consider the example of two-mode states. A bosonic state $|\Psi\rangle_b$ with a particle in a certain mode A and another in a mode B reads:

$$\begin{aligned} |\Psi\rangle_b &= |A\rangle \otimes |A\rangle = \hat{a}_A^\dagger \hat{a}_B^\dagger |0\rangle \\ &= |B\rangle \otimes |A\rangle = \hat{a}_B^\dagger \hat{a}_A^\dagger |0\rangle , \end{aligned} \tag{40}$$

where $\hat{a}_\lambda$ (resp. $\hat{a}_\lambda^\dagger$) is the bosonic annihilation (resp. creation) operator in the channel λ. Hence, as $|A\rangle \otimes |B\rangle = |B\rangle \otimes |A\rangle$, the commutativity of the tensor product directly implies the bosonic commutation relation $[\hat{a}_A^\dagger, \hat{a}_B^\dagger] = 0$. However, fermions obey the anti-commutation relation $\{\hat{c}_A^\dagger, \hat{c}_B^\dagger\} = 0$. This implies that in order to correctly describe multi-modes fermionic states, we need an anti-symmetric operation: the tensor product needs to be replaced. To that end, we choose the exterior product, defined as $|x\rangle \wedge |y\rangle = \frac{1}{2}\big(|x\rangle \otimes |y\rangle - |y\rangle \otimes |x\rangle \big)$. This solves our problem, as we now have $|x\rangle \wedge |y\rangle = -|y\rangle \wedge |x\rangle$. Consequently, the same state written in terms of fermions will read:

$$\begin{aligned} |\Psi\rangle_f &= |A\rangle \wedge |B\rangle = \hat{c}_A^\dagger \hat{c}_B^\dagger |0\rangle \\ &= -|B\rangle \wedge |A\rangle = -\hat{c}_B^\dagger \hat{c}_A^\dagger |0\rangle , \end{aligned} \tag{41}$$

where $\hat{c}_\lambda$ (resp. $\hat{c}_\lambda^\dagger$) is the fermionic annihilation (resp. creation) operator in the channel λ. Similarly, as $|A\rangle \wedge |B\rangle = -|B\rangle \wedge |A\rangle$, the exterior product's anti-commutativity directly gives the fermionic anti-commutation relation $\{\hat{c}_A^\dagger, \hat{c}_B^\dagger\} = 0$. The correct way to describe fermionic states in first quantization is then to do it with the exterior product instead of the tensor product.

Moreover, we see that this mathematical definition perfectly encapsulates Pauli's exclusion principle, as any state $|\Psi\rangle$ with two particles in a same quantum state is equal to 0, translating its physical impossibility:

$$|\Psi\rangle = |A\rangle \wedge |A\rangle = -|A\rangle \wedge |A\rangle = -|\Psi\rangle \implies |\Psi\rangle = 0. \tag{42}$$

Speaking of Pauli's exclusion particle, it is primordial to mention another of its numerous implications regarding multi-mode fermionic states: the super-selection rule.

Super-selection rule

Another specificity of fermions is that they obey to a super-selection rule, restricting the space of the physically authorized states. This rule states that, even though they are mathematically legitimate, any superposition of fermionic states with different parities is physically forbidden. This rule, that we won't demonstrate here, directly results from Einstein's special relativity. Indeed, we can prove that, if they existed, such states would allow the communication of information at a speed superior to the speed of light. Formally, we can write that the Hilbert space $\mathcal{H}^{(N)}$ of the physically possible N-modes states is the direct sum of $\mathcal{H}_e^{(N)}$ the space of the even-fermion-number superpositions and $\mathcal{H}_o^{(N)}$ the odd-fermion-number superpositions:

$$\mathcal{H}^{(N)} = \mathcal{H}_e^{(N)} \oplus \mathcal{H}_o^{(N)}. \tag{43}$$

To be a little more concrete, let's take examples in the case of two fermionic modes in the second quantization formalism. The state $|\psi_1\rangle = \frac{1}{\sqrt{2}}(|01\rangle + |11\rangle)$ is forbidden by the super-selection rule, as it is a superposition of a state with an odd number of fermions ($|01\rangle$, 1 fermion) and another state with an even number of fermions ($|11\rangle$, 2 fermions). However, the states $|\psi_2\rangle = \frac{1}{\sqrt{2}}(|00\rangle + |11\rangle)$ and $|\psi_3\rangle = \frac{1}{\sqrt{2}}(|10\rangle - |01\rangle)$ are both physical states authorized by the super-selection rule, as $|\psi_2\rangle$ is a superposition of two even-number-of-fermions states (0 and 2), and $|\psi_3\rangle$ is a superposition of two odd-number-of-fermions states (1 and 1).

With this rule, we see that Pauli's exclusion principle acts in a sense as a restriction on quantum physics' most important principle: the principle of superposition. Indeed, contrary to bosons, it is not possible to physically build any superposition of fermionic states.

Fermionic entangled states

Last but not least, let's give some precisions about the notion of entanglement with indistinguishable particles. Let's consider a two-mode state $|\Psi_{AB}\rangle$ composed of two fermions A and B, which are in the respective states $|\psi_A\rangle \in \mathcal{H}_A$ and $|\psi_B\rangle \in \mathcal{H}_B$. As briefly mentioned in the first section of this document, this two-fermion state is said to be *separable* if it can be written as the exterior product of the state of the fermion A with the state of the fermion B: $|\Psi^{sep}_{AB}\rangle = |\Psi_A\rangle \wedge |\Psi_B\rangle$. In terms of correlation functions, the definition writes for two operators $\hat{A}$ (acting on $\mathcal{H}_A$) and $\hat{B}$ (acting on $\mathcal{H}_B$):

$$\langle\Psi^{sep}_{AB}|\,\hat{A}\wedge\hat{B}\,|\Psi^{sep}_{AB}\rangle = \langle\Psi^{sep}_{AB}|\,\hat{A}\wedge\mathbb{1}_B\,|\Psi^{sep}_{AB}\rangle\,\langle\Psi^{sep}_{AB}|\,\mathbb{1}_A\wedge\hat{B}\,|\Psi^{sep}_{AB}\rangle\,, \tag{44}$$

where $\mathbb{1}_\lambda$ is the identity operator acting on $\mathcal{H}_\lambda$. On the contrary, a state is said to be *entangled* if such a decomposition - whether it be in terms of states or in operators - is not possible. However, this definition only holds for distinguishable particles as we need to know which state belongs to which fermion: this creates a tension between the notions of indistinguishability and separability. The problem in our situation is that we work with pairs of indistinguishable particles. To overcome this difficulty, we need an other definition of entanglement for pairs of indistinguishable particles.

For that matter, we reason in the second quantization formalism and we consider the mode partitioning perspective. Indeed, let's consider M modes $\{c_i\}_{i=1}^M$. We call a *bipartition of modes* two subsets $\mathbb{A} = \{\hat{c}_{A,i}, \hat{c}^\dagger_{A,i}\}_{i=1}^m$ and $\mathbb{B} = \{\hat{c}_{B,j}, \hat{c}^\dagger_{B,j}\}_{j=m+1}^M$, with $m \in \{1, ...M\}$. The operators generated by $\mathbb{A}$ and $\mathbb{B}$ define sets that we respectively call $\mathcal{A}_A$ and $\mathcal{A}_B$. Then, we define a *separable* state $|\Psi^{sep}\rangle$ as a state that can be written in the following way:

$$|\Psi^{sep}\rangle = P\big(\hat{c}^\dagger_{A,1}, ..., \hat{c}^\dagger_{A,m}\big)\,Q\big(\hat{c}^\dagger_{B,m+1}, ..., \hat{c}^\dagger_{B,M}\big)\,|0\rangle\,, \tag{45}$$

where $P \in \mathcal{A}_A$ and $Q \in \mathcal{A}_B$ are polynomials of creation operators, and $|0\rangle$ is the M-mode vacuum. All the other states are then called *entangled*.

Let's finally give some examples of separable and entangled states according to this definition. For example, the states $|\psi_1\rangle = |0_A 0_B\rangle$ ($P = 0$ and $Q = 0$) and $|\psi_2\rangle = |1_A 1_B\rangle = \hat{c}^\dagger_A \hat{c}^\dagger_B\,|0_A 0_B\rangle$ ($P = \hat{c}^\dagger_A$ and $Q = \hat{c}^\dagger_B$) are obviously separable. Similarly, $|\psi_3\rangle = \big(|0_{A,1}1_{A,2}1_{A,3}\rangle + |1_{A,1}1_{A,2}0_{A,3}\rangle\big)\,|1_{B,1}1_{B,2}\rangle$ is also separable, with $P = \hat{c}^\dagger_{A,2}\hat{c}^\dagger_{A,3} + \hat{c}^\dagger_{A,1}\hat{c}^\dagger_{A,2}$ and $Q = \hat{c}^\dagger_{B,1}\hat{c}^\dagger_{B,2}$. By the way, we notice that $|\psi_3\rangle$ indeed respects the super-selection rule, as P creates a superposition of two two-fermion states. Finally, $|\psi_4\rangle = |1_A 1_B\rangle + |0_A 0_B\rangle = \big(\hat{c}^\dagger_A \hat{c}^\dagger_B + \mathbb{1}_A \mathbb{1}_B\big)\,|0_A 0_B\rangle$ is entangled, as it cannot be written as the product of two polynomials P and Q respectively acting on $\mathcal{H}_A$ and $\mathcal{H}_B$.

Here, we directly gave the good definition of entanglement for indistinguishable particles, as this point is not central in the work done during the internship. In order to have more details on the motivations and the reasoning behind this definition, the interested reader can refer to [3]. Let's now study different entanglement criteria that could help to determine whether specific two-fermion states are entangled or not.

4.2.2 Cauchy-Schwarz inequalities as quantum entanglement tests

A large variety of entanglement criteria have been studied since the 1970's, following Clauser, Zeilinger, and Aspect's experiments. The most popular of such criteria are probably those derived from the famous Bell inequality [2]. However, another well-known mathematical inequality happens to provide, when applied to the quantum fields theory's formalism, some very interesting results concerning quantum entanglement: the Cauchy-Schwarz (C.S.) inequality.

In its most general (and mathematical) form, the C.S. inequality gives an upper-bound on the value of the scalar product between two vectors **u** and **v**:

$$|\langle \mathbf{u}, \mathbf{v} \rangle|^2 \leq \langle \mathbf{u}, \mathbf{u} \rangle \, \langle \mathbf{v}, \mathbf{v} \rangle, \tag{46}$$

where the notation $\langle \cdot, \cdot \rangle$ refers to the scalar product. Using the scalar product $\langle \hat{A}, \hat{B} \rangle := \langle \hat{A}^\dagger \hat{B} \rangle_{\hat{\rho}} = Tr(\hat{\rho}\, \hat{A}^\dagger \hat{B})$ on operators, this result can be transposed to the formalism of quantum fields theory. It then take the following form:

$$|\langle \hat{A}_1 \hat{A}_2 \hat{B}_1 \hat{B}_2 \rangle_{\hat{\rho}}|^2 \leq \langle \hat{A}_1 \hat{A}_1^\dagger \hat{B}_1 \hat{B}_1^\dagger \rangle_{\hat{\rho}} \, \langle \hat{A}_2^\dagger \hat{A}_2 \hat{B}_2^\dagger \hat{B}_2 \rangle_{\hat{\rho}}. \tag{47}$$

In equation (47), $\{\hat{A}_1, \hat{A}_2, \hat{B}_1, \hat{B}_2\}$ are four operators, the notation $\cdot^\dagger$ stands for the hermitian conjugate, and $\langle \cdot \rangle_{\hat{\rho}}$ is the quantum expectation value over a quantum state described by the density operator $\hat{\rho}$. During this internship, we worked on three entanglement criteria derived from equation (47).

Before continuing any further, it is crucial to insist on the nuance between the C.S. inequality and the entanglement criteria that can be derived from it. Indeed, as the C.S. inequality is a general mathematical result, it is true for *any* physical state and cannot be violated. On the other hand, entanglement criteria are precisely derived to be violated only by entangled quantum states, and verified by any separable state. However, a quantum state verifying an entanglement criterion does not necessarily mean that it is separable: only entangled states can violate an entanglement criterion, but some entangled states verify it.

The first of the three entanglement criteria considered in this section is the most general. It is derived in [29] and reads:

$$|\langle \hat{A}_1 \hat{A}_2 \hat{B}_1 \hat{B}_2 \rangle_{\hat{\rho}}|^2 \leq \langle \hat{A}_1 \hat{A}_1^\dagger \hat{B}_2^\dagger \hat{B}_2 \rangle_{\hat{\rho}} \langle \hat{A}_2^\dagger \hat{A}_2 \hat{B}_1 \hat{B}_1^\dagger \rangle_{\hat{\rho}}. \tag{48}$$

In the following, equation (48) will be referred to as *criterion 1*, or *full-*$\mathcal{G}^{(2e)}$ *criterion* for reasons we will explain a bit further. The two other criteria are basically special cases of criterion 1, and are known in the literature as *Hillery-Zubairy* criteria [18]. One of them treats the case where $\hat{A}_2 = \hat{B}_1 = \mathbb{1}$, $\hat{A}_1 = \hat{A}^\dagger$, and $\hat{B}_2 = \hat{B}$. Namely, it writes:

$$|\langle \hat{A}^\dagger \hat{B} \rangle_{\hat{\rho}}|^2 \leq \langle \hat{A}^\dagger \hat{A} \hat{B}^\dagger \hat{B} \rangle_{\hat{\rho}}. \tag{49}$$

This criterion will be referred to as *criterion 2*, or *hybrid criterion*. Finally, the third criterion corresponds to the special case $\hat{A}_1 = \hat{B}_1 = \mathbb{1}$, and reads as follows:

$$|\langle \hat{A} \hat{B} \rangle_{\hat{\rho}}|^2 \leq \langle \hat{A}^\dagger \hat{A} \rangle_{\hat{\rho}} \langle \hat{B}^\dagger \hat{B} \rangle_{\hat{\rho}}. \tag{50}$$

We will call this expression *criterion 3*, or *full-*$\mathcal{G}^{(e)}$ *criterion*. This alternative denomination in terms of $\mathcal{G}$ functions comes from the form of these three criteria when we try to express them as inequalities on coherence functions. Indeed, let's now focus on the case of an electronic flying qubit. We saw in section 1 that such a qubit is composed of two channels - let's call them A and B - in which electronic excitations can propagate. It seems then appropriate to define the electronic field operator $\hat{\psi}_\alpha^{(\dagger)}[\varphi]$ annihilating (or creating) in the channel α an electronic excitation described by the wave-function φ. Then, if we replace the generic operators $\{\hat{A}_1, \hat{A}_2, \hat{B}_1, \hat{B}_2\}$ with $\{\hat{\psi}_A^\dagger[\varphi_A], \hat{\psi}_A[\varphi'_A], \hat{\psi}_B^\dagger[\varphi_B], \hat{\psi}_B[\varphi'_B]\}$ in criterion 1 (equation (48)), we obtain:

$$\begin{aligned} &|\langle \hat{\psi}_A^\dagger[\varphi_A]\, \hat{\psi}_A[\varphi'_A]\, \hat{\psi}_B^\dagger[\varphi_B]\, \hat{\psi}_B[\varphi'_B] \rangle_{\hat{\rho}}|^2 \\ &\qquad \leq \langle \hat{\psi}_A^\dagger[\varphi_A]\, \hat{\psi}_A[\varphi_A]\, \hat{\psi}_B^\dagger[\varphi'_B]\, \hat{\psi}_B[\varphi'_B] \rangle_{\hat{\rho}} \, \langle \hat{\psi}_A^\dagger[\varphi'_A]\, \hat{\psi}_A[\varphi'_A]\, \hat{\psi}_B^\dagger[\varphi_B]\, \hat{\psi}_B[\varphi_B] \rangle_{\hat{\rho}} \end{aligned} \tag{51}$$

We recognize the definition of the $\mathcal{G}^{(2e)}$-function, and it is then possible to write criterion 1 as follows:

$$|\mathcal{G}_{\hat{\rho}}^{(2e)}(\varphi_A,\varphi_B\,|\,\varphi'_A,\varphi'_B)|^2 \leq \mathcal{G}_{\hat{\rho}}^{(2e)}(\varphi_A,\varphi'_B\,|\,\varphi_A,\varphi'_B)\mathcal{G}_{\hat{\rho}}^{(2e)}(\varphi'_A,\varphi_B\,|\,\varphi'_A,\varphi_B). \tag{52}$$

This expression justifies why equation (48) will be referred to as *full-$\mathcal{G}^{(2e)}$ criterion*, as it only involves the second-order coherence function in its expression. By replacing the generic operators with the appropriate field operators in the two other criteria, it is easy to show that equations (49) and (50) respectively become:

$$\begin{cases} |\mathcal{G}^{(e)}(\varphi_A,\varphi_B)|^2 \leq \mathcal{G}^{(2e)}(\varphi_A,\varphi_B\,|\,\varphi_A,\varphi_B) \\ |\mathcal{G}^{(e)}(\varphi_A,\varphi_B)|^2 \leq \big(1-\mathcal{G}^{(e)}(\varphi_A|\varphi_A)\big)\mathcal{G}^{(e)}(\varphi_B|\varphi_B) \end{cases} \tag{53}$$

hence the denominations "*hybrid criterion*" and "*full-$\mathcal{G}^{(e)}$ criterion*". In order to better visualize, for each of these three criteria, which quantum states are considered as separable or entangled - meaning which states respect the inequalities and which don't -, it would be useful to use another representation based on spin-operators. This is the purpose of next subsection.

4.2.3 Spin-operator representation

In this subsection, we will use the fact that any quantum state can be represented by a point in what is called *the Bloch sphere*. This representation is very commonly used in quantum information in order to represent the quantum states (meaning the qubits) and the rotations (meaning the operations) we can perform on them.

In order to completely describe a state, we need to know its coordinates along each of the three axis (Ox, Oy, and Oz) of the sphere. We thus need to build a set of three operators $\{\hat{\sigma}^x,\hat{\sigma}^y,\hat{\sigma}^z\}$ which, when applied to a quantum state, give its coordinate along the corresponding axis. Of course, we recognized here an analog of the widely used Pauli spin-operators, which give the spin-value of a quantum state along a given axis. These operators must respect the Pauli algebra, given by the following relation:

$$[\hat{\sigma}^\alpha,\hat{\sigma}^\beta] = 2i\varepsilon_{\alpha\beta\gamma}\hat{\sigma}^\gamma. \tag{54}$$

In equation (54), the notation $[\cdot,\cdot]$ stands for the commutator between two operators, and ε is the totally anti-symmetric Levi-Civita tensor. The aim is then to find three operators permitting to rewrite the previously presented criteria, and respecting equation (54).

Citeria 2 and 3

After some relatively easy but cumbersome calculations, we can show that the following operators fulfill these conditions for criteria 2 and 3 (criterion 1 will be treated separately afterwards):

$$\begin{cases} \hat{\sigma}^x = \hat{\psi}_A^\dagger[\varphi]\,\hat{\psi}_B[\varphi'] + \hat{\psi}_B^\dagger[\varphi']\,\hat{\psi}_A[\varphi] \\ \hat{\sigma}^y = i\big(\hat{\psi}_B^\dagger[\varphi']\,\hat{\psi}_A[\varphi] - \hat{\psi}_A^\dagger[\varphi]\,\hat{\psi}_B[\varphi']\big) \\ \hat{\sigma}^z = \hat{\psi}_A^\dagger[\varphi]\,\hat{\psi}_A[\varphi] - \hat{\psi}_B^\dagger[\varphi']\,\hat{\psi}_B[\varphi'] \end{cases} \tag{55}$$

It is easy to show that these operators are hermitian, meaning they indeed represent a physical observable. From this set of operators, we define auxiliary operators that will help us to rewrite criteria 2 and 3:

$$\begin{cases} \hat{\sigma}^+ = \frac{1}{2}(\hat{\sigma}^x + i\hat{\sigma}^y) = \hat{\psi}_A^\dagger[\varphi]\,\hat{\psi}_B[\varphi'] \\ \hat{\sigma}^- = \frac{1}{2}(\hat{\sigma}^x - i\hat{\sigma}^y) = \hat{\psi}_B^\dagger[\varphi']\,\hat{\psi}_A[\varphi] \\ \mathbb{1}^\sigma = \hat{\psi}_A^\dagger[\varphi]\,\hat{\psi}_A[\varphi] + \hat{\psi}_B^\dagger[\varphi']\,\hat{\psi}_B[\varphi'] \end{cases} \tag{56}$$

Finally, we define the number operator for channel α by $\hat{N}_\alpha[\varphi] = \hat{\psi}^\dagger_\alpha[\varphi]\,\hat{\psi}_\alpha[\varphi]$. This operator basically gives the number of excitations described by the wave-function φ in channel α. Then, we immediately have the relation $\hat{N}_{A/B}[\varphi] = \frac{1}{2}(\mathbb{1}^\sigma \pm \hat{\sigma}^z)$. Using these operators, it is now easy to express equation (49):

$$\begin{aligned} |\langle\hat{\sigma}^+\rangle_{\hat{\rho}}|^2 &\leq \left\langle \frac{1}{2}(\mathbb{1}^\sigma + \hat{\sigma}^z)\frac{1}{2}(\mathbb{1}^\sigma - \hat{\sigma}^z)\right\rangle_{\hat{\rho}} \\ &\leq \frac{1}{4}\big(1 - \langle(\hat{\sigma}^z)^2\rangle_{\hat{\rho}}\big) \end{aligned} \tag{57}$$

However, as $\hat{\sigma}^z$ is a fermionic operator, we have $(\hat{\sigma}^z)^2 = \mathbb{1}^\sigma$. This means that we necessarily have $\langle(\hat{\sigma}^z)^2\rangle_{\hat{\rho}} = 1$. Consequently, the hybrid criterion expressed in terms of spin-operators simply writes:

$$|\langle\hat{\sigma}^+\rangle_{\hat{\rho}}|^2 \leq 0 \tag{58}$$

As the left-hand member of equation (58) is always positive, the criterion is only respected for the states such that $\langle\hat{\sigma}^+\rangle_{\hat{\rho}} = 0$. Besides, it is possible to show that the quantity $2\langle\hat{\sigma}^+\rangle_{\hat{\rho}}$ corresponds to the distance between the origin of the Bloch sphere and the projection of the state on the xOy plane. This means that only two states are separable according to this criterion. The visual representation given in figure 15 shows that these are the states, represented by a red dot, for which $\langle\hat{\sigma}^z\rangle_{\hat{\rho}} = \pm 1$.

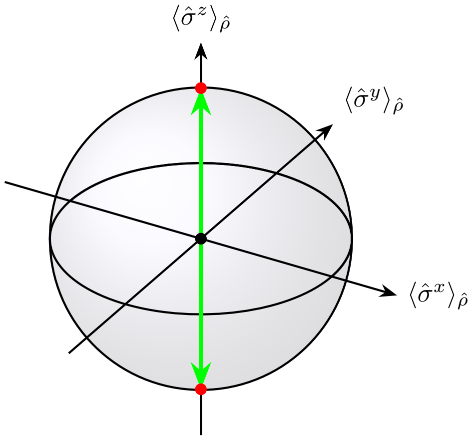

Figure 15: Visual representation of the hybrid criterion on the Bloch sphere. The green states are those who respect the criterion, and all the others violate it. We see that this criterion is very strong: only 2 states respect it, those aligned along $\langle\hat{\sigma}^z\rangle_{\hat{\rho}}$. These two states correspond to the only states for which $\langle\hat{\sigma}^\pm\rangle_{\hat{\rho}} = 0$, meaning that their projection on the $(\langle\hat{\sigma}^x\rangle_{\hat{\rho}}, \langle\hat{\sigma}^y\rangle_{\hat{\rho}})$ plane is the null vector.

With the same operators (55), we can also express the full-$\mathcal{G}^{(e)}$ criterion. Equation (50) then reads:

$$\begin{aligned} |\langle\hat{\sigma}^+\rangle_{\hat{\rho}}|^2 &\leq \left(1 - \frac{1}{2}\langle\mathbb{1}^\sigma + \hat{\sigma}^z\rangle_{\hat{\rho}}\right)\frac{1}{2}\langle\mathbb{1}^\sigma - \hat{\sigma}^z\rangle_{\hat{\rho}} \\ &\leq \frac{1}{4}\big(1 - \langle\hat{\sigma}^z\rangle_{\hat{\rho}}\big)^2 \end{aligned} \tag{59}$$

We can notice that each side of the previous equation is actually the square of a positive quantity (because $-1 \leq \langle\hat{\sigma}^z\rangle_{\hat{\rho}} \leq 1$). This means that the full-$\mathcal{G}^{(e)}$ criterion can finally be written:

$$2|\langle\hat{\sigma}^+\rangle_{\hat{\rho}}| \leq 1 - \langle\hat{\sigma}^z\rangle_{\hat{\rho}} \tag{60}$$

Equation (60) tells that the study can be continued in the plane formed by the axis representing $\langle \hat{\sigma}^z \rangle_{\hat{\rho}}$ and $2\langle \hat{\sigma}^+ \rangle_{\hat{\rho}}$. From here, it is easy to show that this expression is equivalent to the following cartesian equation in the (x, y) plane:

$$x^2 - y^2 + 2y - 1 \leq 0 \tag{61}$$

Geometrically, equation (61) corresponds to the green area in figure 16. Therefore, the full-$\mathcal{G}^{(e)}$ criterion considers as separable all the states located in this volume of the Bloch sphere, and as entangled all the states outside of it.

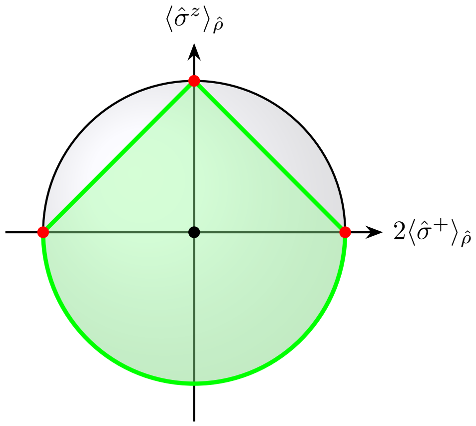

Figure 16: Visual representation of the full-$\mathcal{G}^{(e)}$ criterion in the $\big(2\langle \hat{\sigma}^+ \rangle_{\hat{\rho}}, \langle \hat{\sigma}^z \rangle_{\hat{\rho}}\big)$ plane. The green area corresponds to the separable states, while the grey area represent the entangled states that don't respect the criterion. Being respected by more states than previously, this criterion is less strong than the hybrid one. However, it is still useful as some states violate it.

The asymmetry of figure 16's green area is simply a consequence of the operators to which we applied the criterion. Indeed, while the criterion is symmetrical, applying it to a particular set of operators breaks the symmetry. For example, had we taken $(\hat{A}, \hat{B}) = \big(\hat{\psi}_B^\dagger[\varphi_B], \hat{\psi}_A[\varphi_A]\big)$ instead of $(\hat{A}, \hat{B}) = \big(\hat{\psi}_A^\dagger[\varphi_A], \hat{\psi}_B[\varphi_B]\big)$ in equation (50), the criterion would have read:

$$2|\langle \hat{\sigma}^- \rangle_{\hat{\rho}}| \leq 1 + \langle \hat{\sigma}^z \rangle_{\hat{\rho}}. \tag{62}$$

In cartesian coordinates, equation (62) then reads $x^2 - y^2 - 2y - 1 \leq 0$, and translates into the visual representation in the $(2\langle \hat{\sigma}^- \rangle_{\hat{\rho}}, \langle \hat{\sigma}^z \rangle_{\hat{\rho}})$ plane given in figure 17.

Criterion 1

To conclude this subsection, let's deal with the spin-operators' expression of the full-$\mathcal{G}^{(2e)}$ criterion. In that last case, the previously defined set of spin operators doesn't allow us to correctly express the criterion, given by equation (48). Indeed, to do so, we need spin operators creating two different excitations on the same channel, which isn't possible with operators (55). To overcome this problem, we need to define spin operators for each channel λ ($\lambda \in \{A, B\}$):

$$\begin{cases} \hat{\sigma}^x_\lambda = \hat{\psi}^\dagger_\lambda[\varphi]\,\hat{\psi}_\lambda[\varphi'] + \hat{\psi}^\dagger_\lambda[\varphi']\,\hat{\psi}_\lambda[\varphi] \\ \hat{\sigma}^y_\lambda = i\big(\hat{\psi}^\dagger_\lambda[\varphi']\,\hat{\psi}_\lambda[\varphi] - \hat{\psi}^\dagger_\lambda[\varphi]\,\hat{\psi}_\lambda[\varphi']\big) \\ \hat{\sigma}^z_\lambda = \hat{\psi}^\dagger_\lambda[\varphi]\,\hat{\psi}_\lambda[\varphi] - \hat{\psi}^\dagger_\lambda[\varphi']\,\hat{\psi}_\lambda[\varphi'] \end{cases} \tag{63}$$

Like for the hybrid and the full-$\mathcal{G}^{(e)}$ criteria, we also define three other channel-dependent operators from these ones:

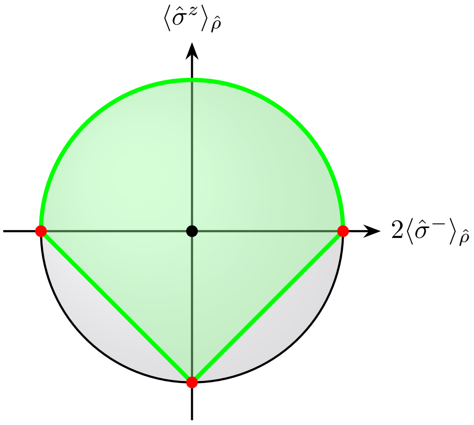

Figure 17: Visual representation of the full-$\mathcal{G}^{(e)}$ criterion in the $\big(2\langle\hat{\sigma}^-\rangle_{\hat{\rho}}, \langle\hat{\sigma}^z\rangle_{\hat{\rho}}\big)$ plane, for a different choice of field operators. The green area corresponds to the separable states, while the grey area represent the entangled states that don't respect the criterion. This example illustrates the fact that even though the criterion is symmetrical, the symmetry is broken by the choice of operators to which we apply it.

$$\begin{cases} \hat{\sigma}^+_\lambda = \frac{1}{2}(\hat{\sigma}^x_\lambda + i\hat{\sigma}^y_\lambda) = \hat{\psi}^\dagger_\lambda[\varphi]\,\hat{\psi}_\lambda[\varphi'] \\ \hat{\sigma}^-_\lambda = \frac{1}{2}(\hat{\sigma}^x_\lambda - i\hat{\sigma}^y_\lambda) = \hat{\psi}^\dagger_\lambda[\varphi']\,\hat{\psi}_\lambda[\varphi] \\ \mathbb{1}^\sigma_\lambda = \hat{\psi}^\dagger_\lambda[\varphi]\hat{\psi}_\lambda[\varphi] + \hat{\psi}^\dagger_\lambda[\varphi']\,\hat{\psi}_\lambda[\varphi'] \end{cases} \tag{64}$$

Defining $\hat{N}_\lambda[\varphi] = \hat{\psi}^\dagger_\lambda[\varphi]\,\hat{\psi}_\lambda[\varphi]$, we can again notice that $\hat{N}_\lambda[\varphi/\varphi'] = \frac{1}{2}(\mathbb{1}^\sigma_\lambda \pm \hat{\sigma}^z_\lambda)$. Hence, equation (48) written in terms of spin operators reads:

$$\begin{aligned} |\langle\hat{\sigma}^+_A\hat{\sigma}^+_B\rangle_{\hat{\rho}}|^2 &\leq \Big\langle\frac{1}{2}(\mathbb{1}_A + \hat{\sigma}^z_A)\frac{1}{2}(\mathbb{1}_B - \hat{\sigma}^z_B)\Big\rangle_{\hat{\rho}}\Big\langle\frac{1}{2}(\mathbb{1}_A - \hat{\sigma}^z_A)\frac{1}{2}(\mathbb{1}_B + \hat{\sigma}^z_B)\Big\rangle_{\hat{\rho}} \\ &\leq \frac{1}{16}\big\langle(\mathbb{1}_A + \hat{\sigma}^z_A)(\mathbb{1}_B - \hat{\sigma}^z_B)\big\rangle_{\hat{\rho}}\big\langle(\mathbb{1}_A - \hat{\sigma}^z_A)(\mathbb{1}_B + \hat{\sigma}^z_B)\big\rangle_{\hat{\rho}}. \end{aligned} \tag{65}$$

We remark that equation (65) for criterion 1 is notably more complex than equations (58) and (60), respectively giving the spin-operators expressions of criteria 2 and 3. Even though this criterion is the most general (and probably the most physically interesting) of the three studied criteria, we did not find any simple geometric interpretation of this equation that would allow us to visualize the states in considers as separable and entangled.

However, we're not going to give up our wish to interpret this criterion geometrically, as next subsection will give an in-depth analysis of criterion 1 in the case of a two-electron coherent scattering model.

4.3 Entanglement in a two-electron scattering model

We want to test entanglement generation by Coulomb interaction for two electrons perfectly localized in energy, and propagating within two quantum Hall edge channels. To emulate a railroad qubit setup, we consider a system composed of two parallel channels (typically two quantum Hall edge channels in a mesoscopic conductor) labelled A and B.

4.3.1 Second-order criterion for two perfectly energy-localized electrons

We will make our study in the frequency domain, and consequently use the electronic operators $\hat{c}_\alpha[\omega]$ (resp. $\hat{c}^\dagger_\alpha[\omega]$) annihilating (resp. the creating) an electron of energy ω in the channel α. As the study relies on two-electron states, we will need the full-$\mathcal{G}^{(2e)}$ criterion. Hence, we choose in equation (48) the four-operators set $\{\hat{c}_A^\dagger[\omega_A], \hat{c}_A[\omega'_A], \hat{c}_B^\dagger[\omega_B], \hat{c}_B[\omega'_B]\}$ to replace $\{\hat{A}_1, \hat{A}_2, \hat{B}_1, \hat{B}_2\}$. Then, it reads:

$$\begin{aligned} &|\langle \hat{c}_A^\dagger[\omega_A]\, \hat{c}_A[\omega'_A]\, \hat{c}_B^\dagger[\omega_B]\, \hat{c}_B[\omega'_B]\rangle_{\hat{\rho}}|^2 \\ &\qquad \leq \langle \hat{c}_A^\dagger[\omega_A]\, \hat{c}_A[\omega_A]\, \hat{c}_B^\dagger[\omega'_B]\, \hat{c}_B[\omega'_B]\,\rangle_{\hat{\rho}}\, \langle \hat{c}_A^\dagger[\omega'_A]\, \hat{c}_A[\omega'_A]\, \hat{c}_B^\dagger[\omega_B]\, \hat{c}_B[\omega_B]\rangle_{\hat{\rho}}. \end{aligned} \tag{66}$$

In order to continue in the frequency space, we will use the frequency representation of the second-order electronic coherence function:

$$\left(\frac{v_F}{2\pi}\right)^2 \widetilde{\mathcal{G}}^{(2e)}_{\hat{\rho}}(\omega'_A, \omega'_B \,|\, \omega_A, \omega_B) = \langle \hat{c}_A^\dagger[\omega_A]\, \hat{c}_B^\dagger[\omega_B]\, \hat{c}_B[\omega'_B]\, \hat{c}_A[\omega'_A]\rangle_{\hat{\rho}}, \tag{67}$$

We now inject equation (67) in (66), and the criterion can be written as an inequality between two products of second-order electronic coherence functions:

$$|\widetilde{\mathcal{G}}^{(2e)}_{\hat{\rho}}(\omega'_A, \omega'_B \,|\, \omega_A, \omega_B)|^2 \leq \widetilde{\mathcal{G}}^{(2e)}_{\hat{\rho}}(\omega_A, \omega'_B \,|\, \omega_A, \omega'_B)\, \widetilde{\mathcal{G}}^{(2e)}_{\hat{\rho}}(\omega'_A, \omega_B \,|\, \omega'_A, \omega_B). \tag{68}$$

Let's now apply criterion (68) to a physical state corresponding to a simple model of two-electron coherent scattering. To begin with, we consider a state $|\psi\rangle_{in}$ composed of two electronic excitations, one in each of the two channels A and B, of respective energies $\hbar\omega_A$ and $\hbar\omega_B$. This situation corresponds to two incoming electronic plane waves, of which the energies are perfectly defined. Writing the Fermi sea of the global system as the exterior product of the Fermi sea of each channel, this state reads:

$$|\psi\rangle_{in} = \hat{c}_A^\dagger[\omega_A]\, \hat{c}_B^\dagger[\omega_B]\; |F\rangle \quad \text{with} \quad |F\rangle := |F\rangle_A \wedge |F\rangle_B\,. \tag{69}$$

The index (A or B) on the right member's kets indicates the channel on which the excitation is created. This two-electron state enters an interaction area and experiences a coherent two-particle scattering above the Fermi sea. This process is described by the two-electron scattering matrix $\hat{S}$ that ensures that the total energy is conserved. An amount $\delta\omega$ of energy is transferred from the electron in channel A to the electron in channel B (see figure 18).

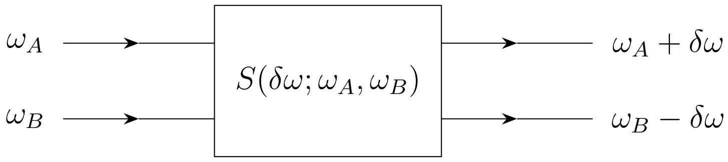

Figure 18: Schema of the two-electron scattering model. Two electrons, with respective energies $\hbar\omega_A$ and $\hbar\omega_B$, enter the interaction area described by the scattering matrix $\hat{S}$, exchange an amount of energy $\delta\omega$, and exit with energies $\hbar(\omega_A + \delta\omega)$ and $\hbar(\omega_B - \delta\omega)$.

Consequently, the output state $|\psi\rangle$ describing the two-electron state is a superposition of all the output states for each $\delta\omega$ value. We can write:

$$|\psi\rangle = \int_{\mathbb{R}} d(\delta\omega)\, S(\delta\omega; \omega_A, \omega_B)\, \hat{c}_A^\dagger[\omega_A + \delta\omega]\, \hat{c}_B^\dagger[\omega_B - \delta\omega]\; |F\rangle\,. \tag{70}$$

The physical interpretation of the $\hat{S}$ matrix is that the squared modulus of the matrix coefficient $S(\delta\omega; \omega_A, \omega_B)$ gives the transition probability between the input state (ω_A, ω_B) and the output state $(\omega_A + \delta\omega, \omega_B - \delta\omega)$. This can be written:

$$|S(\omega; \omega_A, \omega_B)|^2 = \mathbb{P}\big[(\omega_A, \omega_B) \to (\omega_A + \omega, \omega_B - \omega)\big] \tag{71}$$

The objective is now to re-write equation (68) explicitly in the case where $\hat{\rho} = |\psi\rangle\,\langle\psi|$, with $|\psi\rangle$ defined as in equation (70). To begin with, let's express the $\mathcal{G}^{(2e)}$-function with four arbitrary arguments, like in the the left-hand side of (68). For simplicity, the four arguments of $\mathcal{G}_{\hat{\rho}}^{(2e)}$ will be defined with respect to the input energies ω_A and ω_B, and the function reads as follows:

$$\widetilde{\mathcal{G}}_{\hat{\rho}}^{(2e)}(\omega_A + \delta\omega_A^+,\, \omega_B - \delta\omega_B^+ \,|\, \omega_A + \delta\omega_A^-,\, \omega_B - \delta\omega_B^-), \tag{72}$$

where $\{\delta\omega_A^+, \delta\omega_B^+, \delta\omega_A^-, \delta\omega_B^-\}$ are the four "new" variables.

It is important to remark that, as we are only interested in detecting electrons coming from the scattering process, there is only a limited energy bandwidth in which the detection is relevant. Indeed, the second-order coherence function can be formally written:

$$\mathcal{G}_{AB}^{(2e)} = \underbrace{\Delta\mathcal{G}_{AB}^{(2e)}}_{[1]} + \underbrace{\Delta\mathcal{G}_{A}^{(e)}\mathcal{G}_{B,F}^{(e)}}_{[2]} + \underbrace{\mathcal{G}_{A,F}^{(e)}\Delta\mathcal{G}_{B}^{(e)}}_{[3]} + \underbrace{\mathcal{G}_{AB,F}^{(2e)}}_{[4]} \tag{73}$$

In equation (73), the letters A and/or B in indices correspond to the channel(s) in which the coherence is considered, while the letter F refers to the coherence of the Fermi sea in the channel(s), and the symbol $\Delta\cdot$ stands for the intrinsic excess of coherence. This decomposition - that we will explain just after - shows that four contributions corresponding to different phenomena contribute to the second-order coherence.

The incoming electrons enter the scattering process with respective energies $\hbar\omega_A$ and $\hbar\omega_B$, exchange an energy $\delta\omega$, and exit the process with energies $\hbar(\omega_A + \delta\omega)$ and $\hbar(\omega_B - \delta\omega)$. Then, in order for both incoming electrons to be detected above the Fermi sea when they exit the interaction area, the energy $\delta\omega$ exchanged between them must be such as:

$$-\omega_A \leq \delta\omega \leq \omega_B \tag{74}$$

The detailed computation of the $\mathcal{G}^{(2e)}$-function's explicit form in the scattering model is given in appendix A. In order not to drawn in calculations, we only present in this section the result of the full calculation:

$$\begin{aligned}
&\widetilde{\mathcal{G}}_{\hat{\rho}}^{(2e)}(\omega_A + \delta\omega_A^+,\, \omega_B - \delta\omega_B^+ \,|\, \omega_A + \delta\omega_A^-,\, \omega_B - \delta\omega_B^-) \\
&\quad = \left.\begin{array}{l} \delta(\delta\omega_A^- - \delta\omega_B^-)\,\delta(\delta\omega_A^+ - \delta\omega_B^+)\,S(\delta\omega_A^-;\omega_A,\omega_B)^*\,S(\delta\omega_A^+;\omega_A,\omega_B) \\ \Theta(\omega_B - \delta\omega_A^+)\,\Theta(\omega_A + \delta\omega_A^+)\,\Theta(\omega_A + \delta\omega_A^-)\,\Theta(\omega_B - \delta\omega_A^-) \end{array}\right\}[1] \\
&\quad + \left.\begin{array}{l} \delta(\delta\omega_B^- - \delta\omega_B^+)\,\delta(\delta\omega_A^- - \delta\omega_A^+)\,|S(\delta\omega_A^+;\omega_A,\omega_B)|^2 \\ \Theta(\delta\omega_B^+ - \omega_B)\,\Theta(\omega_B - \delta\omega_A)\,\Theta(\omega_A - \delta\omega_A^+) \end{array}\right\}[2] \\
&\quad + \left.\begin{array}{l} \delta(\delta\omega_B^- - \delta\omega_B^+)\,\delta(\delta\omega_A^- - \delta\omega_A^+)\,|S(\delta\omega_B^+;\omega_A,\omega_B)|^2 \\ \Theta(-\delta\omega_A^+ - \omega_A)\,\Theta(\omega_A + \delta\omega_B)\,\Theta(\omega_B - \delta\omega_B^+) \end{array}\right\}[3] \\
&\quad + \ \delta(\delta\omega_B^- - \delta\omega_B^+)\,\delta(\delta\omega_A^- - \delta\omega_A^+)\,\Theta(-\delta\omega_A^+ - \omega_A)\,\Theta(\delta\omega_B^+ - \omega_B)\ \}[4]
\end{aligned} \tag{75}$$

As in equation (73), the terms of equation (75) come from four different physical scenarii, and have different interpretations. Besides, each term of equation (75) corresponds to the term with the same number in equation (73).

Concretely, term [1] physically corresponds to the case where both detected electrons come from the scattering process, hence the notation $\Delta\mathcal{G}_{AB}^{(2e)}$ denoting the second-order intrinsic excess of coherence in equation (73). It is non-zero only if the four variables are such that:

$$\begin{array}{lcl} \delta\omega_A^- = \delta\omega_B^- & \text{and} & -\omega_A \leq \delta\omega_A^- \leq \omega_B \\ \delta\omega_A^+ = \delta\omega_B^+ & \text{and} & -\omega_A \leq \delta\omega_A^+ \leq \omega_B \end{array}$$

Regarding term [2], it represents the case where the electron detected in channel A comes from the scattering process $\left(\Delta\mathcal{G}_{A}^{(e)}\right)$, and the one detected in channel B comes from the Fermi sea $\left(\mathcal{G}_{B,F}^{(e)}\right)$. It gives a non-zero contribution only if:

$$\begin{array}{lcl} \delta\omega_A^- = \delta\omega_A^+ & \text{and} & -\omega_A \leq \delta\omega_A^+ \leq \omega_B \\ \delta\omega_B^- = \delta\omega_B^+ & \text{and} & \omega_B \leq \delta\omega_B^+ \end{array}$$

The contribution of term [3] corresponds to the physical opposite of term [2]. This corresponds to the case where the electron detected in channel A comes from the Fermi sea $\left(\mathcal{G}_{A,F}^{(e)}\right)$, and the one detected in channel B comes from the scattering process $\left(\Delta\mathcal{G}_B^{(e)}\right)$. It is non-zero if and only if:

$$\begin{array}{lcl} \delta\omega_A^- = \delta\omega_A^+ & \text{and} & \delta\omega_A^+ \leq -\omega_A \\ \delta\omega_B^- = \delta\omega_B^+ & \text{and} & -\omega_A \leq \delta\omega_B^+ \leq \omega_B \end{array}$$

Finally, the last term [4] corresponds to the only case that is not encapsulated by the three previous terms: when both detected electrons come the Fermi sea $\left(\mathcal{G}_{AB,F}^{(2e)}\right)$. It is non-null as soon as:

$$\begin{array}{lcl} \delta\omega_A^- = \delta\omega_A^+ & \text{and} & \delta\omega_A^+ \leq -\omega_A \\ \delta\omega_B^- = \delta\omega_B^+ & \text{and} & \omega_B \leq \delta\omega_B^+ \end{array}$$

As mentioned previously, only one of these four terms is really relevant in the case we are interested in. Indeed, as the goal of this work is to study the evolution of the two-electron entanglement after the collision, all the terms corresponding to at least one detected electron coming from the Fermi sea are irrelevant. Hence, we can consider only the case described by term [1]. Let's now give a complete expression of the Cauchy-Schwarz criterion (68) in terms of the $\hat{S}$ matrix.

Expression in terms of $\hat{S}$ matrix coefficients

The rest of the study will then be realized under some constraints regarding the values of $\delta\omega_A^\pm$ and $\delta\omega_B^\pm$, corresponding to those of term [1] in equation (75):

$$\begin{array}{lcl} \delta\omega_A^- = \delta\omega_B^- & \text{and} & -\omega_A \leq \delta\omega_A^- \leq \omega_B \\ \delta\omega_A^+ = \delta\omega_B^+ & \text{and} & -\omega_A \leq \delta\omega_A^+ \leq \omega_B \end{array}$$

In the following, we consider $\delta\omega_A^- = \delta\omega_B^- := \delta\omega^-$, $\delta\omega_A^+ = \delta\omega_B^+ := \delta\omega^+$, and $\delta\omega^- \neq \delta\omega^+$ (otherwise, the criterion simply expresses a trivial equality). Under these assumptions, the $\mathcal{G}^{(2e)}$ function takes a simpler form:

$$\widetilde{\mathcal{G}}_{\hat{\rho}}^{(2e)}(\omega_A + \delta\omega^+, \omega_B - \delta\omega^+ \,|\, \omega_A + \delta\omega^-, \omega_B - \delta\omega^-) = S(\delta\omega^-; \omega_A, \omega_B)^* \, S(\delta\omega^+; \omega_A, \omega_B). \tag{76}$$

In equation (76), we suppressed the two δ and the four Θ functions as they are redundant with the hypothesis on the energies. With these new variables, and under the previous hypothesis on the energies, the criterion writes:

$$\begin{aligned} &|\widetilde{\mathcal{G}}_{\hat{\rho}}^{(2e)}(\omega_A + \delta\omega^+, \omega_B - \delta\omega^+ \,|\, \omega_A + \delta\omega^-, \omega_B - \delta\omega^-)|^2 \\ &\qquad \leq \widetilde{\mathcal{G}}_{\hat{\rho}}^{(2e)}(\omega_A + \delta\omega^-, \omega_B - \delta\omega^+ \,|\, \omega_A + \delta\omega^-, \omega_B - \delta\omega^+) \\ &\qquad\quad \widetilde{\mathcal{G}}_{\hat{\rho}}^{(2e)}(\omega_A + \delta\omega^+, \omega_B - \delta\omega^- \,|\, \omega_A + \delta\omega^+, \omega_B - \delta\omega^-). \end{aligned} \tag{77}$$

First, we consider the first term of the criterion's right-hand member. Given the conditions on $\delta\omega^-$ and $\delta\omega^+$, and using equation (75), we have:

$$\widetilde{\mathcal{G}}_{\hat{\rho}}^{(2e)}(\omega_A + \delta\omega^-, \omega_B - \delta\omega^+ \,|\, \omega_A + \delta\omega^-, \omega_B - \delta\omega^+) = 0. \tag{78}$$

Indeed, the first term in the right-hand side of (75) vanishes because of the δ-functions as $\delta\omega^- \neq \delta\omega^+$. Concerning the other terms, they are all cancelled due to the Θ-functions combinations that are not compatible with the conditions $-\omega_A \leq \delta\omega^- \leq \omega_B$ and $-\omega_A \leq \delta\omega^+ \leq \omega_B$. Additionally, we can notice that for the same reasons, the second term of the criterion's right-hand member is null too. Finally, criterion (77) writes:

$$|S(\delta\omega^-;\omega_A,\omega_B)^* S(\delta\omega^+;\omega_A,\omega_B)|^2 \leq 0. \tag{79}$$

This means that the criterion detects the output state as entangled as soon as $S(\delta\omega^-;\omega_A,\omega_B) \neq 0$ and $S(\delta\omega^+;\omega_A,\omega_B) \neq 0$. Concretely, if the incoming electrons exchange energy, the criterion is automatically violated. Another way to say it is that the scattering process necessarily creates entanglement.

Visualization of the scattering process

In order to better understand the meaning of the entanglement criterion, let's first try to visualize the scattering process associated to our model in the four-dimensional frequency space. We consider the overlap between the two previously considered quantum paths in the scattering area: one along which the two initial electrons of energies (ω_A, ω_B) exchange a quantity $\delta\omega^+$ of energy, and the other one along which they exchange a quantity $\delta\omega^-$. This corresponds to the number $\widetilde{\mathcal{G}}^{(2e)}(\omega_A+\delta\omega^+, \omega_B-\delta\omega^+ \,|\, \omega_A+\delta\omega^-, \omega_B-\delta\omega-)$, which is exactly the left-hand side member of equation (77). In the following, we will preferentially use the following variables:

$$\begin{cases} \overline{\omega} = \frac{\delta\omega^+ + \delta\omega-}{2} \\ \Delta\omega = \delta\omega^+ - \delta\omega^- \end{cases} \tag{80}$$

In equation (80), $\overline{\omega}$ and $\Delta\omega$ respectively correspond to the average exchanged-energy and the difference between the two energies exchanged along both paths. We can then express the "old" variables as $\delta\omega^\pm = \overline{\omega} \pm \frac{\Delta\omega}{2}$.

In the four-dimensional energy space, a quantum state is represented by a 4D-point, which can be decomposed into what we call a *diagonal* and an *off-diagonal* parts. The diagonal contribution represents the "classical side" of the point, meaning the energy of each of the two electrons constituting the state. It is obtained by computing the average of each argument over the two quantum paths. Concerning the off-diagonal part, it corresponds to the coherence between the two electrons in the state, and is associated to the "quantum side" of the state. It is calculated by taking, for each argument, the difference between both quantum paths. A schema of the situation, representing the states considered here, is given in figure 19. For the initial and final states, two pairs of coordinates are represented: the top one corresponds to the diagonal part, while the bottom one refers to the off-diagonal contribution.

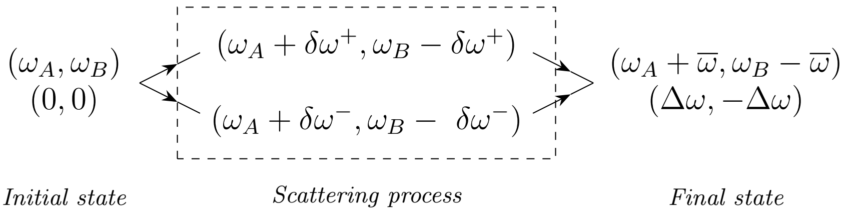

Figure 19: Schema of the two quantum paths considered in the $\mathcal{G}^{(2e)}$ function. The two-electron initial state of classical component (ω_A, ω_B) and off-diagonal part $(0, 0)$ scatters in two different ways: one with an exchanged energy $\delta\omega^+$ in the scattering area, and the other with an exchanged energy $\delta\omega^-$. This gives a final state with a classical component $(\omega_A + \overline{\omega}, \omega_B - \overline{\omega})$ and an off-diagonal contribution $(\Delta\omega, -\Delta\omega)$.

After the collision, the diagonal part of the final state is $(\omega'_A, \omega'_B) := (\omega_A + \overline{\omega}, \omega_B - \overline{\omega})$, and its off-diagonal part is $(\Omega'_A, \Omega'_B) := (\Delta\omega, -\Delta\omega)$. For the initial state, it is $(0, 0)$ by definition as it is perfectly localized in energy.

We can then give a graphical representation of a state's evolution by identifying each point of the four-dimensional space as a point in the two-dimensional *diagonal* plane and another point in the two-dimensional *off-diagonal* plane. The graphs in figure 20 represent the state studied in this paragraph before and after it scattered.

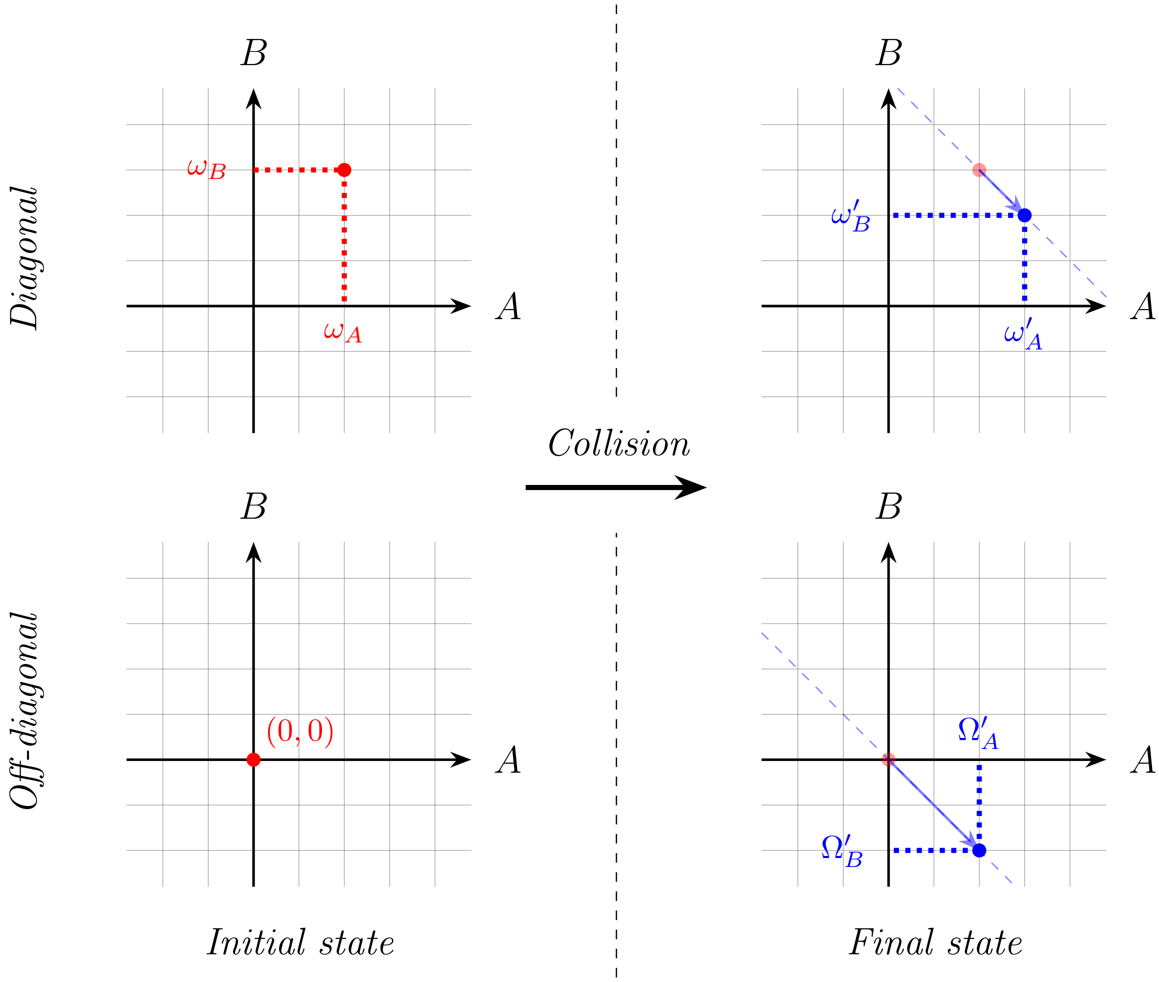

Figure 20: Localization of the two-electron state before and after scattering. The initial state corresponds to the two left-hand side graphs, while the scattered state is described by the two graphs on the right. For each state, the top-graph represents the coherence's diagonal part ("classical component") and the bottom-graph stands for the off-diagonal part ("quantum component"). During the collision, both diagonal and off-diagonal contributions are displaced along the 3D-hyperplane conserving the total energy, and represented by the line of slope -1 that crosses the initial state's point.

We notice that the collision "moved" the 4D point representing the initial state along the three-dimensional hyperplane represented by the line of slope -1 (in dashed blue in figure 20), whether it be in the diagonal or the off-diagonal plane. This is due to the conservation of energy: the amount of energy gained (resp. lost) by the electron in channel A is necessary lost (resp. gained) by the one in channel B.

To have a better intuition regarding the scattering process, let's study the coupling existing between the difference of the contributions from both channels (A and B) in the diagonal and in the off-diagonal planes. Indeed, the coordinates of the scattered state in figures 19 and 20 lead to the conclusion that the sum of the two diagonal coordinates and that of the two off-diagonal coordinates remain unchanged by the scattering process. This is a consequence of the energy conservation when the electrons are scattered. The idea is then to study the differences between the two diagonal and off-diagonal coordinates to visualize (in a 2D plane) the position of the scattered state compared to the initial state. To be clearer, let's first introduce several notations. In the following:

- ω_A (resp. ω_B) represents the diagonal contribution of the electron in channel A (resp. B);
- Ω_A (resp. Ω_B) represents the off-diagonal contribution of the electron in channel A (resp. B).

The goal of this paragraph is then to study the relations between the quantities $\delta\omega := \omega_A - \omega_B$ and $\delta\Omega := \Omega_A - \Omega_B$. Like before, we consider here the initial state (ω_A, ω_B). After the collision, the diagonal contributions become $(\omega_A + \overline{\omega}, \omega_B - \overline{\omega})$, giving $\delta\omega = \omega_A - \omega_B + 2\overline{\omega} = \omega_A - \omega_B + \delta\omega^+ + \delta\omega^-$. As the off-diagonal contributions become $(\Delta\omega, -\Delta\omega)$, the same calculation gives $\delta\Omega = 2\Delta\omega = 2(\delta\omega^+ - \delta\omega^-)$. Then, the initial state with the 4D-coordinates $\big((\omega_A, \omega_B), (0,0)\big)$ in the diagonal and off-diagonal planes has the coordinates $(\omega_A - \omega_B, 0)$ in the $(\delta\omega, \delta\Omega)$ plane (see the red point in figure 21). Following the same reasoning, the scattered state with the coordinates $\big((\omega_A + \overline{\omega}, \omega_B - \overline{\omega}), (\Delta\omega, -\Delta\omega)\big)$ in the 4D-space is represented by the 2D-point of coordinates $(\omega_A - \omega_B + 2\overline{\omega}, 2\Delta\omega)$ in the $(\delta\omega, \delta\Omega)$ plane.

Now, let's make the hypothesis that $|\delta\omega^+|$ and $|\delta\omega^-|$ are upper-bounded, say by a maximal value $\delta\omega_{max}$. This hypothesis make sense physically, as there always exist a value of $\delta\omega^\pm$ for which $\omega_A - |\delta\omega^\pm|$ or $\omega_B - |\delta\omega^\pm|$ becomes smaller than the Fermi level, and then doesn't respect the conditions set before. After the collision, we can then write:

$$\begin{gathered} \omega_A - \omega_B - 2\delta\omega_{max} \leq \delta\omega \leq \omega_A - \omega_B + 2\delta\omega_{max} \\ -4\delta\omega_{max} \leq \delta\Omega \leq 4\delta\omega_{max} \end{gathered} \tag{81}$$

We can notice that the extreme values of $\delta\omega$ ($\delta\omega = \omega_A - \omega_B \pm 2\delta\omega_{max}$) imply that $\delta\omega^+ = \delta\omega^- = \pm\delta\omega_{max}$. As a consequence, we necessarily have $\delta\Omega = 0$ in this case as $\delta\Omega = 2(\delta\omega^+ - \delta\omega^-)$. Reciprocally, the extreme values of $\delta\Omega$ ($\delta\Omega = \pm 4\delta\omega_{max}$) imply that $\delta\omega^+ = -\delta\omega^- = \pm\delta\omega_{max}$. In that case, we then have $\delta\omega = \omega_A - \omega_B + \delta\omega^+ + \delta\omega^- = \omega_A - \omega_B$. These four cases, the two extremal values of $\delta\omega$ and those of $\delta\Omega$, correspond to the four blue points in figure 21.

Then, we deduce from the inequalities (81) that the possible values taken by the couple of variables $(\delta\omega, \delta\Omega)$ lie inside the diamond delimitated by the extremal cases (see the blue area in figure 21). Indeed, as explained before, the conservation of the total energy implies that both variables $\delta\omega$ and $\delta\Omega$ are not independent: the bigger $\delta\omega$, the smaller the interval in which $\delta\Omega$ can take values (and reciprocally). This appears naturally if we look at the expression of these two variables as functions of ω_+ and ω_-. The physical interpretation of the blue diamond represented in figure 21 is that, under the considered hypothesis, the final state scattered from an initial two-electron state of 4D-coordinates $\big((\omega_A, \omega_B), (0,0)\big)$ is necessarily located in the diamond centered in $(\omega_A - \omega_B, 0)$, of height $8\delta\omega_{max}$, and of width $4\delta\omega_{max}$ in the $(\delta\omega, \delta\Omega)$ plane. This means that for a given value of the diagonal contribution $\delta\omega$, the off-diagonal part $\delta\Omega$ is located in an interval centered in 0 and which length decreases when $\delta\omega$ deviate from $\omega_A - \omega_B$). Reciprocally, a fixed value of $\delta\Omega$ implies a diagonal part $\delta\omega$ lying in an interval centered in $\omega_A - \omega_B$ and which length decreases as $\delta\Omega$ deviates from 0.

A less physical, but maybe easier way to understand the diamond shape in the $(\delta\omega, \delta\Omega)$ plane is the following. The condition $|\delta\omega^\pm| \leq \delta\omega_{max}$ describes in the $(\delta\omega^+, \delta\omega^-)$ plane a square centered on the initial state, and of side $4\delta\omega_{max}$. However, the rotation and the rescaling done by switching to the two variables $(\overline{\omega}, \Delta\omega)$ transforms this square into a diamond of width $4\delta\omega_{max}$ and of height $8\delta\omega_{max}$.

Four-dimensional visualisation

Now that we know how to represent the scattered state on which we define our study, let's focus on the right-hand side of criterion (77). We then need to study the points $\widetilde{\mathcal{G}}^{(2e)}_{\hat{\rho}}(\omega_A + \delta\omega^+, \omega_B - \delta\omega^- \,|\, \omega_A + \delta\omega^+, \omega_B - \delta\omega -)$ and $\widetilde{\mathcal{G}}^{(2e)}_{\hat{\rho}}(\omega_A + \delta\omega^-, \omega_B - \delta\omega^+ \,|\, \omega_A + \delta\omega^-, \omega_B - \delta\omega^+)$. These quantities are both diagonal,

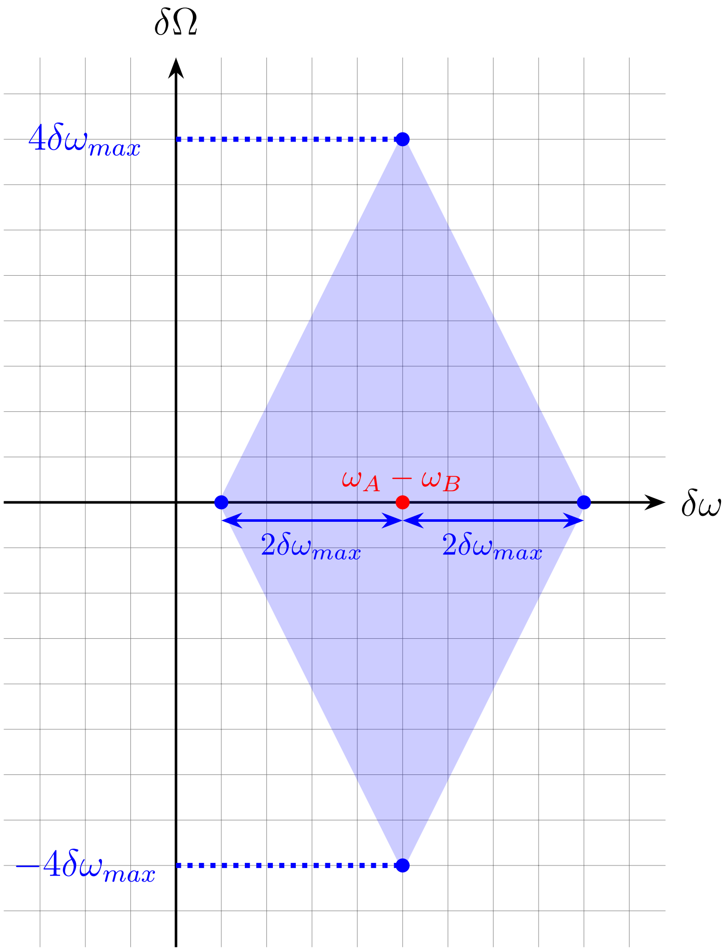

Figure 21: Geometrical interpretation of the Cauchy-Schwarz criterion in the $(\delta\omega, \delta\Omega)$ plane. The x-axis represents the coherence's diagonal part and the y-axis the off-diagonal part. The red point corresponds to the initial state, and the blue diamond the area in which this state can be moved by the scattering process.

hence their zero contribution in the off-diagonal plane. For their "classical components", they are equal to $(\omega_A + \delta\omega^+, \omega_B - \delta\omega^-)$ for the first point, and $(\omega_A + \delta\omega^-, \omega_B - \delta\omega^+)$ for the second one. However, it would be easier to express these diagonal coordinates with respect to those of the final state (ω'_A, ω'_B), in order to see where the Cauchy-Schwarz comparison points are relatively to the final state. For the first point (corresponding to $\widetilde{\mathcal{G}}^{(2e)}_{\hat{\rho}}(\omega_A + \delta\omega^+, \omega_B - \delta\omega^- \,|\, \omega_A + \delta\omega^+, \omega_B - \delta\omega^-)$), we have:

$$\begin{bmatrix} \omega_A + \delta\omega^+ \\ \omega_B - \delta\omega^- \end{bmatrix} = \begin{bmatrix} \omega_A + \varpi + \frac{\Delta\omega}{2} \\ \omega_B - \varpi + \frac{\Delta\omega}{2} \end{bmatrix} = \begin{bmatrix} \omega'_A + \frac{\Delta\omega}{2} \\ \omega'_B + \frac{\Delta\omega}{2} \end{bmatrix}. \tag{82}$$

This means that one of the two points to which we have to compare the post-scattering state is the point shifted by $+\frac{\Delta\omega}{2}$ along both axis. Doing the same manipulation for the second point, namely $\widetilde{\mathcal{G}}^{(2e)}_{\hat{\rho}}(\omega_A + \delta\omega^-, \omega_B - \delta\omega^+ \,|\, \omega_A + \delta\omega^-, \omega_B - \delta\omega^+)$, we obtain:

$$\begin{bmatrix} \omega_A + \delta\omega^- \\ \omega_B - \delta\omega^+ \end{bmatrix} = \begin{bmatrix} \omega_A + \varpi - \frac{\Delta\omega}{2} \\ \omega_B - \varpi - \frac{\Delta\omega}{2} \end{bmatrix} = \begin{bmatrix} \omega'_A - \frac{\Delta\omega}{2} \\ \omega'_B - \frac{\Delta\omega}{2} \end{bmatrix}. \tag{83}$$

Similarly, we have to compare the post-scattering state to the point shifted by $-\frac{\Delta\omega}{2}$ along both axis. The graphical representation of Cauchy-Schwarz criterion (77) is given in figure 22.

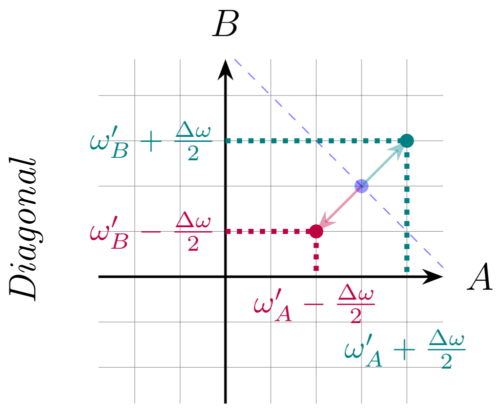

Figure 22: Localization of Cauchy-Schwarz criterion's right-hand side points (each color - purple and teal - corresponds to one point). Both states are diagonal, as their off-diagonal part is $(0, 0)$. However, their diagonal component is out of the hyperplane that conserves the total energy during the collision.

In figure 22, the fact that the two points giving the Cauchy-Schwarz upper bound do not respect the conservation of energy appears clearly, as their diagonal contributions are out of the line of slope -1 and crossing the point (ω'_A, ω'_B) that represents the final state. This 4D representation gives a clear visual interpretation of equation (79). Indeed, we see in figure 22 that, as the scattered state we consider is perfectly localized in energy, it translates into a point in this representation. Consequently, it is not spread along the line defined by the two Cauchy-Schwarz upper-bound points. As these points are located out of the energy-conservation line as soon as the output state is scattered ($\iff \Delta\omega \neq 0$), there is no overlap between the output state and the comparison points, which means that the criterion is violated. This is exactly the conclusion we deduced from equation (79).

4.3.2 Cauchy-Schwarz inequality in the scattering model

Until now, we only studied a criterion *based on* the Cauchy-Schwarz inequality, but different from the original inequality. Indeed, the true Cauchy-Schwarz relation being a general mathematical result, it cannot be violated by any physical state, whether it be separable or entangled. In this section, we will do the same study as previously, but starting from the general Cauchy-Schwarz inequality (47). We recall here its expression in terms of operators:

$$|\langle \hat{A}_1 \hat{A}_2 \hat{B}_1 \hat{B}_2 \rangle_{\hat{\rho}}|^2 \leq \langle \hat{A}_1 \hat{A}_1^\dagger \hat{B}_1 \hat{B}_1^\dagger \rangle_{\hat{\rho}} \, \langle \hat{A}_2^\dagger \hat{A}_2 \hat{B}_2^\dagger \hat{B}_2 \rangle_{\hat{\rho}}. \tag{84}$$

Derivation of the $\hat{S}$-matrix coefficients expression

Like in the first section, we replace the four-operators set $\{\hat{A}_1, \hat{A}_2, \hat{B}_1, \hat{B}_2\}$ with fermionic creation operators $\{\hat{c}_A^\dagger[\omega_A], \hat{c}_A[\omega'_A], \hat{c}_B^\dagger[\omega_B], \hat{c}_B[\omega'_B]\}$. Then, the inequality becomes:

$$\begin{aligned} &|\langle \hat{c}_A^\dagger[\omega_A]\, \hat{c}_A[\omega'_A]\, \hat{c}_B^\dagger[\omega_B]\, \hat{c}_B[\omega'_B] \rangle_{\hat{\rho}}|^2 \\ &\qquad \leq \langle \hat{c}_A^\dagger[\omega_A]\, \hat{c}_A[\omega_A]\, \hat{c}_B^\dagger[\omega_B]\, \hat{c}_B[\omega_B] \rangle_{\hat{\rho}} \, \langle \hat{c}_A^\dagger[\omega'_A]\, \hat{c}_A[\omega'_A]\, \hat{c}_B^\dagger[\omega'_B]\, \hat{c}_B[\omega'_B] \rangle_{\hat{\rho}}. \end{aligned} \tag{85}$$

Using the $\mathcal{G}^{(2e)}$-function to simplify the previous expression, we find that equation (85) is equivalent to:

$$|\mathcal{G}^{(2e)}_{\hat{\rho}}(\omega'_A, \omega'_B \,|\, \omega_A, \omega_B)|^2 \leq \mathcal{G}^{(2e)}_{\hat{\rho}}(\omega_A, \omega_B \,|\, \omega_A, \omega_B)\, \mathcal{G}^{(2e)}_{\hat{\rho}}(\omega'_A, \omega'_B \,|\, \omega'_A, \omega'_B) \tag{86}$$

In order to follow the same reasoning as for criterion (48), we express the arguments in the $\mathcal{G}^{(2e)}$-function relatively to the input energies ω_A and ω_B by introducing the four variables $\delta\omega_A$, $\delta\omega'_A$, $\delta\omega_B$, and $\delta\omega'_B$:

$$\begin{aligned}
&|\widetilde{\mathcal{G}}^{(2e)}_{\hat{\rho}}(\omega_A + \delta\omega_A^+, \omega_B - \delta\omega_B^+ \,|\, \omega_A + \delta\omega_A^-, \omega_B - \delta\omega_B^-)|^2 \\
&\qquad \leq \widetilde{\mathcal{G}}^{(2e)}_{\hat{\rho}}(\omega_A + \delta\omega_A^-, \omega_B - \delta\omega_B^- \,|\, \omega_A + \delta\omega_A^-, \omega_B - \delta\omega_B^-) \\
&\qquad\quad \widetilde{\mathcal{G}}^{(2e)}_{\hat{\rho}}(\omega_A + \delta\omega_A^+, \omega_B - \delta\omega_B^+ \,|\, \omega_A + \delta\omega_A^+, \omega_B - \delta\omega_B^+).
\end{aligned} \tag{87}$$

The argument on the electrons' scattering in the Fermi remains valid here. Then, for the same reasons as before, we now only consider the case:

$$\begin{aligned}
\delta\omega_A^- = \delta\omega_B^- := \delta\omega^- \quad &\text{and} \quad -\omega_A \leq \delta\omega^- \leq \omega_B \\
\delta\omega_A^+ = \delta\omega_B^+ := \delta\omega^+ \quad &\text{and} \quad -\omega_A \leq \delta\omega^+ \leq \omega_B.
\end{aligned}$$

Besides, we still keep the hypothesis that $\delta\omega \neq \delta\omega'$ in order not to have a trivial inequality. These considerations allow us to write the Cauchy-Schwarz inequality under a slightly lighter form:

$$\begin{aligned}
&|\widetilde{\mathcal{G}}^{(2e)}_{\hat{\rho}}(\omega_A + \delta\omega^+,\, \omega_B - \delta\omega^+ \,|\, \omega_A + \delta\omega^-,\, \omega_B - \delta\omega^-)|^2 \\
&\qquad \leq \widetilde{\mathcal{G}}^{(2e)}_{\hat{\rho}}(\omega_A + \delta\omega^-,\, \omega_B - \delta\omega^- \,|\, \omega_A + \delta\omega^-,\, \omega_B - \delta\omega^-) \\
&\qquad\quad \widetilde{\mathcal{G}}^{(2e)}_{\hat{\rho}}(\omega_A + \delta\omega^+,\, \omega_B - \delta\omega^+ \,|\, \omega_A + \delta\omega^+,\, \omega_B - \delta\omega^+).
\end{aligned} \tag{88}$$

Using equation (75) derived previously, we can now translate equation (88) into an expression involving only $\hat{S}$-matrix coefficients:

$$|S(\delta\omega^-; \omega_A, \omega_B)^* S(\delta\omega^+; \omega_A, \omega_B)|^2 \leq |S(\delta\omega^-; \omega_A, \omega_B)|^2\, |S(\delta\omega^+; \omega_A, \omega_B)|^2. \tag{89}$$

Inequality (84) is actually an equality, and is then always true: we indeed find that every physical state verifies the Cauchy-Schwarz inequality, like expected and differently from criterion (47). Let's now look at how this inequality can be visualized graphically.

Geometrical interpretation of the general Cauchy-Schwarz inequality

In the following, we will once again consider two quantum paths along which quantities $\delta\omega^+$ and $\delta\omega^-$ of energy have been transferred from one electron of the initial state to the other. Like previously, we also define the variables $\overline{\omega} := \frac{\delta\omega^+ + \delta\omega^-}{2}$ and $\Delta\omega := \delta\omega^+ - \delta\omega^-$.

First, we can notice that in criterion (47) as well as in inequality (84), the left-hand side member is the same: only the right-hand side member changes from the criterion to the general inequality. Then all the discussion made on the final state after scattering and represented in figures 20 and 22 remain true. However, the points constituting the upper-bound (represented in figure 23), and to which we must compare the final state, changed.

Indeed, these points now have $\big((\omega_A + \delta\omega^+, \omega_B - \delta\omega^+), (0,0)\big)$ and $\big((\omega_A + \delta\omega^-, \omega_B - \delta\omega^-), (0,0)\big)$ as 4D-coordinates. Expressing these coordinates relatively those of the scattered state $(\omega'_A = \omega_A + \overline{\omega}, \omega'_B = \omega_B - \overline{\omega})$, we obtain $\big((\omega'_A + \frac{\Delta\omega}{2}, \omega'_B - \frac{\Delta\omega}{2}), (0,0)\big)$ and $\big((\omega'_A - \frac{\Delta\omega}{2}, \omega'_B + \frac{\Delta\omega}{2}), (0,0)\big)$. Figure 23 gives a visual representation of the two "new" points corresponding to the right-hand side member of equation (88).

We notice that this time, the two upper-bound points are located on the line of slope -1 an crossing the point corresponding to the post-scattering state (represented in blue in figure 23). Thus, these points represent states that respect the conservation of energy.

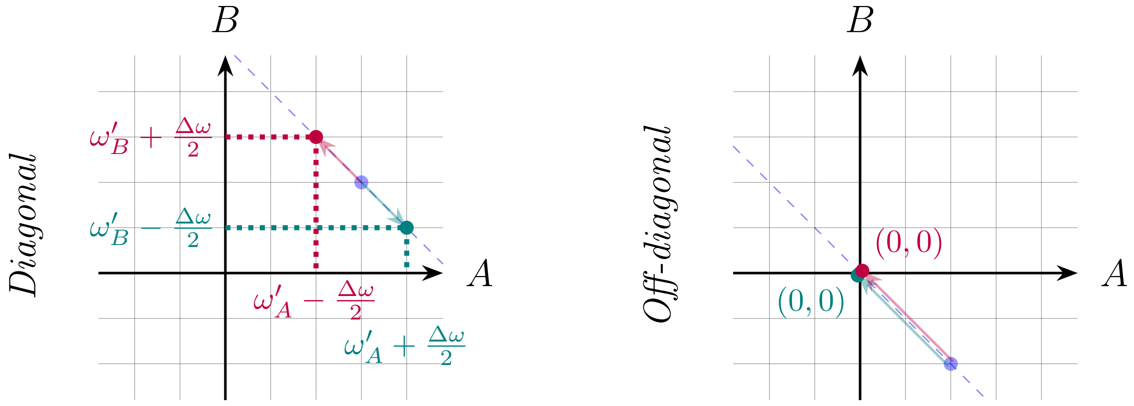

Figure 23: Localization of Cauchy-Schwarz inequality's right-hand side points. Like for the Cauchy-Schwarz criterion, both points are still diagonal, as their coherence's off-diagonal part is null. However, their diagonal contribution is now moved in the direction that conserves the total energy: this partly explains why the inequality is always respected by physical states, contrary to the criterion.

Finally, if we want to visualize the Cauchy-Schwarz inequality in the $(\delta\omega, \delta\Omega)$ plane, we first need to translate the right-hand side points' 4D-coordinates into the corresponding 2D-coordinates. We find:

$$\begin{cases} (\omega'_A - \omega'_B + \Delta\omega, 0) = (\omega_A - \omega_B + 2\overline{\omega} + \Delta\omega, 0) = (\omega_A - \omega_B + 2\delta\omega^+, 0) \\ (\omega'_A - \omega'_B - \Delta\omega, 0) = (\omega_A - \omega_B + 2\overline{\omega} - \Delta\omega, 0) = (\omega_A - \omega_B + 2\delta\omega^-, 0) \end{cases} \tag{90}$$

Figure 24 then shows the geometrical representation of the general Cauchy-Schwarz inequality in the $(\delta\omega, \delta\Omega)$ plane. We see that both points of the right-hand side member are represented by two distinct points (see the purple and teal points in figure 24) along the $\delta\omega = 0$ line. This is completely normal, as the Cauchy-Schwarz upper-bounds are always diagonal (see equation (88)). Even though they were also diagonal in the case of the entanglement criterion, these points were not represented in figure 20. Indeed, in the previous case, the Cauchy-Schwarz comparison points were located in a dimension which was orthogonal to the figure. Hence, they could not be visualized.

Here, we gave the example of an arbitrary scattered state, represented by the blue point in figure 24. We see that the two Cauchy-Schwarz comparison points corresponding to this state are, by construction, always located in the diamond. Indeed, each scattered state is upper-bounded by the intersection points of the two lines crossing the scattered state's point ad parallel to the sides of the diamond with the $\delta\omega = 0$ line. That way, any point located in the diamond is always bounded by two points also located in the diamond. This is the visual interpretation of why the Cauchy-Schwarz inequality is true for any scattered state.

On the other hand, we already mentioned that in the case of the entanglement criterion, both Cauchy-Schwarz comparison points are located in an orthogonal dimension. As the diamond obtained here is completely "flat", and not spread in any transverse dimension, we understand better why the criterion is almost always violated in the case of perfectly energy-localized electrons. The only way for the criterion to be respected is if the upper-bound points remain in the plane defined by the diamond, meaning if the electrons do not scatter ($\iff$ $\Delta\omega = 0$). Of course, the situation would be different if we considered more realistic input states with not-perfectly-determined energies. In such cases, the diamond of the scattered states would spread in orthogonal dimensions, and the criterion could then be respected even if the electrons have scattered and if the comparison points are out of the $(\delta\omega, \delta\Omega)$ plane.

We started to study such input wave-packets at the end of this internship, but did not have the time to obtain important results that we could present here. Nevertheless, we showed the considering two Landau wave-packets - defined by a Lorentzian energy distribution - as input states, the diamond indeed

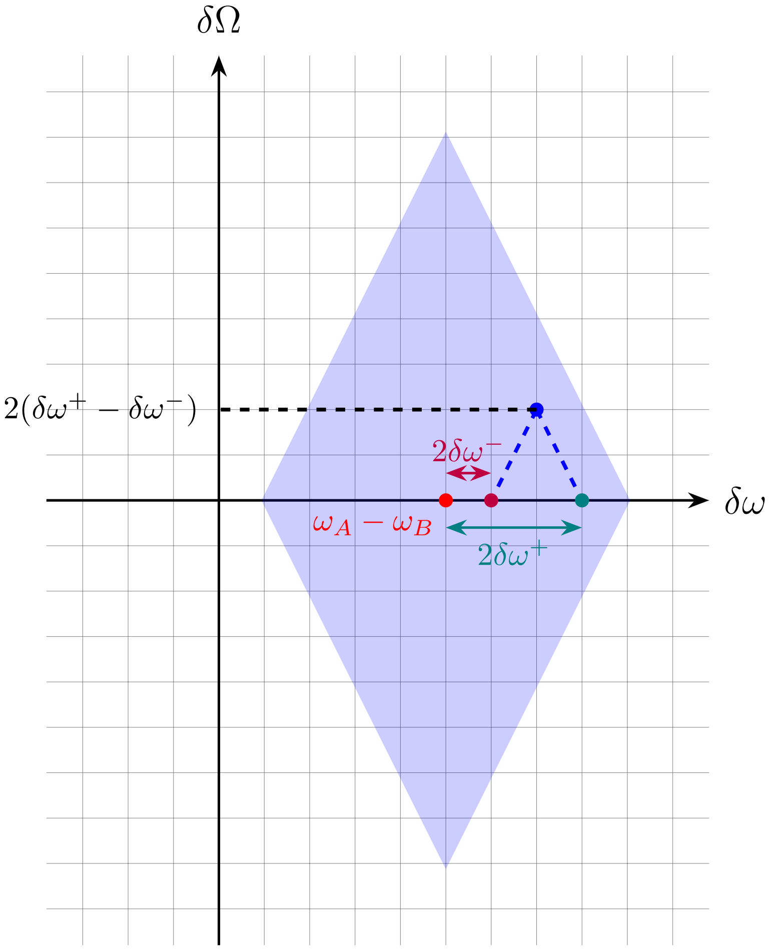

Figure 24: Geometrical interpretation of the Cauchy-Schwarz inequality in the $(\delta\omega, \delta\Omega)$ plane. The x-axis represents the coherence's diagonal part and the y-axis the off-diagonal part. The red point corresponds to the initial state, and the blue diamond the area in which this state can be moved by the scattering process. We gave the example of an arbitrary scattered state, represented by the blue point. The comparison points of Cauchy-Schwarz's inequality corresponding to this state are represented by the teal and purple points, and are located in the diamond.

spreads in transverse dimensions, giving the possibility to respect the entanglement criterion even with a scattered output state.

5 Conclusion

During this work, we investigated several problems relative to the manipulation and determination of the information carried by an electron in a mesoscopic quantum conductor. These questions are currently central in the field of electron quantum optics, given the exponentially growing interest regarding the perspective to design electron-based quantum computers. This idea relies on a new paradigm of quantum computation, functioning with delocalized qubits submitted to measurements on a common hardware. Several leads are currently studied in order to make such so-called electronic *flying* qubits, but the most promising is probably to use Levitonic excitations propagating in quantum Hall edge channels [10]. By delocalizing these Levitons into two channels, we create what is called a railroad qubit. Then, it becomes possible to generate entanglement between the channels, and communicate information among a quantum mesoscopic system.

The first study realized during this internship deals with the full determination of an electronic excitation's quantum state. To do so, an electron quantum tomography protocol based on two-particle Hong-Ou-Mandel interferometry technique has already been proved to work [5]. However, this method presents one major drawback. Indeed, the measurement time required to determinate the state of a single electron can be several days long, depending on the excitation's complexity and the precision needed. This is a consequence of the fact that this protocol is theoretically complete, but not optimized: in this sense, the Hong-Ou-Mandel tomography is more a proof of concept than an experimental technique that can be used in practice. Our contribution concerning this problem has been the development of an increased version of this protocol. Instead of determining the electron's first-order electronic coherence with pure sinusoidal signals at different frequencies (like for the HOM protocol), the work presented here uses linear combinations of such signals to have a more tunable and efficient exploration of the frequency space we want to probe. This is made possible because the electric charge carried by a single excitation is really small, otherwise this idea would not provide reliable results. Selecting particular linear combinations of the basic sinusoidal signals (harmonics), we build wavelets that result in a probing signal composed of a periodic succession of voltage pulses.

For now, only the theoretical side of such a protocol has been investigated, but it has never been experimentally tested yet. However, we already have good reasons to believe that this work allowed a significant progress compared to the HOM protocol, as this method allows the experimentalist to tune the probing signal in order to probe any very specific area of the frequency space, tuning the bias voltage and the number of harmonics considered to build the wavelet. At the first order in the electric charge carried by the excitation, we demonstrated that this protocol gives access to the electron-hole coherences. We even extended the study to the second-order, and showed that the electron-electron and hole-hole coherences became accessible from this order. Finally, we also checked that the number of harmonics theoretically needed to obtain sufficiently precise estimations is perfectly compatible with the experimental reality.

Then the second part of this work concerned the study of three entanglement criteria when applied electronic states. Working on such inequalities is the first step in the perspective of manipulating the information carried by individual electrons. By evaluating and quantifying the entanglement created when two electrons interact, it becomes possible to use it in order to make operations on electronic qubits. Hence, adapting entanglement criteria to electron quantum optics allows us to gain a better insight on electronic states' degree of entanglement. The most general of these criteria was directly derived from the Cauchy-Schwarz inequality [29]. The two others are particular cases of the first one, and were first mathematically studied by Hillery and Zubairy [18]. Starting from their mathematical form, we first adapted them to the formalism of EQO and gave their expressions as inequalities on products of first-order and second-order electronic coherence functions. In order to better visualize the physical meaning of these criteria, we then developed a representation in terms of spin-operators so that we can easily represent the separable and entangled electron states on the Bloch sphere. By doing this, we saw that despite their apparent similarity, the two Hillery-Zubairy criteria were not equivalent, and this allowed us to evaluate their strength.

Finally, we made a detailed study of the most general criterion in the case of a coherent collision between two electrons. For that matter, we considered a simple two-particle coherent scattering model, and evaluated the possible two-electron states after the collision in order to compare them to the criterion. Doing so, we were able to determine whether the collision could create entanglement. In the case of two perfectly energy-localized input wave-packets, we saw that the criterion was violated as soon as the energy transfer during the collision has a non-zero quantum component, confirming the idea that making two electrons interact entangles them. As a sanity-check, we studied the same situation and compared the final states to the original Cauchy-Schwarz inequality. As this mathematical relation is always true, we logically observed that any of the possible output states respected it.

At the end of the day, these studies allowed us to obtain numerous interesting results, as well in the determination of an electron's quantum state as in its manipulation in order to create entanglement. Nevertheless, all this new knowledge is only a small part in the process leading to important scientific progress. In order to exploit these results in the best way, we can first and foremost think about testing the pulse-train tomography protocol experimentally. To start, it would be relevant to test the protocol with simple wave-packets such as Levitons like in [5], so that we can compare the results given by both protocols. If the results obtained with the pulse-train protocol happen to be concluant, it would then be interesting to test it with more complex states in order to evaluate its general performances and the time gained compared to the HOM protocol. Then, the development of an electron quantum tomography protocol based on the second-order electronic coherence would be another lead in the full-determination of a quantum state, potentially granting access to an even more efficient reconstruction process, or to new experimental possibilities.

Regarding the entanglement created by a collision between two electrons, the next step would be to study the physical implications of the Cauchy-Schwarz criterion with two "more realistic" input electronic excitations, such as Landau wave-packets that are delocalized in energy. In this situation, we expect the conditions for the output states to respect the criterion to be a bit less restricting than with perfectly localized states. Indeed, the more delocalized the input states, the harder it should be to violate the criterion and create entangled states. Of course, an even more interesting result would be the case of Levitonic input wave-packets, as these are the mainly used excitations in practice. Going even further, the last step of this study would be to obtain results when a non-coherent scattering model is considered. Indeed, realistically, we need to consider that a fraction of the input energy is not transferred between the electrons bu lost in the environment: such considerations would result in a pretty general model, and should be able to predict the results of future experimental works. Another perpective is to go further than simply study whether the output state is entangled or not, and find good indicators to quantify the degree of entanglement after a collision. All these ideas are part of a PhD thesis project beginning in the fall of 2025, in the direct continuity of what has been done during this 6-month internship.

A Appendix: computation of the second-order coherence function

Let's start with writing the second-order coherence function explicitly in the case $\hat{\rho} = |\psi\rangle\langle\psi|$, where $|\psi\rangle$ is defined as in equation (70):

$$\begin{aligned}
&\mathcal{G}^{(2e)}_{\hat{\rho}}(\omega_A + \delta\omega_A^+, \omega_B - \delta\omega_B^+ \mid \omega_A + \delta\omega_A^-, \omega_B - \delta\omega_B^-) \\
&\quad = \langle \hat{c}^\dagger_A[\omega_A + \delta\omega_A^-]\hat{c}^\dagger_B[\omega_B - \delta\omega_B^-]\hat{c}_B[\omega_B - \delta\omega_B^+]\hat{c}_A[\omega_A + \delta\omega_A^+]\rangle_{\hat{\rho}} \\
&\quad = \iint_{\mathbb{R}^2} d\omega\ d\omega'\ S(\omega';\omega_A,\omega_B)^* S(\omega;\omega_A,\omega_B)\langle \hat{c}_B[\omega_B - \omega']\hat{c}_A[\omega_A + \omega']\hat{c}^\dagger_A[\omega_A + \delta\omega_A^-]\hat{c}^\dagger_B[\omega_B - \delta\omega_B^-] \\
&\qquad \hat{c}_B[\omega_B - \delta\omega_B^+]\hat{c}_A[\omega_A + \delta\omega_A^+]\hat{c}^\dagger_A[\omega_A + \omega]\hat{c}^\dagger_B[\omega_B - \omega]\rangle_F .
\end{aligned} \tag{91}$$

In equation (91), the notation $\langle\cdot\rangle_F$ means that the quantum expectation value is calculated on the state $|F\rangle$ corresponding to the Fermi sea. Let's call Λ the eight-points correlation function appearing in the integral expression in (91). Using Wick's theorem, it is possible to decompose Λ into a combination of two-points correlation functions. Due to the fermionic super-selection rule - forbidding any superposition of states with particle-numbers of different parities -, numerous terms vanish in the decomposition, and the final result is a sum of only four terms:

$$\begin{aligned}
\Lambda = \ & \left.\begin{matrix} \langle \hat{c}_B[\omega_B - \omega']\hat{c}^\dagger_B[\omega_B - \delta\omega_B]\rangle_F \langle \hat{c}_B[\omega_B - \delta\omega'_B]\hat{c}^\dagger_B[\omega_B - \omega]\rangle_F \\ \langle \hat{c}_A[\omega_A + \omega']\hat{c}^\dagger_A[\omega_A + \delta\omega_A]\rangle_F \langle \hat{c}_A[\omega_A + \delta\omega'_A]\hat{c}^\dagger_A[\omega_A + \omega]\rangle_F \end{matrix}\right\} [1] \\
+ \ & \left.\begin{matrix} \langle \hat{c}_B[\omega_B - \omega']\hat{c}^\dagger_B[\omega_B - \omega]\rangle_F \langle \hat{c}^\dagger_B[\omega_B - \delta\omega_B]\hat{c}_B[\omega_B - \delta\omega'_B]\rangle_F \\ \langle \hat{c}_A[\omega_A + \omega']\hat{c}^\dagger_A[\omega_A + \delta\omega_A]\rangle_F \langle \hat{c}_A[\omega_A + \delta\omega'_A]\hat{c}^\dagger_A[\omega_A + \omega]\rangle_F \end{matrix}\right\} [2] \\
+ \ & \left.\begin{matrix} \langle \hat{c}_B[\omega_B - \omega']\hat{c}^\dagger_B[\omega_B - \delta\omega_B]\rangle_F \langle \hat{c}_B[\omega_B - \delta\omega'_B]\hat{c}^\dagger_B[\omega_B - \omega]\rangle_F \\ \langle \hat{c}_A[\omega_A + \omega']\hat{c}^\dagger_A[\omega_A + \omega]\rangle_F \langle \hat{c}^\dagger_A[\omega_A + \delta\omega_A]\hat{c}_A[\omega_A + \delta\omega'_A]\rangle_F \end{matrix}\right\} [3] \\
+ \ & \left.\begin{matrix} \langle \hat{c}_B[\omega_B - \omega']\hat{c}^\dagger_B[\omega_B - \omega]\rangle_F \langle \hat{c}^\dagger_B[\omega_B - \delta\omega_B]\hat{c}^\dagger_B[\omega_B - \delta\omega'_B]\rangle_F \\ \langle \hat{c}_A[\omega_A + \omega']\hat{c}^\dagger_A[\omega_A + \omega]\rangle_F \langle \hat{c}^\dagger_A[\omega_A + \delta\omega_A]\hat{c}_A[\omega_A + \delta\omega'_A]\rangle_F \end{matrix}\right\} [4]
\end{aligned} \tag{92}$$

In order to express the $\mathcal{G}^{(2e)}$ function, we need to compute the double integral of (91) for each of the four terms in the right-hand side of (92). Let's begin with the first term.

Computation of the first term

$$\begin{aligned}
&\iint_{\mathbb{R}^2} d\omega\ d\omega'\ S(\omega';\omega_A,\omega_B)^* S(\omega;\omega_A,\omega_B)[1] \\
&\qquad = \int_{\mathbb{R}} d\omega'\ S(\omega';\omega_A,\omega_B)^* \langle \hat{c}_B[\omega_B - \omega']\hat{c}^\dagger_B[\omega_B - \delta\omega_B^-]\rangle_F \langle \hat{c}_A[\omega_A + \omega']\hat{c}^\dagger_A[\omega_A + \delta\omega_A^-]\rangle_F \\
&\qquad\quad \int_{\mathbb{R}} d\omega\ S(\omega;\omega_A,\omega_B)\langle \hat{c}_B[\omega_B - \delta\omega_B^+]\hat{c}^\dagger_B[\omega_B - \omega]\rangle_F \langle \hat{c}_A[\omega_A + \delta\omega_A^+]\hat{c}^\dagger_A[\omega_A + \omega]\rangle_F
\end{aligned} \tag{93}$$

Now, we use the fact that $\langle \hat{c}^\dagger_\alpha[\Omega]\hat{c}_\beta[\Omega']\rangle_F = \delta_{\alpha\beta}\delta(\Omega - \Omega')f_T(\Omega)$, where f_T is the Fermi-Dirac distribution at temperature T. As we consider the case $T = 0$, we have $f_{T=0}(\Omega) = \Theta(-\Omega)$ with Θ being the Heaviside function. Using the fermionic anti-commutation relation $\{\hat{c}_\alpha[\Omega], \hat{c}^\dagger_\beta[\Omega']\} = \delta_{\alpha\beta}\delta(\Omega - \Omega')\mathbb{I}$, we finally obtain the relation:

$$\langle \hat{c}_\alpha[\Omega]\hat{c}^\dagger_\beta[\Omega']\rangle_F = \delta_{\alpha\beta}\delta(\Omega - \Omega')\Theta(\Omega). \tag{94}$$

Inserting this expression in (93), we have:

$$\begin{aligned}&\iint_{\mathbb{R}^2} d\omega\ d\omega'\ S(\omega';\omega_A,\omega_B)^* S(\omega;\omega_A,\omega_B)[1]\\&\quad= \int_{\mathbb{R}} d\omega'\ S(\omega';\omega_A,\omega_B)^* \delta(\omega'-\delta\omega_B^-)\Theta(\omega_B-\delta\omega_B^-)\delta(\omega'-\delta\omega_A^-)\Theta(\omega_A+\delta\omega_A^-)\\&\quad\int_{\mathbb{R}} d\omega\ S(\omega;\omega_A,\omega_B)\delta(\omega-\delta\omega_B^+)\Theta(\omega_B-\delta\omega_B^+)\delta(\omega-\delta\omega_A^+)\Theta(\omega_A+\delta\omega_A^+)\end{aligned} \tag{95}$$

The final result for this first term is then:

$$\begin{aligned}&\iint_{\mathbb{R}^2} d\omega\ d\omega'\ S(\omega';\omega_A,\omega_B)^* S(\omega;\omega_A,\omega_B)[1]\\&\quad= \delta(\delta\omega_A-\delta\omega_B^-)\delta(\delta\omega_A^+-\delta\omega_B^+)S(\delta\omega_A^-;\omega_A,\omega_B)^* S(\delta\omega_A^+;\omega_A,\omega_B)\\&\qquad\Theta(\omega_B-\delta\omega_A^-)\Theta(\omega_A+\delta\omega_A^-)\Theta(\omega_B-\delta\omega_A^+)\Theta(\omega_A+\delta\omega_A^+)\end{aligned} \tag{96}$$

Computation of the second term

Using (94) and the identity $1-\Theta(\Omega)=\Theta(-\Omega)$, we can write:

$$\begin{aligned}&\iint_{\mathbb{R}^2} d\omega\ d\omega'\ S(\omega';\omega_A,\omega_B)^* S(\omega;\omega_A,\omega_B)[2]\\&\quad= \delta(\delta\omega_B^--\delta\omega_B^+)\Theta(\delta\omega_B^--\omega_B)\iint_{\mathbb{R}^2} d\omega\ d\omega'\ S(\omega';\omega_A,\omega_B)^* S(\omega;\omega_A,\omega_B)\\&\qquad\delta(\omega-\omega')\Theta(\omega_B-\omega)\delta(\omega'-\delta\omega_A^+)\Theta(\omega_A+\delta\omega_A^-)\delta(\omega-\delta\omega_A^+)\Theta(\omega_A+\delta\omega_A^+)\end{aligned} \tag{97}$$

Computing the integrals, we obtain:

$$\begin{aligned}&\iint_{\mathbb{R}^2} d\omega\ d\omega'\ S(\omega';\omega_A,\omega_B)^* S(\omega;\omega_A,\omega_B)[2]\\&\quad= \delta(\delta\omega_A^--\delta\omega_A^+)\delta(\delta\omega_B^--\delta\omega_B^+)|S(\delta\omega_A^+;\omega_A,\omega_B)|^2\Theta(\delta\omega_B^--\omega_B)\Theta(\omega_B-\delta\omega_A^-)\Theta(\omega_A+\delta\omega_A^-)\end{aligned} \tag{98}$$

Computation of the third term

For this term, the computation is the same as for the second one. We obtain:

$$\begin{aligned}&\iint_{\mathbb{R}^2} d\omega\ d\omega'\ S(\omega';\omega_A,\omega_B)^* S(\omega;\omega_A,\omega_B)[3]\\&\quad= \delta(\delta\omega_A^--\delta\omega_A^+)\Theta(-\delta\omega_A^--\omega_A)\iint_{\mathbb{R}^2} d\omega\ d\omega'\ S^*(\omega';\omega_A,\omega_B) S(\omega;\omega_A,\omega_B)\\&\qquad\delta(\omega-\omega')\Theta(\omega_A+\omega)\delta(\omega'-\delta\omega_B^-)\Theta(\omega_B-\delta\omega_B^-)\delta(\omega-\delta\omega_B^+)\Theta(\omega_B-\delta\omega_B^+)\end{aligned} \tag{99}$$

Simplifying the expression, this gives:

$$\begin{aligned}&\iint_{\mathbb{R}^2} d\omega\ d\omega'\ S(\omega';\omega_A,\omega_B)^* S(\omega;\omega_A,\omega_B)[3]\\&\quad= \delta(\delta\omega_A^--\delta\omega_A^+)\delta(\delta\omega_B^--\delta\omega_B^+)|S(\delta\omega_B^-;\omega_A,\omega_B)|^2\Theta(-\delta\omega_A^--\omega_A)\Theta(\omega_A+\delta\omega_B^-)\Theta(\omega_B-\delta\omega_B^-)\end{aligned} \tag{100}$$

Computation of the fourth term

To conclude, let's now compute the integral of the last term:

$$\begin{aligned}
&\iint_{\mathbb{R}^2} d\omega\ d\omega'\ S(\omega';\omega_A,\omega_B)^* S(\omega;\omega_A,\omega_B)[4] \\
&\quad = \delta(\delta\omega_A^- - \delta\omega_A^+)\Theta(-\delta\omega_A^- - \omega_A)\delta(\delta\omega_B^- - \delta\omega_B^+)\Theta(\delta\omega_B^- - \omega_B)\iint_{\mathbb{R}^2} d\omega\ d\omega' S(\omega';\omega_A,\omega_B)^* \\
&\qquad S(\omega;\omega_A,\omega_B)\delta(\omega-\omega')\Theta(\omega_B-\omega)\delta(\omega-\omega')\Theta(\omega_A+\omega) \\
&\quad = \delta(\delta\omega_A^- - \delta\omega_A^+)\delta(\delta\omega_B^- - \delta\omega_B^+)\Theta(-\delta\omega_A^- - \omega_A)\Theta(\delta\omega_B^- - \omega_B)\int_{-\omega_A}^{\omega_B} d\omega\ |S(\omega;\omega_A,\omega_B)|^2
\end{aligned} \tag{101}$$

Finally, by unitarity of the $\hat{S}$ matrix, we have $\int_{-\omega_A}^{\omega_B} d\omega\ |S(\omega;\omega_A,\omega_B)|^2 = 1$. Then, the result is:

$$\begin{aligned}
&\iint_{\mathbb{R}^2} d\omega\ d\omega'\ S(\omega';\omega_A,\omega_B)^* S(\omega;\omega_A,\omega_B)[4] \\
&\qquad = \delta(\delta\omega_A^- - \delta\omega_A^+)\delta(\delta\omega_B^- - \delta\omega_B^+)\Theta(-\delta\omega_A^- - \omega_A)\Theta(\delta\omega_B^- - \omega_B)
\end{aligned} \tag{102}$$

Final expression of the $\mathcal{G}^{(2e)}$ function

Adding the four expressions we obtained by integrating each term of Λ, we can now express the full $\mathcal{G}^{(2e)}$ function:

$$\begin{aligned}
&\mathcal{G}^{(2e)}_{\hat{\rho}}(\omega_A + \delta\omega_A^+, \omega_B - \delta\omega_B^+ \mid \omega_A + \delta\omega_A^-, \omega_B - \delta\omega_B^-) \\
&\quad = \delta(\delta\omega_A^- - \delta\omega_B^-)\delta(\delta\omega_A^+ - \delta\omega_B^+)S(\delta\omega_A^-;\omega_A,\omega_B)^* S(\delta\omega_A^+;\omega_A,\omega_B) \\
&\qquad \Theta(\omega_B - \delta\omega_A^+)\Theta(\omega_A + \delta\omega_A^+)\Theta(\omega_A + \delta\omega_A^-)\Theta(\omega_B - \delta\omega_A^-) \\
&\quad + \delta(\delta\omega_B^- - \delta\omega_B^+)\delta(\delta\omega_A^- - \delta\omega_A^+)\Big[\Theta(\delta\omega_B^+ - \omega_B)\Theta(\omega_B - \delta\omega_A^+) \\
&\qquad \Theta(\omega_A + \delta\omega_A^+)|S(\delta\omega_A^+;\omega_A,\omega_B)|^2 + \Theta(-\delta\omega_A^+ - \omega_A)\Theta(\omega_A + \delta\omega_B^-) \\
&\qquad \Theta(\omega_B - \delta\omega_B^+)|S(\delta\omega_B^+;\omega_A,\omega_B)|^2 + \Theta(-\delta\omega_A^+ - \omega_A)\Theta(\delta\omega_B^+ - \omega_B)\Big]
\end{aligned} \tag{103}$$

References

[1] Aspect, A., Dalibard, J., and Roger, G. Experimental test of bell's inequalities using time-varying analyzers. *Phys. Rev. Lett. 49* (Dec 1982), 1804–1807.

[2] Bell, J. S. On the einstein podolsky rosen paradox. *Physics Physique Fizika 1* (Nov 1964), 195–200.

[3] Benatti, F., Floreanini, R., Franchini, F., and Marzolino, U. Entanglement in indistinguishable particle systems. *Physics Reports 878* (Sept. 2020).

[4] Bertoni, A., Bordone, P., Brunetti, R., Jacoboni, C., and Reggiani, S. Quantum logic gates based on coherent electron transport in quantum wires. *Phys. Rev. Lett. 84* (Jun 2000), 5912–5915.

[5] Bisognin, R., Marguerite, A., Roussel, B., Kumar, M., Cabart, C., Chapdelaine, C., Mohammad-Djafari, A., Berroir, J.-M., Bocquillon, E., Plaçais, B., Cavanna, A., Gennser, U., Jin, Y., Degiovanni, P., and Fève, G. Quantum tomography of electrical currents. *Nature Communications 10*, 1 (July 2019).

[6] Bocquillon, E., Freulon, V., Berroir, J.-M., Degiovanni, P., Plaçais, B., Cavanna, A., Jin, Y., and Fève, G. Coherence and indistinguishability of single electrons emitted by independent sources. *Science 339*, 6123 (2013), 1054–1057.

[7] Bocquillon, E., Parmentier, F. D., Grenier, C., Berroir, J.-M., Degiovanni, P., Glattli, D. C., Plaçais, B., Cavanna, A., Jin, Y., and Fève, G. Electron quantum optics: Partitioning electrons one by one. *Phys. Rev. Lett. 108* (2012), 196803.

[8] Degiovanni, P., Portier, N., Cabart, C., Feller, A., and Roussel, B. *Physique quantique, Information et Calcul: des concepts aux applications.* jan 2020.

[9] Dubois, J., Jullien, T., Portier, F., Roche, P., Cavanna, A., Jin, Y., Wegscheider, W., Roulleau, P., and Glattli, D. Minimal-excitation states for electron quantum optics using levitons. *Nature 502* (10 2013).

[10] Edlbauer, H., Wang, J., Crozes, T., Perrier, P., Ouacel, S., Geffroy, C., Georgiou, G., Chatzikyriakou, E., Lacerda-Santos, A., Waintal, X., Glattli, D. C., Roulleau, P., Nath, J., Kataoka, M., Splettstoesser, J., Acciai, M., da Silva Figueira, M. C., Öztas, K., Trellakis, A., Grange, T., Yevtushenko, O. M., Birner, S., and Bäuerle, C. Semiconductor-based electron flying qubits: review on recent progress accelerated by numerical modelling. *EPJ Quantum Technology 9*, 1 (aug 2022).

[11] Einstein, A., Podolsky, B., and Rosen, N. Can quantum-mechanical description of physical reality be considered complete? *Phys. Rev. 47* (May 1935), 777–780.

[12] Ferraro, D., Feller, A., Ghibaudo, A., Thibierge, E., Bocquillon, E., Fève, G., Grenier, C., and Degiovanni, P. Wigner function approach to single electron coherence in quantum hall edge channels. *Phys. Rev. B 88* (Nov 2013), 205303.

[13] Fève, G. *Quantification du courant alternatif : la boîte quantique comme source d' électrons uniques subnanoseconde.* Thèse de doctorat, Université Pierre et Marie Curie - Paris VI, Nov. 2006.

[14] Filippone, M., Marguerite, A., Le Hur, K., Fève, G., and Mora, C. Phase-coherent dynamics of quantum devices with local interactions. *Entropy 22*, 8 (July 2020), 847.

[15] Forrester, M., and Kusmartsev, F. Graphene levitons and anti-levitons in magnetic fields. *Nanoscale 6* (05 2014), 7594–7603.

[16] Glattli, D. C., Nath, J., Taktak, I., Roulleau, P., Bauerle, C., and Waintal, X. Design of a single-shot electron detector with sub-electron sensitivity for electron flying qubit operation. *arXiv* (2020).

[17] Grenier, C. *Electronic quantum optics.* Theses, Ecole normale supérieure de lyon - ENS LYON, June 2011.

[18] Hillery, M., and Zubairy, M. S. Entanglement conditions for two-mode states: Applications. *Physical Review A 74*, 3 (Sept. 2006).

[19] Hong, C. K., Ou, Z. Y., and Mandel, L. Measurement of subpicosecond time intervals between two photons by interference. *Phys. Rev. Lett. 59* (Nov 1987), 2044–2046.

[20] Ionicioiu, R., Amaratunga, G., and Udrea, F. Quantum computation with ballistic electrons. *International Journal of Modern Physics B 15*, 02 (jan 2001), 125–133.

[21] Ivanov, D. A., Lee, H. W., and Levitov, L. S. Coherent states of alternating current. *Phys. Rev. B 56* (Sep 1997), 6839–6850.

[22] Marguerite, A., Bocquillon, E., Berroir, J., Plaçais, B., Cavanna, A., Jin, Y., Degiovanni, P., and Fève, G. Two-particle interferometry in quantum hall edge channels. *physica status solidi (b) 254*, 3 (Dec. 2016).

[23] Roulleau, P., Portier, F., Glattli, D. C., Roche, P., Cavanna, A., Faini, G., Gennser, U., and Mailly, D. Finite bias visibility of the electronic mach-zehnder interferometer. *Phys. Rev. B 76* (Oct 2007), 161309.

[24] Roussel, B., Cabart, C., Fève, G., and Degiovanni, P. Processing quantum signals carried by electrical currents. *PRX Quantum 2* (May 2021), 020314.

[25] Roussely, G., Arrighi, E., Georgiou, G., Takada, S., Schalk, M., Urdampilleta, M., Ludwig, A., Wieck, A. D., Armagnat, P., Kloss, T., Waintal, X., Meunier, T., and Bäuerle, C. Unveiling the bosonic nature of an ultrashort few-electron pulse. *Nature Communications 9* (July 2018).

[26] Thibierge, É. *Cohérence à un et deux électrons en optique quantique électronique.* Thèse de doctorat, Ecole normale supérieure de lyon - ENS LYON, June 2015.

[27] Tsukada, N., Wieck, A., and Ploog, K. Proposal of novel electron wave coupled devices. *Applied Physics Letters 56* (Jun 1990), 2527–2529.

[28] Vidal, N. T., Bera, M. L., Riera, A., Lewenstein, M., and Bera, M. N. Quantum operations in an information theory for fermions. *Physical Review A 104*, 3 (Sept. 2021).

[29] Wölk, S., Huber, M., and Gühne, O. Unified approach to entanglement criteria using the cauchy-schwarz and hölder inequalities. *Physical Review A 90*, 2 (Aug. 2014).